Technische Universität München

Lehrstuhl für Technische Chemie II

Transport in Nanoporous Solids

Oliver Christian Jean-Marie Gobin

Vollständiger Abdruck der von der Fakultät für Chemie der Technischen Universität München zur Erlangung des akademischen Grades eines

Doktors der Naturwissenschaften (Dr. rer. nat.)

genehmigten Dissertation.

Vorsitzender: Univ.-Prof. Dr.-Ing. K.-O. Hinrichsen

Prüfer der Dissertation:

1. Univ.-Prof. Dr. techn. J. A. Lercher
2. Univ.-Prof. Dr. rer. nat., Dr. rer. nat. habil. K. Köhler
3. Univ.-Prof. Dr.-Ing. H. Klein

Die Dissertation wurde am 30.07.2010 bei der Technischen Universität München eingereicht und durch die Fakultät für Chemie am 10.02.2011 angenommen.

Everything flows, nothing stands still.

Heraclitus of Ephesus
(535 - 475 BC)

Contents

Acknowledgments

Only with the help and support of many people was it possible to finish this thesis. In the first part of this dissertation, I would like to thank all the people who contributed to the success of this thesis.

First of all, I would like to thank Professor Dr. Johannes A. Lercher for giving me the chance to work in a highly diverse international working group at the Chair of Technical Chemistry 2 at the Technische Universität München. I am deeply grateful for the supervision and guidance during the work and for the freedom I was given.

I would also like to thank my thesis co-supervisor PD Dr. Andreas Jentys for his support, guidance, and for the scientific discussions.

I am grateful to Professor Kärger and whole international research group 'Diffusion in Zeolites' for excellent meetings and stimulating discussions.

I also thank my co-worker Dr. Stephan J. Reitmeier, for the close collaboration we had during the time of the thesis and for the intense and excellent scientific discussions.

I wish to thank the whole group of Professor Lercher, for the great atmosphere and the many hours we spent together during conferences, e.g., in Weimar at the German catalysis conference. Especially I thank Robin Kolvenbach for excellent discussions about transport processes, and Michi for all the fish. I also thank all students I supervised in the last few years.

I thank Professor Dr. Ferdi Schüth, who always allowed me to run special measurements required for the thesis at the Max Planck Institute and for all the things I learned from him and from and the other members of the MPI during my Diploma thesis.

Finally, I want to thank my parents Marie-Hélène Gobin and Axel Schneider for their invaluable support in everything, and my brother Philippe Schneider.

Symbols

Latin symbols

A		amplitude
B	(m^2 s^{-1})	mobility
c	(g mol^{-1})	concentration
d	(m)	diameter
D	(m^2 s^{-1})	diffusion coefficient
E	(kJ mol^{-1})	energy
F	(m^2 s^{-1})	single file mobility
F	(m^3 s^{-1})	flow rate
G	(kJ mol^{-1})	free energy
h	(m)	pitch
H	(kJ mol^{-1})	heat of adsorption
I	(kg m^2)	moment of inertia
J	(mol s^{-1})	molar flux
k	(s^{-1})	rate constant
K	(-)	Langmuir or BET equilibrium constant
K_{H}	(-)	Henry constant
K_{FR}	(-)	FR constant
L	(m)	characteristic length
L	(-)	ZLC constant
M	(g mol^{-1})	molar mass
n	(-)	index
n	(-)	structural order
n	(mol)	amount adsorbed
N_{A}	mol^{-1}	avogados number: $N_{\mathrm{A}} = 6.022 \cdot 10^{23}$ mol^{-1}
P, p	(bar)	pressure
q	(g mol^{-1})	adsorbed phase concentration
q	(-)	partition function
q_n	(-)	roots
r	m	radius
R, r	(-)	rate
R	(J mol^{-1} K^{-1})	molar gas constant

S	(J mol^{-1})	entropy of adsorption
S	(m^2)	surface area
t	(s)	time
T	(K)	temperature
u	(m s^{-1})	velocity
V	(m^3)	volume
x	(-)	relative pressure: $x = p/p_0$
x, y, z	(-)	coordinate
w	(m)	wall thickness

Greek symbols

α	(-)	sticking probability
α_s	(-)	α_s-plot
β_n	(-)	roots
δ	(-)	number of sites
δ	(-)	variance
δ	(-)	symmetry number
δ	(-)	FR characteristic function
ϵ	(-)	porosity
γ	(N m^{-1})	surface tension
λ	(m)	mean free path
μ		chemical potential
ω	(s^{-1})	angular frequency
τ	(-)	tortuosity
τ	(s)	time constant of a transport process
θ	(-)	loading
χ	(-)	trapping coefficient

Indices

$\parallel$	parallel
$\perp$	perpendicular
0	reference or initial value
a	axial
ads	adsorption
c	core
des	desorption
e	edge
ext	external
fiber	fiber
m	molecular
max	maximum
ma	macropore
me	mesopore
mi	micropore
min	minimum
p,pore	pore
r	radial
s	surface
t	tangential
tot	total
w	wall

Abbreviations

Abbreviations

AAS	atomic absorption spectroscopy
a.u.	arbitrary units
BAS	Brönsted acid sites
BET	Brunauer, Emmett, Teller
BJH	Barrett, Joyner, Halenda
CVD	chemical vapor deposition
CLD	chemical liquid deposition
DFT	density functional theory
DLS	dynamic light scattering
DSC	differential scaning calorimetry
DTA	differential thermoanalysis
EFI	electronic fuel injection
FAU	Faujasite
FT	Fourier transformation
FTIR	Fourier transform infrared spectrometer
FR	frequency response
GC	gas chromatography
GUI	graphical user interface
HC	hydrocarbons
HR	high resolution
H-ZSM-5	H-form of zeolite Socony Mobile 5
IUPAC	international union of pure and applied chemistry
IR	infrared
IRM	infrared microscopy
IZA	international zeolite association
K	Kelvin
LAS	Lewis acid sites
LTA	Linde type A zeolite
MCM-22	Mobil composition of matter 22
MD	molecular dynamics
MFI	ZSM-5
MEL	ZSM-11
MOR	Mordenite
MS	mass spectrometry, mass spectrometer

NMR	nuclear magnetic resonance
NRMS	normalized root mean square error
PID	proportional-integral-derivative controller
PFG	pulsed field gradient
PSD	pore / particle size distribution
QENS	quasi-elastic neutron scattering
RS-IR	rapid scan infrared spectroscopy
SBU	secondary nuilding unit
SEM	scanning electron microscopy
S/N	signal to noise ratio
STP	standard temperature and pressure
TAP	temporal analysis of products
TEM	transmision electron microscopy
T-atom	tetrahedrally coordinated Si or Al atom
TG	thermogravimetry
TGA	thermogravimetric analysis
TPD	temperature programmed desorption
u.c.	unit cell
UHV	ultra high vacuum
XRD	X-ray diffraction
XPS	X-ray photoelectron spectroscopy
ZSM-5	Zeolite Socony Mobil 5
ZSM-11	Zeolite Socony Mobil 11
ZLC	zero length column

1 Introduction

The fundamental understanding of the sorption and transport properties of porous solids is essential for their application as adsorbents, catalysts, or functional materials. The focus of this thesis is the detailed investigation of the mass transport processes in several complex porous solids.

The thesis is structured in the following way. In chapter 2, a broad introduction to porous materials, to their sorptive properties, and to the analysis of sorption dynamics is given. This also includes a chapter on the fundamentals of diffusion and on the techniques typically used to measure the sorption kinetics.

In chapter 3, the intracrystalline transport properties of ZMS-5 zeolites are systematically investigated by correlating the complex structure of the zeolite with the transport properties of several aromatic compounds. It was found that, depending on the molecule geometry, the diffusion in the particles is isotropic or anisotropic.

Chapter 4 is based on the results of chapter 3. In this chapter, the ZSM-5 sample investigated in chapter 3 is compared to a sample that is composed of nano-sized particles. In the case of such small particles, surface effects may dominate the overall transport. A kinetic transport model including the gas-phase adsorption of molecules on the outer surface, the pore entering into the zeolite framework, and the intracrystalline diffusion is presented and used in order to quantify the effects that occur. It was found that in the case of the sample with nano-sized particles, surface effects are rate limiting and, thus, define the tranport properties.

Chapter 5 is directly based on this finding. If surface effects are the rate limiting step in the nano-sized particle system, modification of the outer surface should distinctly influence the overall transport. In this study, the surface of the particles was modified by a chemical liquid deposition in order to build up an amorphous silica layer on the surface. The transport was investigated and some important changes in the kinetics were observed. For instance, for some molecules, an enhancement of the overall transport was observed, whereas for other molecules, a decrease in the rate occurred. These findings are quantified and discussed on the molecular level in order to understand the impact of such surface treatments, for instance for applications in catalysis.

In the last chapter of this thesis, the transport in a new system is investigated in detail. The material studied in this chapter is a very complex hierarchical mesoporous fiber sample. It is composed of a primary, a secondary, and a ternary structure, and can be considered as a model system for complex materials composed of several hierarchical domains with different porosities or other structural features. It was found, that only by relating the transport properties of each structural domain, an accurate description of the macroscopic transport is possible.

In summary, this thesis gives a broad overview of the analysis of a multitude of different transport processes that may occur in porous solids. This includes the intracrystalline diffusion in micropores, the effective diffusion in mesopores, surface diffusion, and surface effects, as well as the combination of all these processes.

2 State of the art

2.1 Porous materials

Porous materials have attracted the interest of scientists and industry due to their various applications, for instance in molecular separation, heterogeneous catalysis, adsorption technology or opto-electronics, as well as new challenges in the fundamental material research (Banhart, 2001, Davis, 2002, Yaghi et al., 2003). In all applications where porous materials are involved, the molecular level understanding of catalytic and sorptive processes in porous materials is essential for the improvement of their specific properties.

In general, the surface area of a porous material is higher than the surface of an analogous non-porous material. Thereby the internal surface area is usually much higher than the one contributed by the external surface. Due to the fact that heterogeneous catalyzed chemical reactions basically occur on surfaces or at phase boundaries, a higher surface area would, theoretically, directly yield to an improved reactivity. In reality, different kinds of limitation can occur and have to be taken into consideration. Apart from the surface area, other important characteristics of porous solids are the crystallinity or regularity if present, the distribution of pore sizes and the chemistry of the walls. In an ideal porous material, these attributes should be tailored exactly to the needs of the application. To be commercially interesting, such a material should be inexpensive and highly stable for regeneration. Materials based on silicate show such kind of flexibility and have found wide fields of industrial applications.

According to the IUPAC definition (Sing et al., 1985) micropores are pores with a diameter under 2 nm, mesopores with a diameter between 2 and 50 nm, and macropores have diameters greater than 50 nm. Corresponding to this definition, materials can be labeled as solids with a certain porosity. A list of selected definitions associated with porous solids is given in Table 2.1. Examples of microporous materials are zeolites (Kirschhock et al., 2008, Kokotailo et al., 1978, Olson et al., 1981). A well-known mesoporous material is MCM-41 (Mobil Composition of Matter No 41) (Beck et al., 1992) with highly ordered pores. The MCM-41 bi-porous counterpart is SBA-15 (Santa Barbara No 15). Macroporous materials are, for example, porous glasses or gels. In the following two important classes of porous materials relevant for this thesis will be

Term	Definition
Porous solid	Solid with cavities or channels that are deeper than they are wide
Open pore	Cavity or channel with access to the surface
Interconnected pore	Pore that communicates with other pores
Blind or dead-end pore	Pore with a single connection to the surface
Closed pore	Cavity not connected to the surface
Void	Space between particles
Micropore	Pore of internal width less than 2 nm
Mesopore	Pore of internal width between 2 and 50 nm
Macropore	Pore of internal width greater than 50 nm
Pore size or width	Diameter or distance between opposite walls
Pore volume	Volume of pores determined by a stated method
Porosity	Ratio of pore volume to overall volume of particle or granule
Surface area	Area of total surface, as determined by stated method
Internal surface area	Area of pore walls
External surface area	Area of surface outside micropores and mesopores
True density	Density of solid, excluding pores and voids
Apparent density	Density of solid including pores, as determined by stated method
Tortuosity	Ratio of path available for diffusion to distance across porous bed
Zeolitic cage	Intracrystalline pore with windows allowing no passage of molecules larger than H2O
Zeolitic channel	Intracrystalline pore extending infinitely in one direction allowing passage of molecules

Table 2.1: Selected definitions associated with porous solids. From (Neimark et al., 1998b)

reviewed in more detail. The first class are the Zeolites and the second is the class of the ordered mesoporous materials.

2.1.1 Zeolites

Zeolites are an unique class of microporous, crystalline aluminosilicates that can either be found in nature or synthesized artificially (Kirschhock et al., 2008). They are the most widespread group of porous materials industrially used on large scales. The importance is due to their high surface areas in combination with their chemical nature. Their flexible and highly ordered framework structure allows the incorporation of hetero-atoms, i.e., aluminum, making zeolites acid solids with well defined properties. Both material features make them efficient cation exchangers, e.g., Zeolite A in laundry powder, adsorbents, or catalysts (Zeolite Y, mordernite, MCM-22, Zeolite beta, ferrierite, ZSM-5, ZSM-22). Important industrial applications are, for instance, catalytic processes in

the petrochemical industry, e.g., fluid catalytic cracking, isomerization, and alkylation (Corma, 1995, Gilson and Guisnet, 2002).

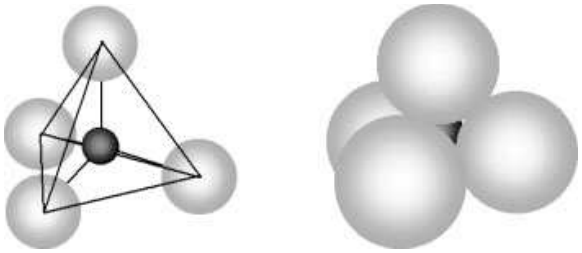

Figure 2.1: Schematic representation of a SiO_4 tetrahedra.

Zeolites were discovered in 1756 by the Swedish mineralogist Axel Frederick Cronsted, who observed that the mineral stilbite loses water when heated. The name zeolite stems from the two Greek words, zeon (to boil), and lithos (stone). In the 1930s, Richard Barrer studied the synthesis of zeolites, and succeeded in 1948 for the first time to synthesize an artificial zeolite without counterpart in nature. Nowadays, about 250 zeolite structures are known and new ones are discovered every year. A general classification of structures was defined by the IUPAC (International Union of Pure and Applied Chemistry). In this system, each structure has three letters, e.g., FAU for faujasites or MOR for mordenites. The most common types of zeolites can be found in the database of zeolite structures (Baerlocher and McCusker, Baerlocher et al., 2001).

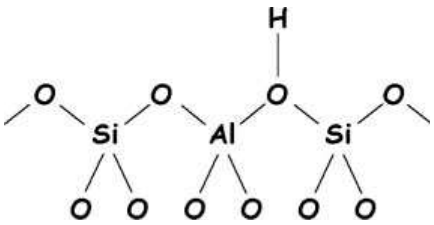

Figure 2.2: Representation of a Brønsted acid site in a zeolite matrix.

Basically, zeolites consist of SiO_4 and AlO_4 tetrahedra as shown in Figure 2.1, that are arranged by sharing of oxygen atoms to build a crystalline lattice. The tetrahedra can be arranged into several silicate units, for instance, six, eight, or twelve-membered rings. These units are called secondary building blocks as shown in Figure 2.3. The zeolite structure is then formed by joining these secondary building blocks into periodic structures.

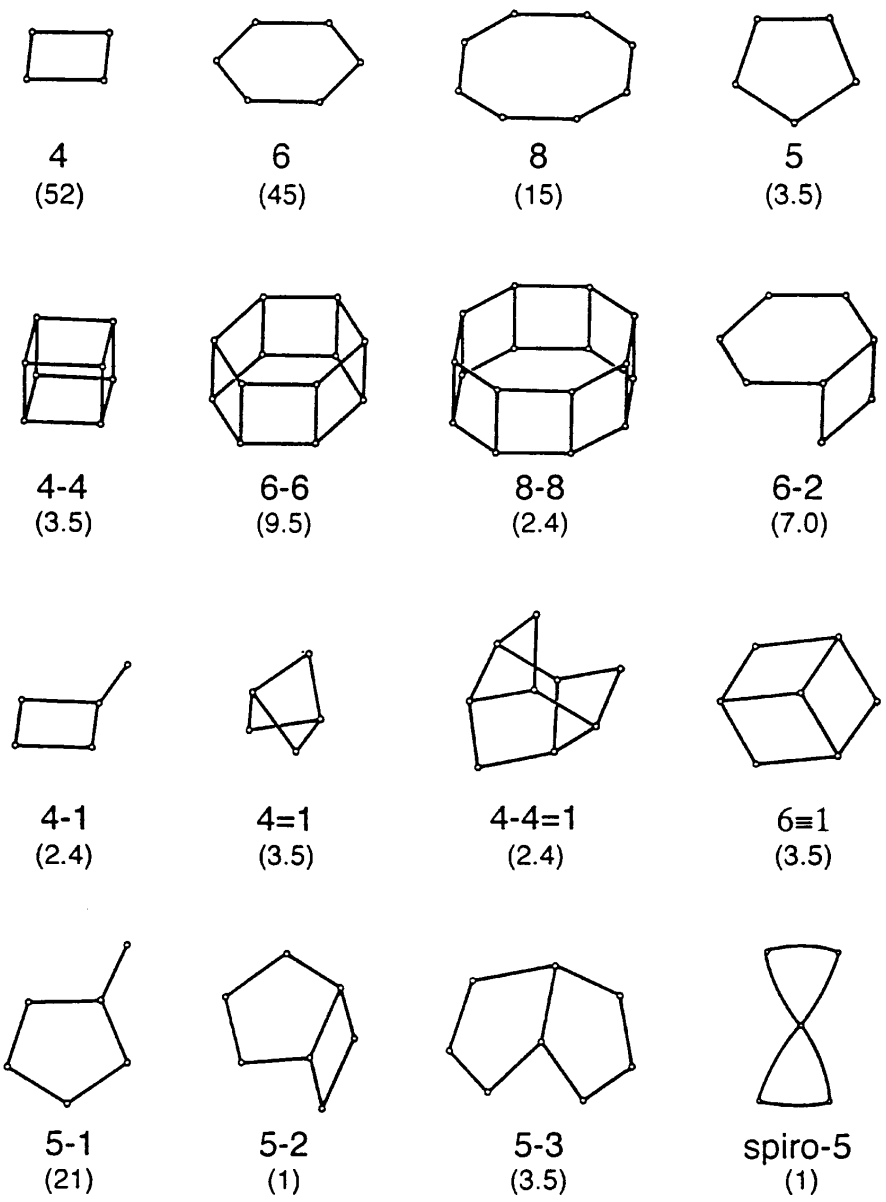

Figure 2.3: Secondary building units (SBUs). Adapted from Baerlocher et al. (2001) including frequency of occurrence in % (in parentheses)

By replacing Si^{4+} by Al^{3+} ions in the tetrahedras, a net charge of -1 is generated for each substitution. This negative charge is neutralized by cations such as Na^{+}. The number of cations in the zeolite structure equals the number of alumina tetrahedra in the framework. If the sodium ion is replaced by protons (H^{+}) a Brønsted acid site is obtained as shown in Figure 2.2. The acid strength of the site depends on the local environment of the proton, and, in particular, on the number of other aluminum ions in the environment.

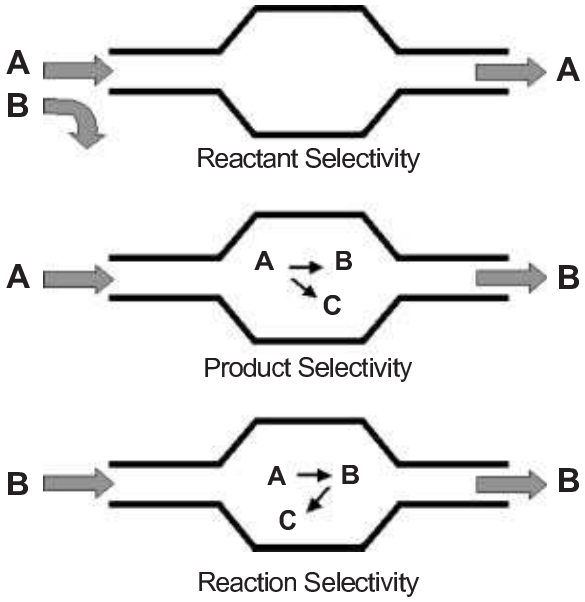

Figure 2.4: Catalytic selectivities induced by the distinct shape of zeolites.

In summary, the combination of crystallinity, uniform pore systems with cages, reactive (acid) surfaces, and a high internal surface area enables the application of zeolites as adsorbents, ion exchangers, and especially shape selective catalysts. In Figure 2.4, the three types of shape selectivity due to the pore structure are shown. The pores only allow molecules small enough to enter or to leave the zeolite lattice. In the case of reactant selectivity as shown in Figure 2.4, one of the reactants is excluded, as it is to big to enter the zeolite. In the second case, i.e., product selectivity, several products are formed in the cages of the zeolite; however, only the product that is small enough is also able to leave the pores of the zeolite. The third type of selectivity induced due to the zeolite structure is the reaction selectivity. In this case, the formation of a bulky transition state is prohibited, and thus a certain reaction pathway excluded (Barthomeuf, 1996, Caro et al., 2000).

2.1.2 Mesoporous materials

Zeolites are, in principle, perfect functional materials, with many unique properties. The major drawback of zeolites is their limitation to pore sizes below 2 nm. Such small pores only allow the reaction of small molecules and often leads to diffusion limitations and thus to rapid deactivation in many industrial processes. Larger pores are required to prevent deactivation and are also needed for the catalytic conversion of bulky molecules. In 1992 researchers from the Mobil Oil Company were the first to develop a synthesis route using liquid crystal templating leading to a new family (M41 S) of mesoporous molecular sieves (Kresge et al., 1992). The MCM-41 materials, as shown in Figure 2.5 are one species of these materials which have been the most investigated. They are mesoporous materials of cylindrical rod-like pores with diameters from 1.5 nm up to about 8 nm ordered in hexagonal arrays. The long range space group is $P6mm$. The pore walls are amorphous and relatively thin. The wall thickness is usually between 0.6 and 1.2 nm (Neimark et al., 1998a). Due to the long rod-like pores, this material is ideally homogeneous and isotropic only on a mesoscopic scale in one or two dimensions.

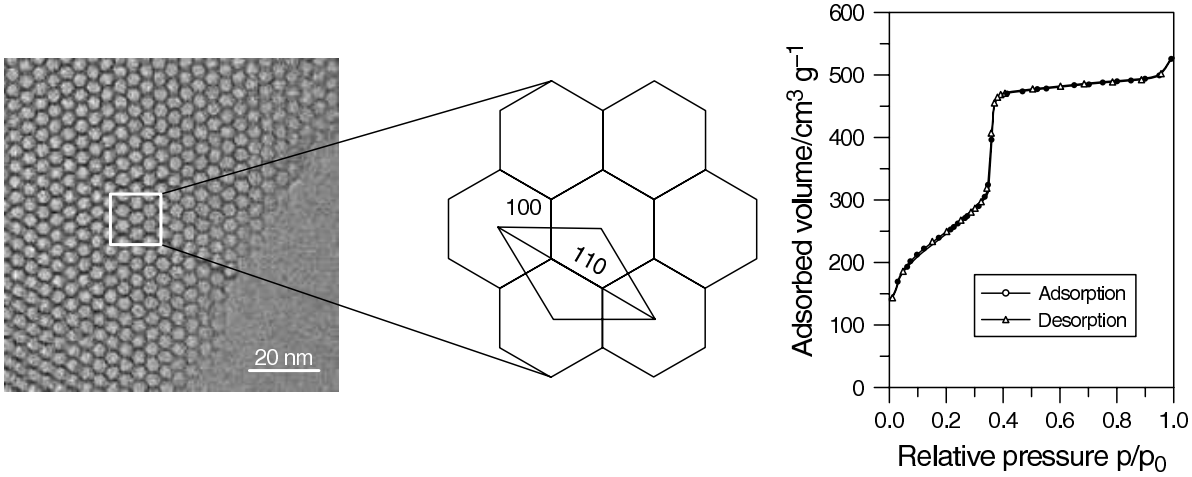

Figure 2.5: Left: Transmission electron microscopy image of MCM-41. Center: Representation of the hexagonal lattice. Right: Nitrogen physisorption isotherm measured at 77 K of calcined MCM-41. From Linden et al. (1998)

Typical pore size distributions are very narrow, an indication for a well ordered structure. The porosity only consists of mesopores without intrawall micropores. This leads to a one-dimensional diffusion through the pores.

MCM-41 materials have found various application in catalysis (Ciesla and Schüth, 1999, Sayari, 1996, Zhao et al., 1996) and various techniques for characterization have

been developed (Jaroniec et al., 1998, 1999, 2000, Kruk and Jaroniec, 2001, Kruk et al., 1999, 2000, Lukens et al., 1999, Neimark and Ravikovitch, 2000, Neimark et al., 1998a, Ravikovitch et al., 1997, 1998, Sayari et al., 1997). They have a very high BET surface area up to 1000-1200 m^2/g. The morphology, pore sizes and BET surface areas are highly adjustable during the synthesis. Also, the chemistry of the walls can be easily changed by incorporation of heteroatoms or grafting techniques (Lim and Stein, 1999, Maschmeyer et al., 1995, Moller and Bein, 1998, Wu et al., 2002). The most important limitation, for example, as FCC catalyst is the low hydrothermal stability of these materials (Kim et al., 1995, Ryoo and Jun, 1997), caused by the rather thin and amorphous pore walls.

In order to overcome this limitation, materials with thicker walls were developed. SBA-15 is a typical material prepared under acidic conditions with the triblock copolymer Pluronic P123 ($EO_{20}PO_{70}EO_{20}$) surfactant as template (Zhao et al., 1998a,b). The mesopores are ordered in hexagonal arrays providing the same long range space group as the one of MCM-41 materials ($P6mm$). However, due to the properties of the Pluronic type surfactant (Alexandridis and Hatton, 1995) SBA-15 materials show important differences in porosity and adsorption properties compared to MCM-41 materials. In a regular synthesis, SBA-15 materials have much thicker walls and primary mesopore diameters between 5 nm and 15 nm. The BET surface area of SBA-15 is generally lower than the one of MCM-41. Due to thicker pore walls, they are hydrothermal more stable (Han et al., 2002, Wu et al., 2002). Also, because of the Pluronic surfactant type, SBA-15 materials generally have a second intrawall porosity consisting of micropores or smaller mesopores. These unordered pores interconnect the primary mesopore channels. It is possible to tailor the micro/mesopore ratio to the needs of the application, still conserving the rather thick pore walls. The intrawall microporosity is caused by the penetration of the hydrophobic PO groups of the blockcopolymer chain into the silica matrix. The wall thickness is caused by the length of these polymer chains.

2.1.3 Hierarchical materials

Hierarchical materials are materials with structures on more than one length scale (Lakes, 1993). Typically, they are composed of structures which themselves contain structured elements. The structural hierarchy often defines the macroscopic, i.e., the bulk properties of the material itself. Many examples of hierarchical materials or frameworks can be found in nature as well as in engineering. In engineering, the Eiffel Tower, or bridges such as the Garabit Viaduct are prominent examples. Porous materials such as zeolites or human bones, as shown in Figure 2.6, are examples for natural hierarchical materials.

In general, hierarchical structures can be characterized by the hierarchical order that

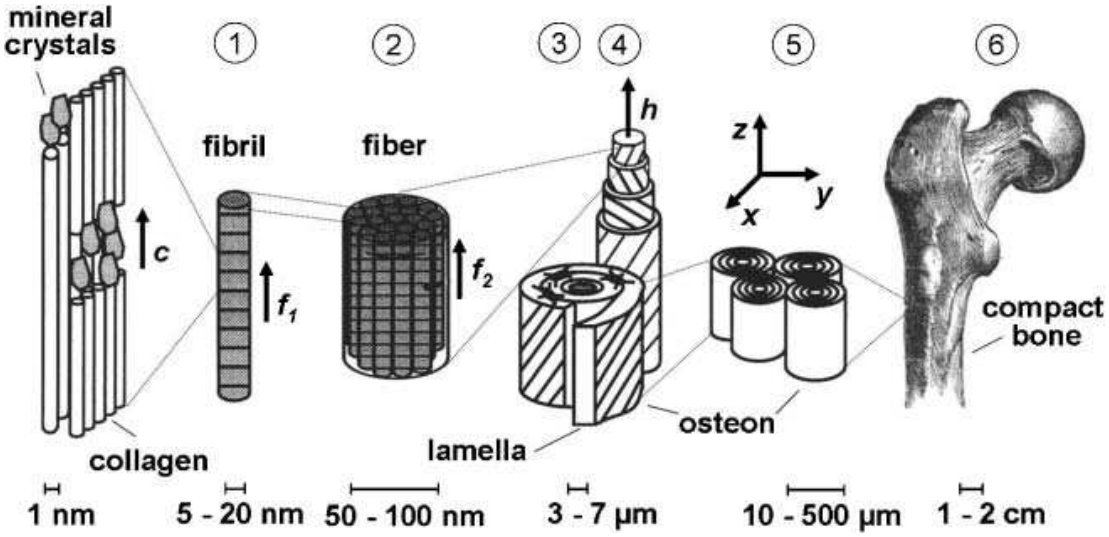

Figure 2.6: Hierarchical structure of a compact bone. Figure from Marlow et al. (2007).

is defined as the number n of length scales with structured elements. A material without structural order, i.e., a zero order hierarchy ($n = 0$), can be regarded as a continuum with respect to the analysis of physical properties. A first order structure contains only one length scale of structural elements. One example is the atomic lattice of a crystal. A material with a hierarchical order of 0 or 1 is typically not considered to be a hierarchical material. An order of 2 is typical for complex structures, such as zeolites, as the zeolite structure is formed by the assembly of secondary building blocks into periodic structures. Higher hierarchical orders are often very complex and the complete unterstanding of the bulk properties is challenging.

An example of third order materials relevant for this thesis are ordered mesoporous fibers. Ordered mesoporous fibers are an interesting, novel type of materials of the M41 S family, with a unique morphology and internal structure. The primary structure is composed of cylindrical mesopores and secondary pores in framework. The second structural domain is composed of the cylindrical mesopores arranged in an ordered hexagonal pore array, and the ternary structure of rod-like particles with diameters of 20 to 50 μm and a length of up to several milimeters.

In order to understand and to quantify the diffusion in such kind of hierarchical materials, all three domain have to be considered. A detailed analysis of the diffusion in ordered mesoporous fibers is given in chapter 6.

2.2 Fundamentals of sorption equilibria

This chapter deals with the fundamentals of the analysis of equilibria and kinetics of adsorption in porous solids. In particular, systems relevant for this thesis will be discussed, however, the methods described herein are valid for a broad range of adsorption phenomena in porous media, e.g., liquid phase systems. Adsorption is usually associated with a porous solid. This is due to the fact that a porous solid, because of its internal pores, provides a much higher surface area compared to a non-porous solid. Often these pores are very small with a high pore volume, and thus, a high adsorption capacity can be reached. During the filling of the pores, molecules need to pass through many of them in order to find a way inside the solid. The understanding and modeling of the transport process occurring during the adsorption of molecules is the domain of the sorption kinetics. The understanding of the adsorption capacity under certain condition is the domain of the sorption equilibria. Both equilibria and kinetics need to be understood, in order to understand a sorption process. In this chapter, first sorption equilibria will be discussed, as these are necessary in order to understand the sorption kinetics that will be discussed subsequently.

2.2.1 The Langmuir adsorption theory

The first consistent adsorption theory was proposed by Irving Langmuir in 1918. It is based on a kinetic point of view, that is, a continuous bombardment of molecules onto the surface, and a continuous desorption from the surface in order to lead to a zero rate accumulation of molecules at the surface at equilibrium.
The assumptions of the Langmuir model are:

1. The surface is homogeneous, that is, a flat surface where the adsorption energy is constant over all sites.
2. Adsorption on surface is localized, that is, adsorbed atoms or molecules are adsorbed at definite, localized sites. No interaction between the adsorbed species occur.
3. Each site can accommodate only one molecule or atom, thus only one monolayer can be adsorbed.

The rate of striking the surface, in mole per unit time and unit area, obtained from the kinetic theory of gas multiplied by the sticking coefficient α, gives the rate of adsorption on an empty surface:

$$R_{\text{ads}}^{\text{empty}} = \frac{P}{\sqrt{2\pi MRT}} \cdot \alpha \tag{2.1}$$

the rate of adsorption on an occupied surface is equal to the rate given by equation (2.1) multiplied by the fraction of empty sites $(1-\theta)$:

$$R_{\text{ads}} = \frac{\alpha P}{\sqrt{2\pi MRT}} \cdot (1-\theta) \tag{2.2}$$

The rate of desorption from the surface is equal to the rate, that corresponds to a fully covered surface (k_{des}), multiplied by the fractional coverage θ:

$$R_{\text{des}} = k_{\text{des}} \cdot \theta = k_{\text{des}}^{\infty} \cdot \exp\left(\frac{E_{\text{des}}}{RT}\right) \tag{2.3}$$

where E_{des} is the activation energy for desorption, which is identical to the heat of adsorption for physically adsorbed molecules.

Since the rate of adsorption has to be equal to the rate of desorption, that is, $R_{\text{ads}} = R_{\text{des}}$ the Langmuir isotherm is obtained:

$$\theta = \frac{Kp}{1+Kp} \tag{2.4}$$

where

$$K = \frac{\alpha \exp\left(H_{\text{ads}}/RT\right)}{k_{\text{des}}^{\infty}\sqrt{2\pi MRT}} = K^{\infty} \cdot \exp\left(\frac{H_{\text{ads}}}{RT}\right) \tag{2.5}$$

Herein, K is the Langmuir constant, which is a measure of how strong a molecule is attracted to the surface. K^{∞} is the pre-exponential factor, which is inversely proportional to the square root of the molecular weight.

The Langmuir isotherm reduces to the Henry isotherm when the pressure is very low, i.e., $Kp << 1$:

$$\theta = Kp \tag{2.6}$$

In the Henry region, the adsorbed amount increases linearly with the pressure. In contrast, at high pressures, the saturation capacity is reached ($\theta \to 1$) corresponding to a complete coverage of all adsorption sites. Langmuir isotherms for different Langmuir constants K are shown in Figure 2.7.

Strong adsorbate-adsorbent interaction, i.e., a high heat of adsorption, result in a large Langmuir constant K leading to a higher surface coverage compared to the corresponding coverage for lower K at the identical pressure as shown in Figure 2.7. An increase in the temperature decreases the amount of adsorbed molecules, as adsorption is an exothermic process and thus more molecules have sufficient energy to evaporate from the surface. Adsorption must be exothermic (i.e., $\Delta H < 0$) since the free energy ΔG must decrease and the entropy change ΔS is negative because of the decrease in the degrees of freedom for the adsorbed molecule:

$$\Delta H^{o} = \Delta G^{o} + T\Delta S^{o} \overset{!}{<} 0 \tag{2.7}$$

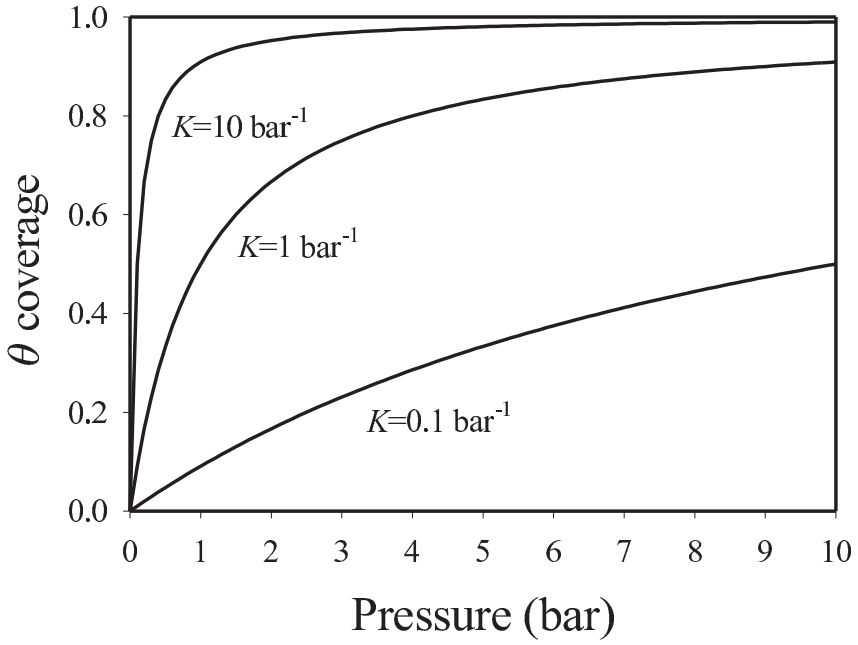

Figure 2.7: Langmuir isotherms for different Langmuir constants.

Isosteric heat of adsorption

Essential in the study of adsorption kinetics is the knowledge of the heat of adsorption. When molecules are adsorbed, the produced heat can be dissipated to the surrounding, or absorbed by the solid. The portion that is absorbed by the solid increases its temperature and may influence the kinetics of sorption. The isosteric heat of adsorption can be obtained from the vanť Hoff equation:

$$\frac{\Delta H}{RT^2} = -\left(\frac{\partial \ln p}{\partial T}\right)_\theta \tag{2.8}$$

2.2.2 Multilayer adsorption

Brunnauer, Emmett and Teller introduced the concept of multilayer adsorption. Here the first layer of adsorbed molecules acts as new substrate for further adsorption. The classical 2-parameter equation is the well known BET-equation:

$$\theta_{\mathrm{BET}}(x) = \frac{n}{n_m} = \frac{1}{1-x} \cdot \frac{Kx}{1+(K-1)x} \tag{2.9}$$

with the total amount of adsorbates n, the amount of adsorbates in a monolayer n_m, the relative concentration or pressure x, and a constant K, which is related to the net heat

of adsorption of the monolayer. It is important to note that this classical form is only valid for an infinite number of layers on a flat surface taking into account the same heat of adsorption for each layer. To calculate the parameters n_m and K, equation (2.9) can be rewritten into the classic BET linear form:

$$\frac{x}{n(1-x)} = \frac{1}{n_m K}\left(1 + (K-1)\,x\right) = \frac{1}{n_m K} + \frac{K-1}{n_m K}x \tag{2.10}$$

Now a plot of $x/n(1-x)$ against x should yield a straight line in a pressure range of about 0.05 to 0.3 p/p_0. From the slope and the intercept, it is possible to determine the above two parameters. The specific surface S_{BET} occupied by the monolayer of the adsorbates can be obtained from n_m and the net heat of adsorption from K. Some restrictions to the parameter K can be used to optimize the BET analysis. For instance, K always has to be positive and larger than zero. Sing et al. (1985) analyzed the influence of K.

The analysis of the adsorption isotherm by the BET method is a common method to determine the surface area of a porous material, but it is mostly restricted to mesoporous or macroporous materials. The application of the BET method to materials containing micropores has to be done with care and only an apparent surface area can be obtained.

Depending on the structure of the solid and on the forces during adsorption, the IUPAC developed in 1985 a standard classification into six general sorption isotherm types. Type I is characteristic for microporous solids like zeolites or monolayer adsorption, type II for nonporous and type III for macroporous solids. Type IV and V possess a hysteresis loop typical for sorption in mesopores proceeding through multilayer adsorption and capillary condensation. Type VI represents the relatively rare stepped multilayer sorption isotherm (Figure 2.8A).

Beside the IUPAC classification, the interpretation of the hysteresis loop observed for mesoporous materials with type IV isotherms can reveal more interesting phenomenas. Rouquerol et al. (1999) has classified the hysteresis loop into four main types as shown in Figure 2.8B. A loop of type H1 is symmetrical with nearly parallel adsorption and desorption branches and often found in cylindrical pore systems in materials like MCM-41, MCM-48 or SBA-15. Type H2 is asymmetrical and triangular and can be assigned to pore systems with pore network connectivity and pore blocking as typical for 'ink-bottle' pores. Type H3 is typical for slit-shaped pores.

It is generally believed that the shape of the adsorption branch of the hysteresis loop is related to the absence or presence of pore network connectivity in the mesoporous materials. Type H1 hysteresis loop is usually assigned to a mesoporous material made up of unconnected pores, whereas type H2 hysteresis loop is expected for mesoporous materials with a connected pore structure (Sangwichien et al., 2002).

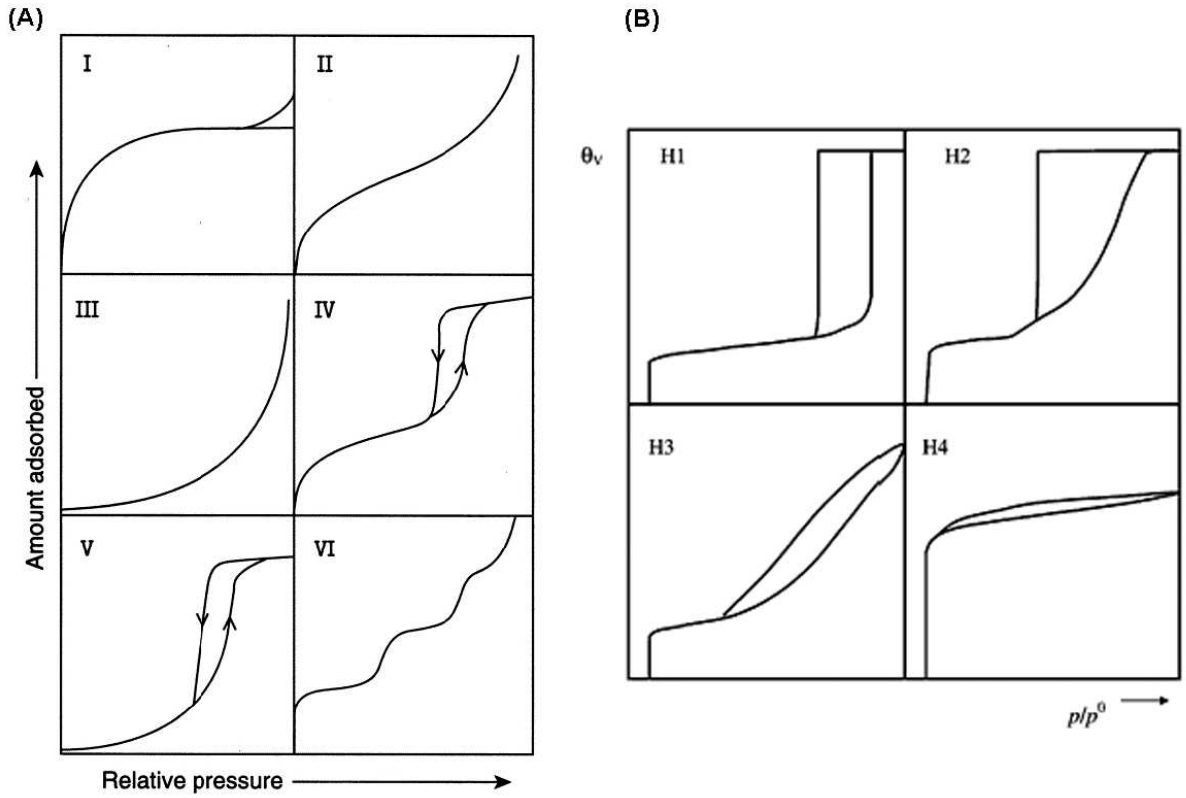

Figure 2.8: (A) IUPAC classification of sorption isotherms from Sing et al. (1985); (B) Modern classification of hysteresis loops from Rouquerol et al. (1999).

Neimark has shown that three different effects can affect the hysteresis loop. These are in particular cavitation and pore-blocking effects or the near equilibrium desorption. In SBA-15/MCM-41 or MCM-48 materials the desorption is generally near equilibrium, no major kinetic effects are limiting the desorption. In pore-blocked materials such as SBA-16 the desorption is kinetically limited by smaller pore entrances, the desorption can be spinodal, that means at a certain critical point the liquid will switch from an meta-stable regime to an unstable regime and desorp immediately out of the mesopores at a certain pressure. Cavitation effects are similar to pore blocking and also a spinodal desorption occurs, but even at a lower pressure (0.45 - 0.48 p/p_0) due to even smaller pore entrance sizes (Neimark and Ravikovitch, 2000, Ravikovitch and Neimark, 2002).

2.2.3 Pore volume and pore size distribution

The pore size distribution reflects in some way the distribution of any one dimensional geometric parameter of a porous material. Of course any arbitrary parameter can be

used to generate other kinds of distributions, such as pore volume distributions.

Looking at this definition, one easily realizes that the exact description of the porous geometry is fundamental to obtain valid distributions for any geometric parameter of the porous systems.

The typical pore size distribution (PSD) can be obtained in a statistical or in a classical way. The basic concept of the statistical way, which is in parts equal with the thermodynamic way, is to represent the experimental physisorption isotherm as a set of independent, non-connected pores. This can be done by multiplication of the sum of all pore sizes of the system (the actual PSD) with the theoretical representation of the adsorption data, as expressed by the following integral equation:

$$N_{\text{exp}}(x) = \int_{R_{\text{min}}}^{R_{\text{max}}} N_{\text{theo}}(x, r) \cdot \text{PSD}(r)\, \text{d}r \tag{2.11}$$

where $N_{\text{exp}}(x)$ is the experimental isotherm as a function of the relative pressure and $N_{\text{theo}}(x, r)$ the theoretical isotherm as a function of the relative pressure and the pore radius (or any other one dimensional geometric parameter of the porous system). To obtain the PSD, this equation has to be solved by inversion of the integral equation.

The main challenge is now to find a appropriate theory to compute the theoretical isotherm. An analytical solution by statistical mechanics and thermodynamics is the non local density function theory (NLDFT). Also well known are numerical solutions by Monte Carlo simulations. The classical way is known as the BJH-method and has been developed 1951 by Barrett et al. (1951). It is based on classical thermodynamics and uses the Kelvin equation to calculate the radius of the pore and an adequate analytical equation for the statistical film thickness of the adsorbates. The Kelvin equation is only valid for a limited number of geometries and is a function of the shape. These are for example cylindrical, spherical or slit-shaped mesopores.

Kruk et al. (1997) proposed in 1997 a modified version of the BJH method. They introduced a correction therm for the original statistical film thickness equation and were able to accurately reproduce the pore size distributions of MCM-41 materials. The original and the modified BJH methods will be further studied in the following section.

The original and modified BJH method

As mentioned before, the original BJH method (Barrett et al., 1951) is based on a model for capillary condensation and evaporation in cylindrical pores using the classical Kelvin equation:

$$\ln x = -\frac{2\gamma V_L}{RTr_c(x)} \tag{2.12}$$

where V_L represents the molar volume of the liquid, γ the surface tension and $r_c = r - t(x)$ with r_c as the 'core' radius and r as the physical radius of the pore. The treatment of 'core' radius and pore radius is the main difference of different BJH methods. The original BJH assumes a constant ratio of 'core' to pore radius.

The Kelvin equation in (2.12) quantifies the deviation in equilibrium vapor pressure above a curved surface from that above a plane surface at the same temperature. In other words, it gives a basic relationship between curvature and thermodynamic activity of a liquid film.

Original BJH method In the original BJH method (Barrett et al., 1951) a calculation scheme has been developed to solve the following integral equation:

$$N_{\text{exp}}(x) = \int_{R_{\min}}^{\infty} \pi \cdot (r-t)^2 \cdot \text{PSD}(r)\ \text{d}r \tag{2.13}$$

The calculation scheme can be written the following way:

$$N_{\text{exp}}(x) = \underbrace{\sum_{i=1}^{k} \Delta V_i(r_i \leq r_c(x_k))}_{\text{1st part}} + \underbrace{\sum_{i=k+1}^{n} \Delta S_i \cdot t_i(r_i > r_c(x_k))}_{\text{2nd part}} \tag{2.14}$$

or as an indexwise scheme:

$$V_n = \frac{\bar{r}(x_n)^2}{(\bar{r}_{c,n} + \Delta t_n)^2} \cdot \left[\Delta N_{\text{exp}}(x,n) - \Delta t_n \cdot \underbrace{\sum_{j=1}^{n-1} \frac{\bar{r}(x_n)^2}{(\bar{r}_{c,n} + \Delta t_j)^2} \cdot \Delta t_j \cdot \frac{2V_j}{\bar{r}(x_j)}}_{\Delta S_n} \right] \tag{2.15}$$

This recursive defined equation has to be implemented starting 'backward' from the point where all pores are filled up with liquid (the last point of the desorption or adsorption branch). The PSD follows from the above using its definition: $\text{PSD}_n = V_n / 2\Delta r_n$.

Modified BJH method (KJS) As stated before the most important difference between the modified BJH method or KJS method (Kruk et al., 1997) is the treatment of the core radius of the Kelvin equation. Introducing the statistical thickness and a correction factor, Kruk, Jaroniec and Sajary (Kruk et al., 1997) were able to modify equation (2.12) to better represent the experimental data of SBA-15 measurements. The modified equation to calculate the core radius is the following:

$$r_c(x)(\text{nm}) = \frac{2\gamma V_L}{RT \ln x} + t_{\text{Harkins}}(x) + 0.3 \tag{2.16}$$

2.3 Diffusion in nanoporous materials

Critically important for the application of zeolites or mesoporous materials as adsorbents and catalysts are the transport properties, in particular the intracrystalline diffusion. Over the past 50 years, a number of experimental methods to measure the intracrystalline diffusion were developed in order to increase the basic understanding of the transport mechanisms. A complete understanding is still far from complete. This is in part due to the fact that, in order to measure the intracrystalline diffusion, desorption and adsorption have to be controlled by this process. (Kärger, 2003, Kärger and Ruthven, 2002, Kärger et al., 1992). In many previous studies this was obviously not the case. Heat effects, inhomogeneous materials with varying features, surface effects, and improper experimental conditions led to the measurement of kinetic processes that were not controlled by the intracrystalline diffusion (Ruthven and Brandani, 2005, Ruthven, 2007a). Therefore, in order to characterize the transport properties of porous materials, in principle the only methodology is to study the transport for each system under the relevant conditions. A different approach is to use model systems as benchmark materials. However, up to now, in the case of zeolites, consistency between different experimental measuring techniques was not achieved (Kärger, 2003, Kärger and Ruthven, 1989). In other words, different measurements techniques tend to measure different diffusivities in identical zeolite samples. For the characterization of the transport, however, only a single intracrystalline diffusivity is generally reported. The inconsistency is in part due to the investigated materials themselves, but also due to the experimental measurement techniques.

The techniques basically differ on the length scale that is observed. Roughly, they can be divided in microscopic, mesoscopic, and macroscopic methods (Ruthven, 2007b). The microscopic techniques measure the diffusivity on length scales smaller than the individual crystals or particles. Therefore, only a small detail of the complete transport is studied. In the case of mesoscopic techniques, only the transport of individual crystals or particles is observed. Thus, the length scale equals the crystal size. Using macroscopic methods, the complete transport from the surrounding phase into the porous phase is considered. Also, often not only individual particles, but packed beds are investigated. Two different types of diffusivities can be obtained by these techniques. The microscopic methods generally provide D_{self}, that is, the self diffusivity. The application of mesoscopic or macroscopic methods provide the transport diffusivity. Some experimental configurations of microscopic and macroscopic set-ups allow the measurement of the transport or self diffusion and vise-versa. A detailed description of the methods will be given in the next chapter.

2.3.1 Fundamentals of diffusion

Fick's first law provides a basis for the quantitative analysis of transport in microporous solids. In essense, it defines the diffusivity $D(q)$ as a function of the adsorbed phase concentration q:

$$J = -D(q)\frac{\partial q}{\partial z} \tag{2.17}$$

The diffusivity defined in this way measures the rate of transport of sorbate under a given concentration gradient, and thus may also be called the transport diffusivity.

From thermodynamics, however, the true driving force is the chemical potential gradient:

$$J = -B(q) \cdot q \cdot \frac{\partial \mu}{\partial z} \tag{2.18}$$

where $B(q)$ is the intrinsic mobility and μ the chemical potential. The mobility, or the so called corrected diffusivity $D_0(q) = B(q) \cdot RT$ can be derived by assuming equilibrium between the adsorbed phase q and the vapor phase. Commonly, this correction is referred to as Darken's equation:

$$D = B(q) \cdot RT \cdot \frac{\partial \ln p}{\partial \ln q} = D_0 \cdot \frac{\partial \ln p}{\partial \ln q} \tag{2.19}$$

For for a Langmuir system, the thermodynamic factor $\partial \ln p / \partial \ln q$ is equal to:

$$\frac{\partial \ln p}{\partial \ln q} = \frac{1}{1 - q/q_s} \tag{2.20}$$

where q_s is the adsorbed concentration at saturation. According to this model, at high loading the transport diffusivity will tend to infinity, and at low concentrations it will tend to be equal to the corrected diffusivity.

The tracer diffusivity D^* may also be defined using Fick's first law in a very similar way:

$$J^* = -D^*(q^*)\frac{\partial q^*}{\partial z}|_q \tag{2.21}$$

This coefficient measures the flux of marked molecules J^* under the influence of a concentration gradient of marked molecules q^* at constant total species concentration q. The major difference between the tracer diffusivity and the transport diffusivity is, beside its physically different definition, the fact that no external concentration gradient is present for the tracer diffusivity. Thus, in the case of the tracer diffusivity, molecules will move with respect to each other according to the Brownian motion, but not induced by an concentration gratient. Therefore, the tracer diffusivity is actually more a 'self-diffusivity' rather than a transport diffusivity. The self-diffusivity can be defined based on the Einstein relation:

$$D_{\text{self}} = \frac{1}{6}\frac{\langle r^2 \rangle}{t} \tag{2.22}$$

where $\langle r^2 \rangle$ is the mean squared displacement of a molecule over a given time t.

These diffusivities are related to each other by the following relation that follows from the Maxwell-Stefan model (Paschek and Krishna, 2001):

$$\frac{1}{D_{\text{self}}} = \frac{1}{D_0} + \frac{\theta}{D_{11}} \tag{2.23}$$

According to this model, in the low concentration limit, the transport, the corrected, and the self diffusivities are the same:

$$\text{for } q \to 0 \Rightarrow D_{\text{self}} = D_0 = D \tag{2.24}$$

herein, D_0 is the corrected diffusivity or the Maxwell-Stefan diffusion for a single component.

Most experimental techniques do not directly measure the diffusive flux, but the concentration change over time, $\mathrm{d}q/\mathrm{d}t$, that is defined by the Fick's second law:

$$\frac{\partial q}{\partial t} = D(q)\frac{\partial^2 q}{\partial z^2} \tag{2.25}$$

This follows directly from Fick's first law, provided that the diffusivity is independent of concentration and is used by macroscopic techniques to experimentally quantify the diffusivity.

2.3.2 Diffusion mechanisms

In the following section, the most common diffusion mechanims are discussed based on their importance for the transport in porous solids. The most important mechanisms occurring in these materials are the Knudsen diffusion in mesopores and the surface, slip, or single file diffusion in micropores. Figure 2.9 shows a selection of these diffusion mechanism in a schematic way. Often, in hierarchical materials composed of a wide range of pores, a combination of these diffusion mechanisms occur, leading to an effective diffusion coefficient (Krishna, 2009, Krishna and van Baten, 2009).

Molecular diffusion

If the mean free path of the sorbate molecules is much smaller than the one of the pores $d_{\text{p}} >> \lambda$, the number of molecule-molecule collisions is higher than the collisions with the pore walls, and the dominant diffusion mechanisms are viscous flow and molecular diffusion.

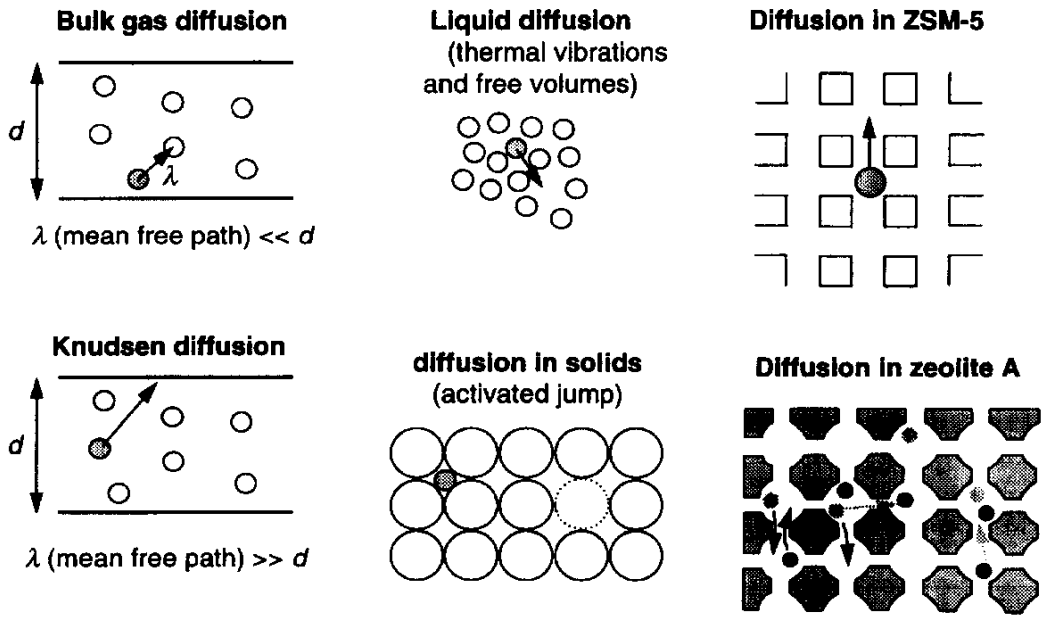

Figure 2.9: Selection of various diffusion mechanism. Figure from Krishna and Wesselingh (1997).

Due to the frequent collisions, molecules move at random and can be modeled as a random walk in three dimensions. Thus, molecular diffusion is identical to the Brownian motion of molecules. If a pressure gradient is present, the diffusive flow can be described according to Fick's first law, given in eq. 2.17.

Viscous flow

If the pores are large, another common diffusion mechanism is viscous Poiseuille flow in the pores. In this case, the transport is induced by a pressure gradient of a continuum fluid mixture. Hence, due to the viscous flow, all the molecules are moving in the same direction. The velocity gradient in a capillary is parabolic. The viscous flux can be derived from the Navier-Stockes equation, assuming a steady flow, no backmixing, and no slip at the capillary walls:

$$J = -q \cdot \frac{r^2}{8\mu} \frac{\partial p}{\partial z} \tag{2.26}$$

where r is the radius of the capillary and μ the dynamic viscosity of the fluid.

Knudsen diffusion

When the number of collisions with the pore walls becomes more pronouced than the number of molecule-molecule collisions, the transport occurs by Knudsen diffusion. In this case the molecule bounces from wall to wall. This mode usually occurs at low pressures in meso- and small macropores. The regime of Knudsen diffusion can be defined by the dimensionless Knudsen number:

$$\mathrm{Kn} = \frac{\text{mean free path}}{\text{diameter of channel}} = \frac{\lambda}{d} \tag{2.27}$$

When the Knudsen number is much larger than unity, transport occurs through a Knudsen flow and no longer through a viscous flow. For numbers much less than unity, the concept of viscosity is applicable and the transport occurs through a Poiseuille flow.

The Knudsen diffusivity for a cylindrical capillary may be defined as:

$$D_{\mathrm{K}} = \frac{2r}{3} \cdot \sqrt{\frac{8RT}{\pi M}} \tag{2.28}$$

where r is the radius of the capillary, and M the molecular weight of the adsorbed species. The Knudsen diffusion is proportional to the pore radius and to the pore geometry, to the square root of the temperature, and to the inverse of the molecular weight. It is, however, independent of the total pressure and of other diffusing species.

The Knudsen flux can than be written in terms of a concentration gradient according to Fick's first law:

$$J = -D_{\mathrm{K}} \frac{\partial p}{\partial z} \tag{2.29}$$

Surface and intra-crystalline diffusion

When the pores are small, i.e., micropores (< 2 nm), or the surface-molecule interactions are strong, molecules stick for a certain period to the walls and diffusion occurs through a hopping mechanism. This regime of diffusion, appart from being termed as surface or slip diffusion, is also widely refered as configurational, intracrystalline, or micropore diffusion. In all cases steric hinderances and surface-molecule interactions become important. It is the dominant diffusion mechanism in zeolites and often occurs in combination with Knudsen diffusion in the case of micro- and mesoporous materials. Due to the fact that many parameters are important for this type of diffusion, this is the most complex diffusion mechanism present in porous solids and many aspects are still poorly understood.

This diffusion regime can be easily distinguished from other transport mechanism by its activation energy. Due to the strong interactions between the molecules and the

pore wall, transport occurs through activated molecule jumps, leading to activation energies of 20 to 50 kJ/mol, depending on the level of confinement. In addition, the diffusion coefficents are generally between 10^{-10} to 10^{-20} m^2/s, i.e., several orders of magnitude lower than typical Knudsen diffusion coefficents (10^{-5} to 10^{-7} m^2/s). This type of transport can be described by equations 2.17 to 2.24 that provide an adequate description of transport in microporous solids.

Single file diffusion

If the pores are so small that molecules are not able to pass one another, the Einstein equation 2.22 is not valid anymore and diffusion occurs by an entirely different class of behavior, i.e., the so called single file diffusion. In such a system, the mean square displacement increases with the square root of time rather than with the first power of time:

$$\langle r^2 \rangle = 2F\sqrt{t} \tag{2.30}$$

where F is the single file mobility given by

$$F = \left(\frac{1-\theta}{\theta}\right)\sqrt{\frac{D_0}{\pi}} \tag{2.31}$$

Effective diffusion

In porous solids, a combination of the different types of diffusion may be present. This is especially the case for materials composed of micro- and mesopores such as SBA-15 or mesoporous zeolites. In this case it is nessesary to define an effective diffusion coefficent, which represents the combined resistance formed by all diffusion mechanisms present in the solid. Beside the diffusion mechanism the tortuosity of the diffusion pathway is also included in the effective diffusivity. In analogy to multiple resistance in an electric circuit the total effective flux of processes occuring in parallel are additive. Thus the total flux is in general given by the fast process. In contrast, for processes that are in series, the total flux is predominantly limited by the slower process. A combination of a diffusion in series of Knudsen and molecular diffusion in the gas phase of the solid in combination with surface and viscous flow in parallel gives the following expression for the effective diffusivity D_{eff}:

$$D_{\text{eff}} = \frac{1}{\tau}\left(\frac{1}{\frac{1}{D_{\text{K}}}+\frac{1}{D_{\text{m}}}}\right) + \frac{1}{\tau}K_{\text{H}}D_{\text{S}} + \frac{1}{\tau}q\cdot\frac{r^2}{8\mu} \tag{2.32}$$

where τ is the tortuosity of the corresponding diffusion pathway, K_{H} the Henry constant, D_{K}, D_{m}, and D_{S} the Knudsen, the molecular, and the surface diffusion coefficient.

2.3.3 Experimental methods to measure sorption kinetics

A number of theoretical and experimental techniques exists to study diffusion in porous materials. This section gives a brief overview over the most important techniques with a strong focus on the techniques that are relevant to this thesis.

Roughly, these methods can be divided in microscopic and macroscopic methods. Figure 2.10 gives an overview over the most important techniques sorted in the range of diffusivities that can be determined by these methods.

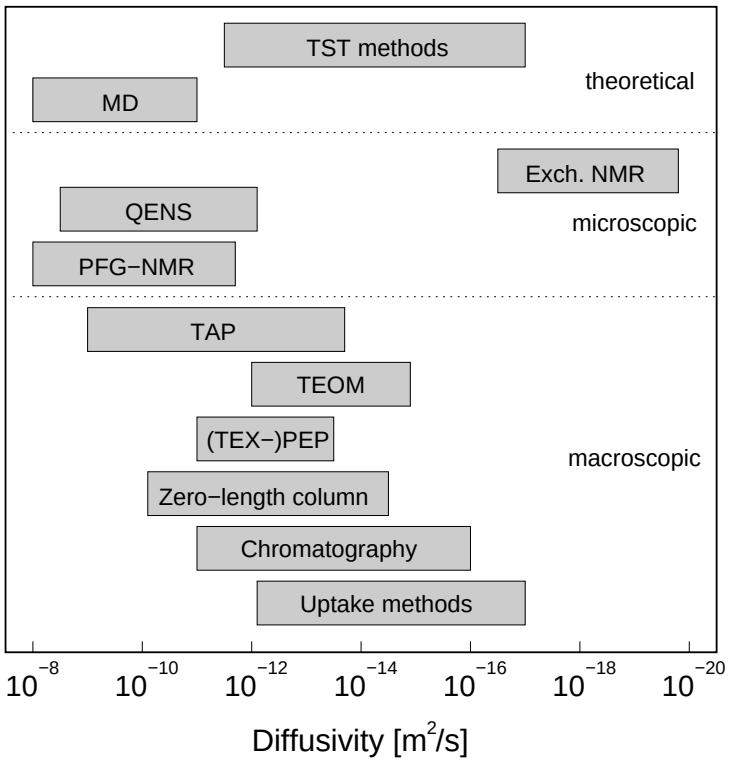

Figure 2.10: Range of diffusivities that can be determined with different methods. A diameter of 10 μm as assumed for the particle size, from Schuring (2002).

Gravimetric uptake

The direct measurement of the uptake by gravimetry is a very common technique to measure sorption kinetics. In principle, it can be modeled as a step change of the pressure or concentration in a batch system. The system response is called the step response. In order to derive a kinetic model, several experimental requirements must be fulfilled:

1. The bed is composed of uniform spherical particles.

2. Intra-crystalline diffusion is the only mass transfer resistance. All other sorption steps are fast, and, thus, in equilibrium.

3. The diffusivity is constant over the pressure step and the sorption isotherm is linear within this region.

4. The thermal conduction within a particle and the heat transfer between the particles of the bed is rapid. Thus, the only significant heat transfer resistance is at the external surface of the sample.

5. The temperature is constant throughout the sample. However, a time dependent difference in the temperature between the adsorbent and the surroundings is allowed. Diffusive heat transfer according to Newton's Law is assumed to be the governing heat transport mechanism.

According to these simplifications and assumption, the following solution for the uptake kinetics as given by Ruthven et al. (1980) is obtained:

$$\frac{c - c_0}{c_\infty - c_0} = 1 - \sum_{n=1}^{\infty} \frac{9\left[\left(q_n \cot q_n - 1\right)/q_n^2\right]^2 \cdot \exp\left(-q_n^2 \tau\right)}{1/\beta + 3/2\left[q_n \cot q_n \left(q_n \cot q_n - 1\right)/q_n^2 + 1\right]} \tag{2.33}$$

where τ is the dimensionless time constant of diffusion, i.e., $\tau = D/L^2 \cdot t$, and α and β are dimensionless parameters related to sorption curve and temperature history of the sample:

$$\alpha = \frac{\lambda A}{\rho C_\mathrm{p}} \tag{2.34}$$

$$\beta = \frac{\Delta H}{C_\mathrm{p}} \cdot \frac{\partial c_\mathrm{eq}}{\partial T} \tag{2.35}$$

where λ is the external heat transfer coefficent, A the external surface area per unit volume of adsorbent sample, ρ the effective density and C_p the effective heat capacity of the adsorbent sample, ΔH is the heat of adsorption, and c_eq the equilibrium adsorbed phase concentration. q_n is given by the roots of:

$$3\beta\left(q_n \cot q_n - 1\right) = q_n^2 - \alpha\big) \tag{2.36}$$

Equation (2.33) is a general expression for the analysis of uptake curves that are limited by diffusion or heat transfer, or controlled by both. In the limiting case of diffusion control, eiter $\alpha \to \infty$ or $\beta \to 0$, and equation (2.33) reduces to:

$$\frac{c - c_0}{c_\infty - c_0} = 1 - \sum_{n=1}^{\infty} \frac{1}{n^2} \cdot \exp\left(-n^2 \pi^2 \tau\right) \tag{2.37}$$

which is the well known expression for the analysis of uptake curves that are controlled by intra-crystalline diffusion. When diffusion is very rapid and the heat transfer is slow, the kinetics are entirely controlled by heat transfer. In this case α is small and the limiting case of heat transfer is obtained from the first term of equation (2.33):

$$\frac{c - c_0}{c_\infty - c_0} = 1 - \frac{\beta}{1+\beta} \exp\left(-\frac{\alpha\tau}{1+\beta}\right) \tag{2.38}$$

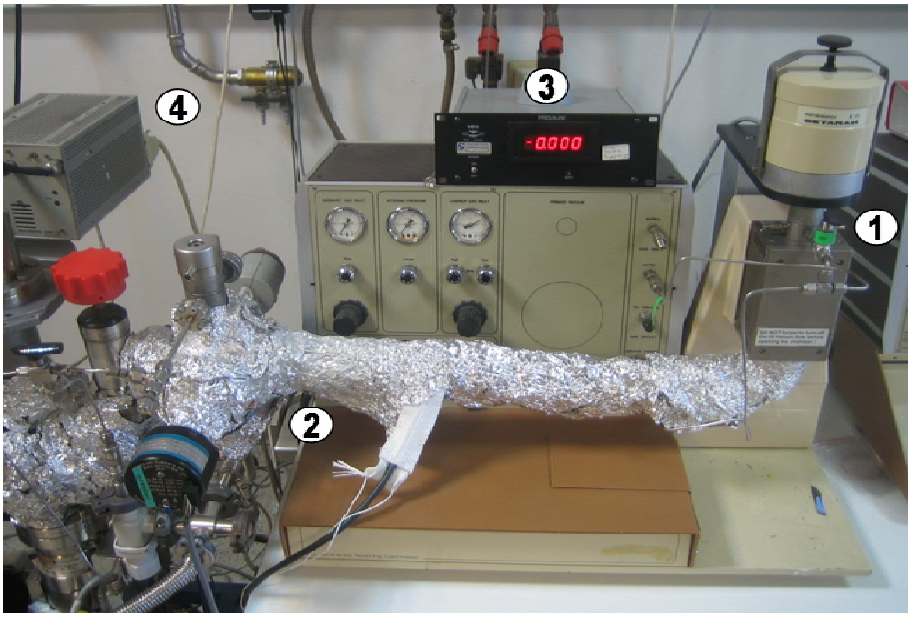

Figure 2.11: (1) (Thermo-)gravimetric high sensitivity microbalance from SETARAM, (2) vacuum chamber and sorbate dosing valve, (3) pressure transducer and (4) mass spectrometer for gas phase analysis.

In principle from the analysis of uptake curves by this expression it is possible to identify heat transfer limited systems, however, for certain values of α and β the shapes of the curves obtained from equation (2.37) and (2.33) are similar. Thus, it is not always possible to differentiate by a mathematical analysis of the uptake curves diffusion and heat limited systems. Experimentally, however, it is possible to identify heat effects by variation of the sample amount and sample configuration as α varies with the total external area of the sample.

Experimental set-up In Figure 2.11 the experimental set-up used in this thesis for the gravimetric uptake experiments is shown. It is composed of a (thermo-)gravimetric high sensitivity microbalance from SETARAM (TG-DSC 111) connected to a high vacuum system. Two pressure transducers in the pressure range of 10^{-4} mbar to atmospheric

pressures provide the option to measure in a broad pressure range. Probe gases are introduced into the system using a Balzers UDV 040 dosing valve. Adsorption and sample activation at temperatures up to 700 °C is possible.

Infrared spectroscopy in rapid scan mode

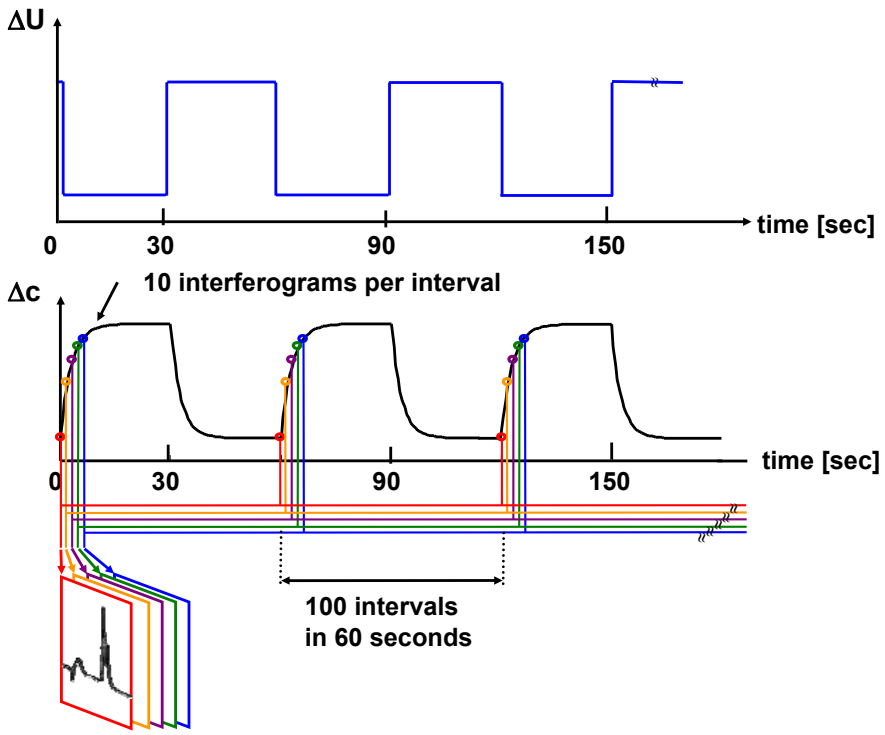

Figure 2.12: Data acquisition scheme for IR spectroscopy in rapid scan mode using a step change volume modulation. The rapid scan experiment is divided into n cycles of 60 s, each composed of 100 time intervals, which are co-added to a single measurement file.

A disadvantage of the gravimetric uptake technique is its limitation to rather slow transport processes with time constants larger than ∼100 s. This is due to the fact that most gravimetric systems have rather high relaxation times, and thus can not measure processes that are faster than the relaxation time of the system. Infrared microscopy in rapid scan mode is a possible solution to this problem. Very similar to the gravimetric technique, the diffusive system is exited by a step change in the sorbate pressure. The relaxation, that is, the responce of the system, is followed by infrared microscopy and not by gravimetry. In order to have a very high time resolution, the spectrometer is operated in the so called rapid scan mode. In this mode, a high time resolution is obtained by

repeating a certain experiment several thousand times in order to optain a single uptake curve by co-addition of these experiments. In figure 2.12 the data acquisition procedure is schematically shown.

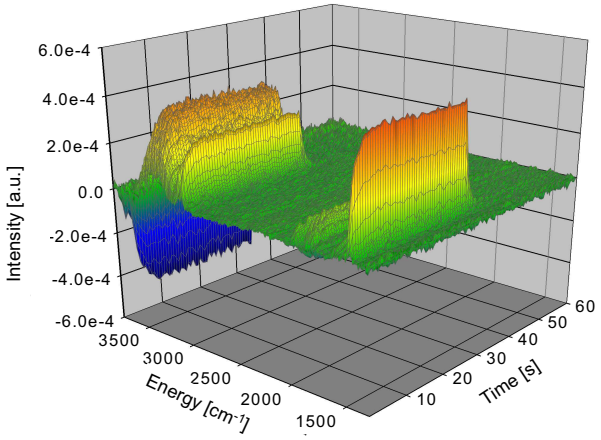

Figure 2.13: Time resolved uptake of benzene on H-ZSM-5 at 403 K by infrared microscopy plotted as a series of 100 difference IR spectra as obtained from a rapid scan experiment.

Experimentally, the reservibility of the process is achieved by applying only very small pressure changes of below 3% of the volume to the system. This also reduces the intrusion of heat effects. An other advantage of this method compared to the gravimetric uptake is the fact, that not only the total uptake of sorbate inside the sample can be observed, but also possible acidic sites inside the zeolite. This makes it possible to directly differentiate surface and bulk transport. In Figure 2.13 a typical time resolved uptake by infrared microscopy as obtained from a rapid scan experiment is shown.

Experimental set-up Figure 2.14 shows the experimental set-up used in this thesis for infrared microscopy and frequency responce experiments. It consists of four parts: an IR spectrometer (Bruker IFS 66v/S) (1) equipped with a transmission vacuum cell that is connected to a high vacuum system (2). Sorbate gases are introduced to the vacuum system via a dosing system using a Pfeiffer UDV040 dosing valve. A differential pressure transducer (Baratron MKS 161 A11) is used to measure the pressure of the sorbate gases in the system and a Pfeiffer TMU071 turbo molecular pump (70 l h^{-1}) to pump the system.

Solid pressed powder samples are placed in the IR cell on a gold ring sample holder. An electronics unit (3) with two Eurotherm 2416 and 2460-type temperature controllers control the temperature of the samples in a range of 298 K to 873 K and of the vacuum

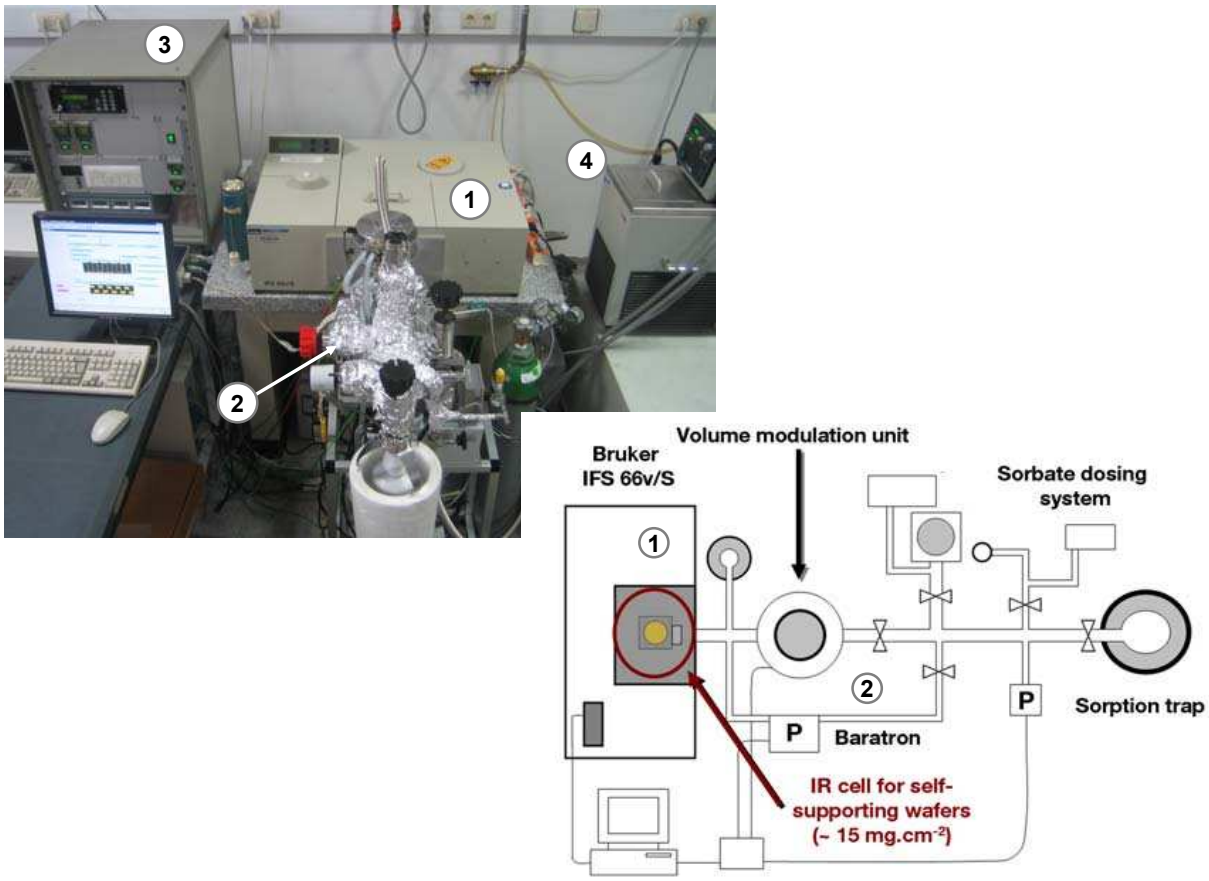

Figure 2.14: Photograph (top) and scheme (bottom) of the infrared and FR apparatus, composed of an IR spectrometer (1), vacuum apparatus (2), electronic controlling unit (3) and water filled cryostat (4).

system. Periodic volume change of the system is achieved via a magnetically driven modulation unit, being composed of a pair of flexible UHV bellows separated by a metal separator plate, placed horizontally between two electromagnets. The magnet polarization is controlled via a HP-Vee based program. For the rapid scan in-situ IR experiments, a constant modulation frequency of 0.0167 Hz is used. The magnets are held at a constant temperature of 313 K by a water-filled cryostat (4).

The amplitude of the volume modulations is limited to $\Delta V = \pm 5\%$ in order to minimize adiabatic effects due to compression of the gas volume, heat effects due to exothermic sorption processes, and further non-idealities of the system. Blank experiments are used in order to quantify this non-ideal behavior. The sorption kinetics were followed using a time resolution of 600 ms. A typical example of a rapid scan experiment is shown in figure 2.13.

Zero length column (ZLC)

A disadvantage of both gravimetric or infrared uptake analysis is the fact that both are operating under conditions that are potentially susceptible to mass and heat transfer limitations. The zero length column methods tries to minimize these effects by using a very small gas volume that is equilibrated with the sorbate of interest and then purged with an inert gas at a high flow rate in order to further decrease external transfer resistances.

Differential ZLC Model The basis of the ZLC model is formed by the Fick's second law of diffusion, which describes the mass balance through the solid-phase via diffusion. Mass transfer also occurs via the constant flow through the reactor bed. Both mass balances have to be solved simultaneously.

This technique has been applied mainly to gaseous systems (Brandani and Ruthven, 1995, 1996, Brandani et al., 2000a,b, Cavalcante and Ruthven, 1995, Duncan and Möller, 2000) but the application to liquid systems have also been reported (Brandani and Ruthven, 1995, Ruthven and Stapleton, 1993). The application to zeolite powders has been extended to pellet systems as well. The diffusion of non-hydrocarbon sorbates has been demonstrated. Furthermore, several criterions for the ZLC technique were also reported (Brandani and Ruthven, 1996, Brandani et al., 1998, Cavalcante et al., 1997, Duncan and Möller, 2002, Ruthven and Brandani, 2005).

Model assumptions The following assumptions were made during the model derivation:

1. The bed is isothermal.
2. No external film resistance.
3. The adsorption equilibrium isotherm is linear (Henry isotherm).
4. The gas hold-up in the fluid-phase was neglected in comparison with the adsorbed-phase accumulation.
5. The particles are spherical and of constant size.

Assumptions (1-3) can be controlled and checked during the measurement. The effect of assumption (4) has to be minimized by a clever design of the set-up. Assumption (5) is more critical and can be solved by analysis of the so called long time reagion of the desorption, i.e., only taking into consideration the biggest particles.

Model equations and solution The mass transfer via diffusion through spherical particles in radial coordinates is given by:

$$\frac{\partial q}{\partial t} = D_{\text{eff}} \cdot \left(\frac{\partial^2 q}{\partial r^2} + \frac{2}{r} \frac{\partial q}{\partial r} \right) \tag{2.39}$$

where q is the concentration of the adsorbed-phase, D_{eff} the effective diffusion constant and r the radial coordinate. The fluid-phase mass balance in one dimension is given by:

$$\frac{\partial c}{\partial t} = D_z \frac{\partial^2 c}{\partial z^2} - c \frac{\partial v}{\partial z} - v \frac{\partial c}{\partial z} - \left(\frac{1-\epsilon}{\epsilon} \right) \frac{\partial q}{\partial t} \tag{2.40}$$

where c is the concentration of sorbates in the fluid-phase, v the velocity of the fluid ϵ the porosity of the bed, D_z the axial diffusion coefficient and z the axial coordinate. Only taking the relevant terms under assumption of stationarity, under negligence of the fluid-phase hold-up, and introducing the volumes of solid-phase, one gets:

$$V_s \frac{\partial q}{\partial t} + F \cdot c(t) = 0 \tag{2.41}$$

In this equation V_s is the solid volume and F the fluid flow rate.

Equation (2.39) and (2.40) are a set of coupled differential equations. Brandani and Ruthven (1995) presented an analytical solution to this problem. It can be solved analytically using the above assumptions and initial and boundary conditions. The following set of equations is the analytical ZLC solution for the model and describes the desorption out of a porous three dimensional material:

$$\frac{c(t)}{c_0} = \sum_{n=1}^{\infty} \frac{2L}{\beta_n^2 + L(L-1)} \cdot \exp\left(-\beta_n^2 \frac{D_{\text{eff}}}{R^2} t \right) \tag{2.42}$$

$$0 = \beta_n \cdot \cot \beta_n + L - 1 \tag{2.43}$$

$$L = \frac{1}{3} \frac{F}{V_s} \cdot \frac{R^2}{K_{\text{H}} D_{\text{eff}}} \tag{2.44}$$

where R is the mean particle radius, K_{H} is the dimensionless Henry constant. β_n are the positive roots of equation (2.43) and L a value which introduces the flow rate into the set of equations.

Experimental set-up The typical experimental set-up was described Jiang and Eic (2003) and is shown in Figure 2.15.

The high pressure cylinder (1) contains the helium inert gas, which is subdivided into three different lines. These are the adsorption, the desorption and the sorbate line. Both adsorption and desorption are high flow rate streams, to minimize external

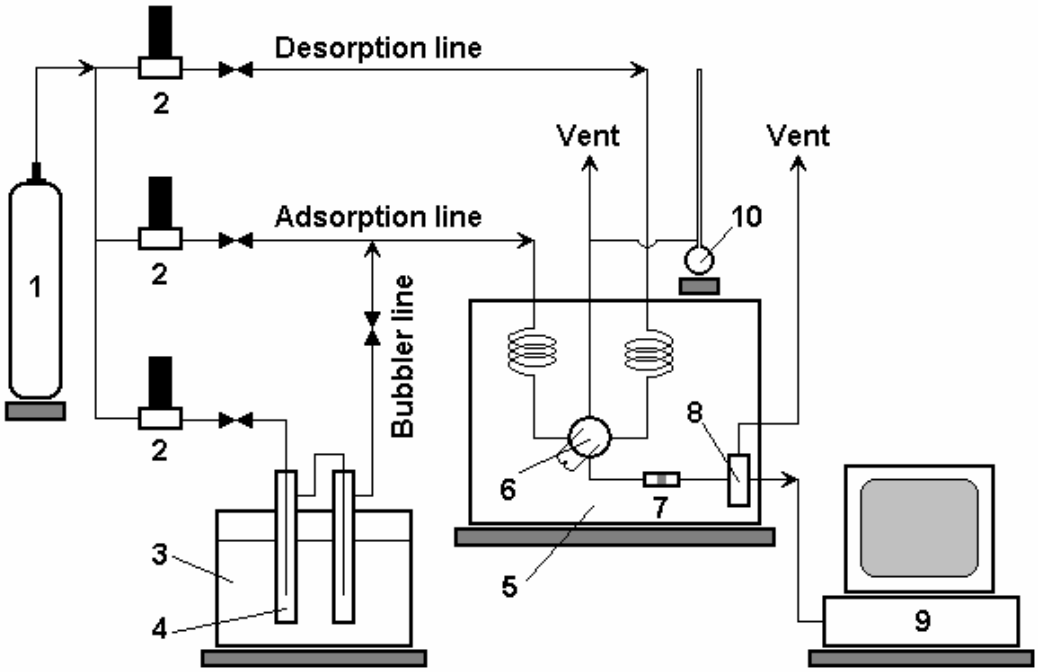

Figure 2.15: Schematic representation of the experimental ZLC set-up.

mass resistance during the measurements (2). To achieve a certain concentration of the sorbates in the adsorption stream, the sorbate line is used as a carrier stream and passed through a bubbler (4) containing the liquid hydrocarbons cooled by a thermostat (3) at a constant temperature of -10 °C to saturate the Helium stream with a certain amount of sorbate, which has to be low, in order to be in the Henry region of the adsorption isotherm. Both desorption and adsorption lines are connected through a 6-way switching valve (6).

The central part of a ZLC system is the zero length cell (7), which typically consists of a 1/8 Swagelok union. Two 1/8 sintered disks are placed on one end of the union to hold the powder samples between them. The outlet of the ZLC cell is connected to a flame ionization detector FID or to a mass spectrometer (8).

Frequency response (FR)

The frequency response technique is widely used to analyse the transport in porous materials. This technique, however, can not only be applied to diffusive systems, but in principle, to any kind of dynamic system. In the frequency response, typically, a system is pertubed periodically and its relaxation as a function of the frequency is measured. In order to eliminate heat effects and non-linearities in the responce, it is nessesary

to keep the perturbations very small. In the case of diffusive systems, the gas phase concentration or the pressure is varied and the system response is recorded. Due to the transport processes occuring inside the adsorptive material, a phase shift and a change in the amplitude of the pressure is obtained. An important feature of the linear frequency response method is the so called superposition principle. It says, that in the frequency space, multiple kinetic processes are additive. Thus this faciliates the identification of multiple processes that occur in parallel.

Differential FR model for batch adsorbers In the typical FR experiment for batch adsorbers, first a small amount of sorbate is equilibrated at constant pressure with the sorbent. Near equilibrium pressure perturbations of varying frequencies are achieved by small ($\pm 1\%$) sinusoidal or square-wave modulations of the system volume. A detailed derivation of the model equations can be found in the publications by Yasuda (1991, 1994a,b), Yasuda and Sugasawa (1984). In the following, only the solution of the differential FR model that is used to quantify the experimental FR data in this thesis is given.

The frequency response of such a system expressed as the in-phase and out- of-phase solutions of the mass balance of a closed volume subjected to periodic sinusoidal volume modulations is given by:

$$\frac{A_\mathrm{B}}{A}\cos\left(\theta-\theta_\mathrm{B}\right)-1=\sum_{1}^{n}K_\mathrm{FR}^{n}\cdot\delta_\mathrm{out}^{(n)} \tag{2.45}$$

$$\frac{A_\mathrm{B}}{A}\sin\left(\theta-\theta_\mathrm{B}\right)-1=\sum_{1}^{n}K_\mathrm{FR}^{n}\cdot\delta_\mathrm{in}^{(n)} \tag{2.46}$$

with

$$K=\frac{RT}{V}\cdot\frac{\partial\theta}{\partial p} \tag{2.47}$$

Herein K is related to the amount of molecules involved in the reversible sorption and desorption process, R is the molar gas constant, $\partial\theta/\partial p$ the gradient of the adsorption isotherm and V the total measurement volume. The number of diffusion processes is defined by n. For instance, in the case of a dual diffusion n equals 2.

A blank experiment without sorbent is required for quantification of the delays and of the non-ideal behavior of the apparatus itself. The corresponding phase $\theta-\theta_\mathrm{B}$ and amplitude A_B/A responses in equations (2.45) and (2.46) are obtained by subsequent Fourier transformation of the pressure square-waves or, in the case of a sinusoidal modulation, directly from the pressure waves. The in-phase and out-of-phase characteristic

functions δ_{in} and δ_{out}, are solutions to Fick's second law. In the case of diffusion in a planar sheet with the thickness $2L$, they are given by:

$$\delta_{\text{in}} = \delta_{1\text{S}} = \frac{1}{\eta}\left(\frac{\sinh\eta + \sin\eta}{\cosh\eta + \cos\eta}\right) \tag{2.48}$$

$$\delta_{\text{in}} = \delta_{1\text{S}} = \frac{1}{\eta}\left(\frac{\sinh\eta - \sin\eta}{\cosh\eta + \cos\eta}\right) \tag{2.49}$$

where $\eta = \sqrt{2\omega L^2/D}$, ω is the angular frequency and D the intracrystalline transport diffusion coefficient.

In the case of a finite rate adsorption process on the surface or supply of sorbate to the surface, i.e., if a so called surface barrier is present, the characteristic functions are given by (Yasuda, 1994a):

$$\delta_{\text{in}} = \left(\frac{a\kappa}{\omega}\right)^2 \cdot \frac{a + c\delta_{1\text{C}}}{\phi} \tag{2.50}$$

$$\delta_{\text{out}} = \left(\frac{a\kappa}{\omega}\right) \cdot \left(1 - \left(\frac{a\kappa}{\omega}\right) \cdot \frac{a\kappa/\omega + c\delta_{1\text{C}}}{\phi}\right) \tag{2.51}$$

where

$$\phi = \left(\frac{a\kappa}{\omega} + c\delta_{1\text{S}}\right)^2 + \left(a + c\delta_{1\text{C}}\right)^2 \tag{2.52}$$

is the rate constant of the surface barrier, and a and c are normalized parameters reflecting the amount of adsorbate in the pores c_{C} and on the surface c_{A}:

$$a = \left(\frac{\mathrm{d}c_{\text{A}}}{\mathrm{d}p}\right) / \left(\frac{\mathrm{d}\left(c_{\text{A}} + c_{\text{C}}\right)}{\mathrm{d}p}\right) \tag{2.53}$$

$$a = \left(\frac{\mathrm{d}c_{\text{C}}}{\mathrm{d}p}\right) / \left(\frac{\mathrm{d}\left(c_{\text{A}} + c_{\text{C}}\right)}{\mathrm{d}p}\right) = 1 - a \tag{2.54}$$

For most zeolites, the dominant amount of the sorbate is present within the micropores ($c \approx 1$).

In practice, zeolites usually do not have a uniform particle size, therefore, the characteristic functions have to be modified by using a normal distribution (Yasuda, 1994a):

$$\overline{\delta}(\overline{L}) = \frac{1}{\delta\sqrt{2\pi}} \int_0^\infty \delta \cdot \exp\left(-\frac{\left(L - \overline{L}\right)^2}{2\delta^2}\right) \mathrm{d}L \tag{2.55}$$

where $\overline{\delta}$ and $\overline{L}$ are the mean values of the characteristic function and of the crystal half thickness.

Experimental set-up The set-up used for the frequency response experiments is identical to the one for the rapid-scan infrared experiments shown in Figure 2.14. The only difference is the location of the sample. For the frequency response experiments, it is placed inside a small tube as powder sample and not as a pressed wafer as for the IR experiments.

Microscopic methods

All the previously described methods are methods belonging to the group of the so called macroscopic methods of diffusion measurement. These methods all have in common that the complete transport process from the gas phase into the porous solid is analysed. This includes possible surface effects and non-homogenities in the particle. Additionally, most macroscopic methods measure the kinetics in particle bed and not in single particles. This makes these methods susceptible to distributions of the particle size or other features influencing the overall transport. In contrast to these methods, microscopic methods provide direct information on the molecular mobility at microscopic scale. Surface effects do not directly influence the analysis and it is generally assumed that the short range mobility can be upscaled to long range mobility.

The two most common microscopic measurement techniques are the quasi-elastic neutron scattering (QENS) and the nuclear magnetic resonance (NMR) based techniques. In contrast to QENS, which only provides mobility information at the local scale below 1 nm, the pulse field gradient NMR (PFG-NMR) can also be applied over longer distances in order to follow the movement of molecules over longer distances. It is, however, still limited to distances smaller than the crystal size. Since the experiment is carried out in steady state, without the application of a concentration gradient, the self diffusivity is directly obtained from the Einstein equation (2.22). The major development and application of the PFG-NMR to measure diffusivities in zeolites was done by Kärger, Pfeiffer and their collaborators. Full detail can be found in the following articles: (Kärger, 2003, Kärger and Ruthven, 1989, Kärger et al., 1992, Krishna, 2009, Krishna and van Baten, 2009, Ruthven, 2007b).

3 Diffusion Pathways of Benzene, Toluene and p-Xylene in MFI

This chapter was published in the journal Microporous and Mesoporous Materials as research article:

Diffusion pathways of benzene, toluene and p-xylene in MFI
Oliver C. Gobin, Stephan J. Reitmeier, Andreas Jentys, and Johannes A. Lercher, Microporous and Mesoporous Mat.; **2009**; 125(1-2), pp 3-10

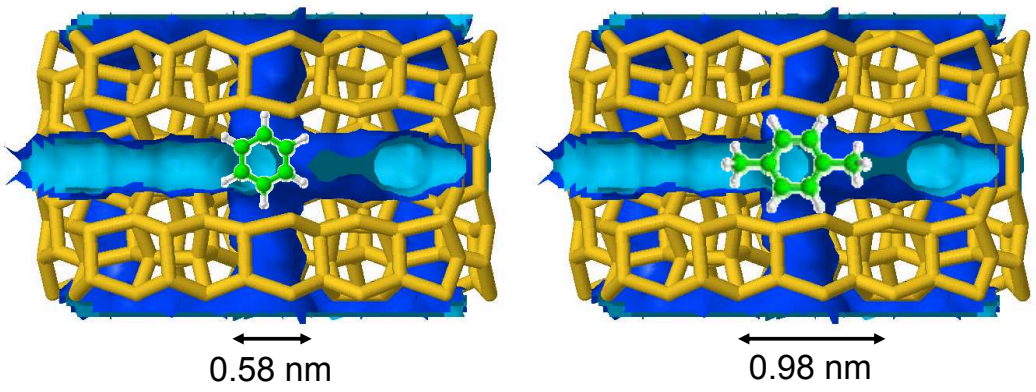

Abstract The diffusion of alkyl-substituted aromatic molecules in H-ZSM-5 was investigated by means of the frequency response method decoupling particle size effects and intracrystalline diffusion. For zeolite crystals above 5 μm average diameter, the transport in the zeolite pores exerts significant effect on the overall transport causing anisotropic diffusion as the aspect ratio of the aromatic molecules increases. Diffusion of benzene is nearly isotropic, while p-xylene shows marked differences between the diffusive processes in the straight and sinusoidal channel system of ZSM-5. The isotropic diffusion of benzene is rationalized on the basis of its ability to reorient between the two channel systems without major hindrances. For p-xylene, switching between the channels is only possible by energetically unfavorable rotational motions leading to a low probability for changing between both channel system.

3.1 Introduction

The molecular level understanding of catalytic and sorptive processes in micorporous materials is essential for the developing and tailoring of next generation materials (Davis, 2002). Among the few zeolites used industrially in a large scale H-ZSM-5 (MFI structure) (Kokotailo et al., 1978, Olson et al., 1981) is a key component in catalytic and separation processes (Corma, 1995). Its complex crystal structure and widely varying external morphology has led to complex and ambiguous interpretations of the transport processes in its pores. To contribute to the understanding of individual transport steps in this material transient techniques have been explored by our group and have led to a detailed understanding of the elementary steps during the entrance of rigid molecules into the MFI pore system (Jentys et al., 2006, Mukti et al., 2007, Reitmeier et al., 2008).

In the present study we revisit the use of the frequency response (FR) technique to explore and model transport diffusivities in complex, but larger MFI crystals. Being a relaxation technique, it measures the phase lag and the amplitude change by subjecting a system to an oscillating pressure or concentration perturbation of varying frequency and constant amplitude. Naphtali and Polinski (Naphtali and Polinski, 1963) were the first to apply this technique for determination and interpretation of adsorption kinetics. Yasuda extended it to study the diffusion in porous solids such as zeolites (Yasuda, 1994a). The main advantage of the FR technique compared to other transient methods is its unique ability to differentiate between several kinetic processes. This is achieved by the transformation of the time dependent diffusion information into the corresponding frequency domain. In the frequency domain, multiple processes are additive, and thus easier identified and deconvoluted compared to time dependent uptake or desorption processes. However, the interpretation of the frequency response is complex and may lead to ambiguity in case of multiple processes. Particle size distributions of powdered samples, for instance, lead to broadening of the frequency response. Moreover, multiple diffusion processes with different time constants, and heat or bed effects are also known to change the shape of the frequency response by masking the intracrystalline diffusion (Sun and Bourdin, 1993, Sun et al., 1993).

Diffusion processes with time constants differing by at least one order of magnitude can be identified by bimodal phase functions, i.e., showing two maxima in the case of a binary diffusion of different molecules or in the case of single component diffusion in a porous solid with different diffusivities in two distinct and unconnected pore systems. If the diffusivities do not differ at least by one order of magnitude only a broadening of the phase function will be observed.

Macroscopic methods, such as the frequency response method, are influenced by

all steps involved during the transport of gas phase molecules into the porous particle (Jentys et al., 2006, Reitmeier et al., 2008, 2009b). These are in particular the sorption of a molecule on the external surface, described by the probability that a gas phase molecule is adsorbed on the external surface of the particle after collision (sticking probability), the entering into the pore and the intracrystalline diffusion processes. The mutual relation of these elementary processes will subtly determine the overall process and it has been unclear whether or not isolable rate determining steps exist.

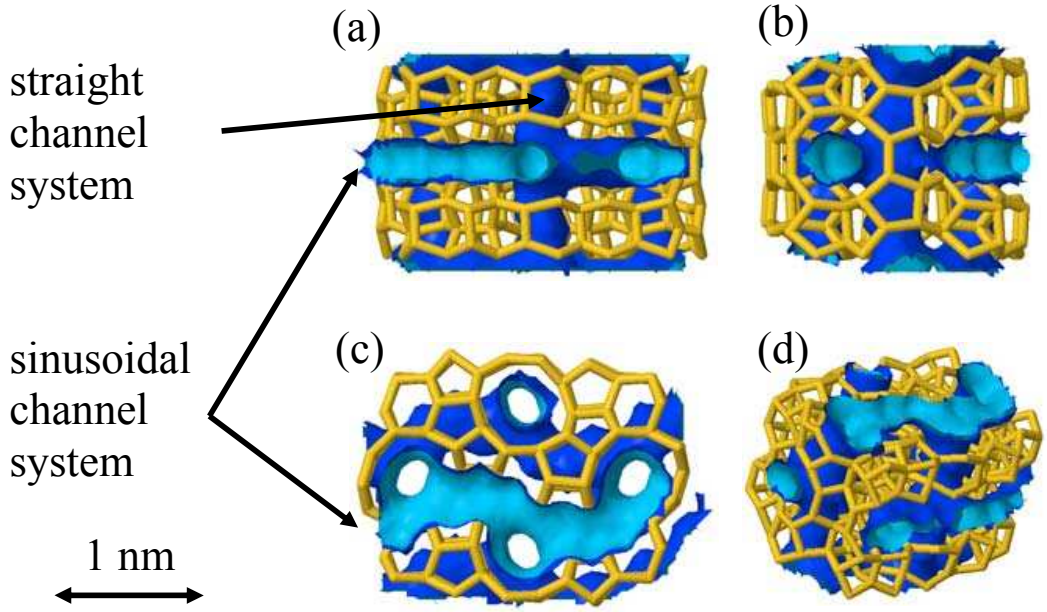

Figure 3.1: Schematic representation of the silicalite-1 / ZSM-5 structure. (a) front [001], (b) left [100], (c) top [010], and (d) isometric projection [111]. Generated from the database of zeolite structures (Baerlocher et al., 2001).

MFI has two interconnected channels with slightly different pore diameters and pore shapes. The slightly elliptical channels are generally denoted as straight channels with a diameter of about 0.53 x 0.56 nm and as sinusoidal channels, which are slightly smaller with a diameter of 0.51 x 0.55 nm (Kokotailo et al., 1978, Olson et al., 1981). Between both channel systems intersections of about 0.9 nm (Liu et al., 2004) exist. The Si framework structure and the pore surface based on the ionic radii of the zeolite framework atoms are shown in Figure 3.1 from four different projections (Baerlocher et al., 2001). The front projection [001] shows the sinusoidal channel system horizontally along the (001) plane and the straight channel system vertically along the (001) plane. From the [010] projection, the sinusoidal shape of the channel system can be seen. Rotation of the bulkier molecules along the (010) plane is only possible at the channel intersections, as

can be easily seen on the basis of Figure 3.1a. Moreover, the [100] projection in Figure 3.1b indicates that rotation of the bulkier molecules along the (100) plane is strongly hindered. Thus, reorientation of rigid molecules with a maximum length larger than the pore diameter of the straight or sinusoidal channels is demanding. Certainly, the necessary reorientation for transport in the sinusoidal channels would make transport in these channels slower than transport in the straight channel inducing anisotropic diffusion. In the case of smaller and sterically less constrained molecules an isotropic diffusion is observed as recently reviewed by (Ruthven, 2007a). Note in this context that Shen and Rees (1991, 1993, 1995) observed for the diffusion of p-xylene in silicalite-1 or ZSM-5 a bimodal frequency response, which was ascribed to the different diffusivities of the molecules in the two types of channels. In contrast, for silicalite-2 (its pore system consists of two interconnected straight channels with identical pore diameter) only one diffusion process was observed (Shen and Rees, 1993). While this is direct evidence for anisotropic diffusion of p-xylene in ZSM-5, there is still a debate if in the case of interconnected pore structures the two processes can be monitored by a macroscopic technique.

In this contribution, the transport diffusion of benzene and derivatives with increasing degree of methyl-substitution, i.e., toluene and p-xylene, in H-ZSM-5 was investigated using the frequency response method. As the presence of more than one transport pathway and the presence of a wide distribution of particles in the sample as well as thermal effects could lead to similar effects on the characteristic functions in frequency response experiments, emphasis was laid upon showing that both latter effects can be excluded to dominate in the results described here.

3.2 Experimental section

3.2.1 Materials

Polycrystalline H-ZSM-5 was provided by Süd-Chemie AG with a Si/Al ratio of 45. Particle size distributions (PSD), or more precisely number densities of particles, with a diameter of 4.4 ± 1.5 μm were obtained by dynamic light scattering (DLS). In addition, the particle size distribution was estimated by scanning electron microscopy (Figure 3.2). An average diameter of 3.9 ± 1.2 μm was obtained, which is in acceptable agreement with the results by DLS. The respective standard deviations were obtained by a Gaussian fit to the data. The particle size distributions obtained by DLS and SEM are compared in Figure 3.3. For diffusion measurements benzene, toluene, and p-xylene in spectroscopic grade (GC standard, $> 99.96\%$) provided by Sigma-Aldrich were used without further

purification. The liquids were treated by several pump-and-freeze cycles to remove gaseous contaminations and afterwards slightly heated before usage.

3.2.2 Physicochemical characterization

Dynamic light scattering measurements were performed on a Malvern Zetasizer Nano ZS. The samples were dispersed in water and kept in an ultrasonic bath prior to the measurements that were repeated at different concentrations several times. Scanning electron microscopy (SEM) images were recorded on a REM JEOL 5900 LV microscope operating at 25 kV with a resolution of 5 nm and a nominal magnification of $3.0 \text{x} 10^6$. The characterization of the acid sites with respect to concentration and distribution was described previously (Zheng, 2002).

3.2.3 Frequency response experiments

For the frequency response experiments, 30 mg of the powdered samples were ground and 30 mg were carefully dispersed on several layers of quartz wool at the bottom of a quartz tube in order to avoid artifacts from bed- depth effects. The sample tube was connected to a vacuum system, placed inside a heating oven and pumped to 10^{-7} mbar at room temperature. The samples were afterwards heated to 823 K with a ramp of 10 K/min and activated under vacuum below 10^{-7} mbar for one hour to remove adsorbed water. The sorbate gases were added with a partial pressure of 0.3 mbar into the system at temperatures between 333 and 423 K. After the sorption equilibrium was fully established, the volume of the system was modulated periodically by two magnetically driven plates sealed with UHV bellows. The modulation resulted in a square-wave perturbation of the system volume with an amplitude of 1%, and was performed in the frequency range of 0.001 to 5 Hz. The pressure response of the system to the volume perturbation was recorded with an inon-line Baratron pressure transducer (MKS 16A11 TCC). The amplitude and the phase lag of the frequency response were obtained by Fourier transformation of the pressure data. Nonlinear parameter fitting of the theoretical characteristic functions to the experimental frequency response was performed by using the CMA evolution strategy in Matlab (Hansen, 2006). The root mean squared error normalized to the variance of the data (NRMS error) was used as the objective function to be minimized. To ensure that the globally optimal parameter set was found, each optimization run was repeated three times with varying parameter sets of the evolution strategy.

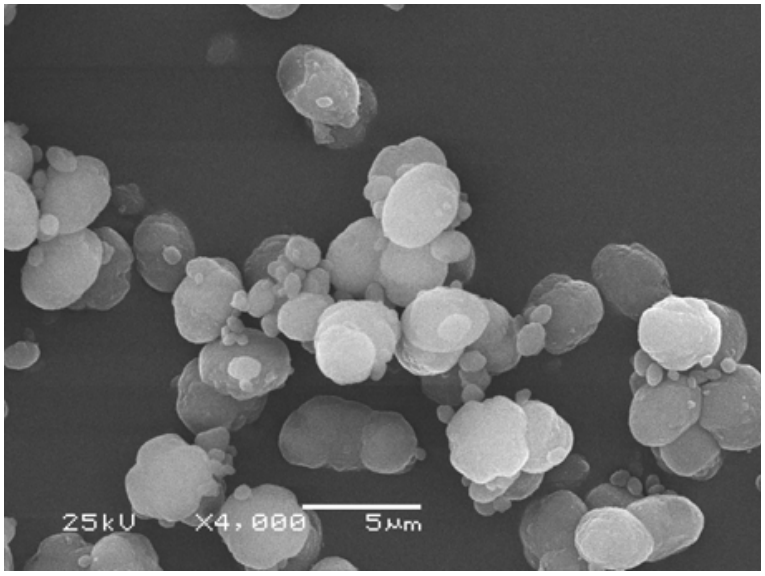

Figure 3.2: Scanning electron micrograph showing the primary particles of the H-ZSM-5 sample.

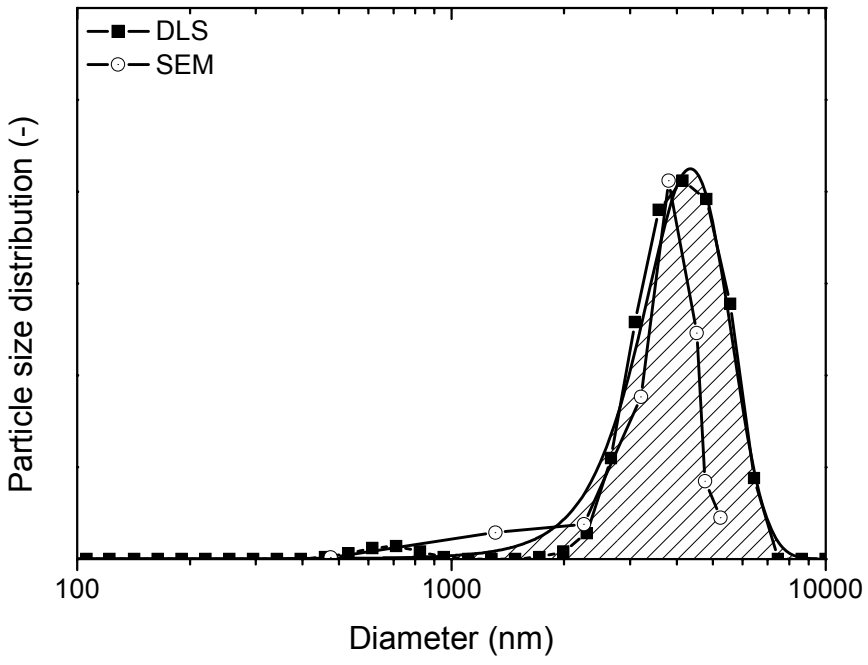

Figure 3.3: Comparison of the number densities of particles obtained by DLS and SEM. The shaded area represents a Gaussian fit to the experimental DLS data with an average diameter of 4.39 μm and a standard deviation of 1.49 μm.

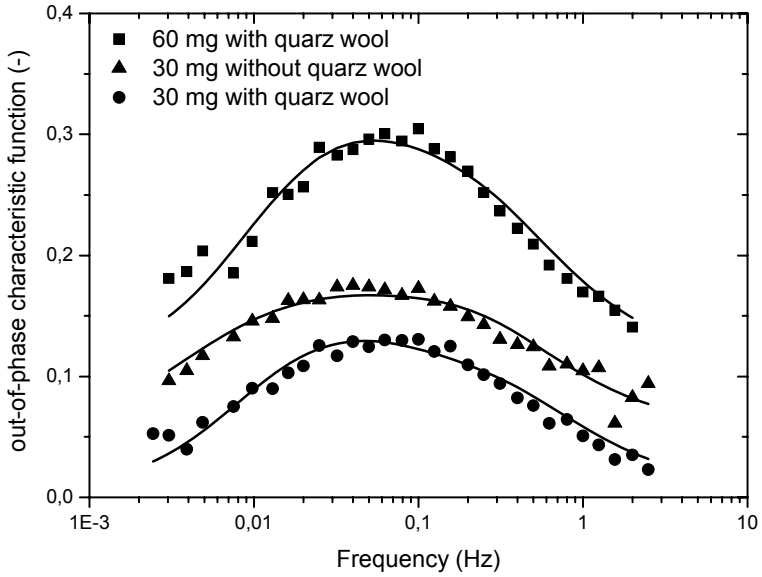

Figure 3.4: Out-of-phase frequency responses of toluene at 403 K. The sample amount and the way the sample was placed in the sample tube were varied in order to check for heat and bed-depth effects. The curves are shifted by 0, 0.05, and 0.10 respectively.

The influence of heat or bed-depth effects was checked by variation of the sample amount and by the way the sample was placed in the sample tube, i.e., with and without dispersing the sample on quartz wool. The frequency responses are shown in Figure 3.4. In all cases the same frequency response was observed and therefore, we can exclude heat or bed-depth effects to be present to the best of our knowledge. In addition, modeling assuming a non-isothermal diffusion (Sun and Bourdin, 1993, Sun et al., 1993) where the time constant of heat transfer is in the same order as for the diffusion process was carried out for all data, and the consistency of the parameters was checked. The resulting fit was poor in many cases and the obtained time constants were inconsistent, which gives further confirmation that heat effects are not significant in the present frequency response experiment under the conditions studied.

3.2.4 Model building

In order to differentiate between broadening effects of the frequency response either caused by a particle size distribution of the sorbent crystals or by multiple diffusion processes in the H-ZSM-5 samples, a careful evaluation of the data is required. First, a model taking into consideration either a Gaussian particle size distribution or the

experimental particle size distribution obtained by DLS and a surface resistance was fitted to the experimental data. The modeling procedure was repeated for each sorbate using the average standard deviations of the Gaussian distribution obtained by the first modeling. In order to study the contribution of both, particle size distribution and multiple diffusion processes on the broadening of the frequency response, subsequent modeling was also performed using a model assuming two diffusion processes in addition to a particle size distribution. The standard deviation of the distribution was set constant to the value obtained by DLS.

3.3 Results

The diffusivities of benzene, toluene, and p-xylene (all having the same minimum kinetic diameter) at temperatures between 343 and 403 K, and the fitting parameters are given for both samples in rable 3.1. All diffusivities increase as function of temperature and are consistent with respect to the molecule dimensions and to diffusivities measured by other methods (Brandani et al., 2000a, Ruthven, 2007a, Shen and Rees, 1991). The sterically more demanding molecules (toluene and p-xylene) show a lower diffusivity than benzene (see Figure 3.5). The apparent activation energies of diffusion increase with the molecule size and with degree of substitution from 20 to 30 kJ/mol (see Table 3.1) in agreement with the literature (Brandani et al., 2000a).

		T	loading	$D \cdot 10^{13}$	K	NRMS-Error	E_A
		°C	molec/u.c.	m^2/s	(-)	(-)	kJ/mol
benzene		343	1.65	3.09	0.84	0.28	
$L =$	$4.39 \cdot 10^{-06}$ m	373	0.83	5.28	0.57	0.21	21
$\sigma =$	$2.22 \cdot 10^{-06}$ m	403	0.34	9.50	0.46	0.17	
toluene		343	2.69	1.35	1.00	0.25	
$L =$	$4.39 \cdot 10^{-06}$ m	373	1.39	2.81	0.65	0.32	28
$\sigma =$	$3.18 \cdot 10^{-06}$ m	403	0.66	5.83	0.42	0.17	
p-xylene		343	3.60	1.14	0.91	0.26	
$L =$	$4.39 \cdot 10^{-06}$ m	373	2.15	2.46	0.78	0.3	29
$\sigma =$	$4.28 \cdot 10^{-06}$ m	403	1.09	5.04	0.41	0.35	

Table 3.1: Diffusivity data, loadings, loadings, and fitting parameters obtained for a theoretical model assuming one processes with a Gaussian particle distribution as additional fitting parameter

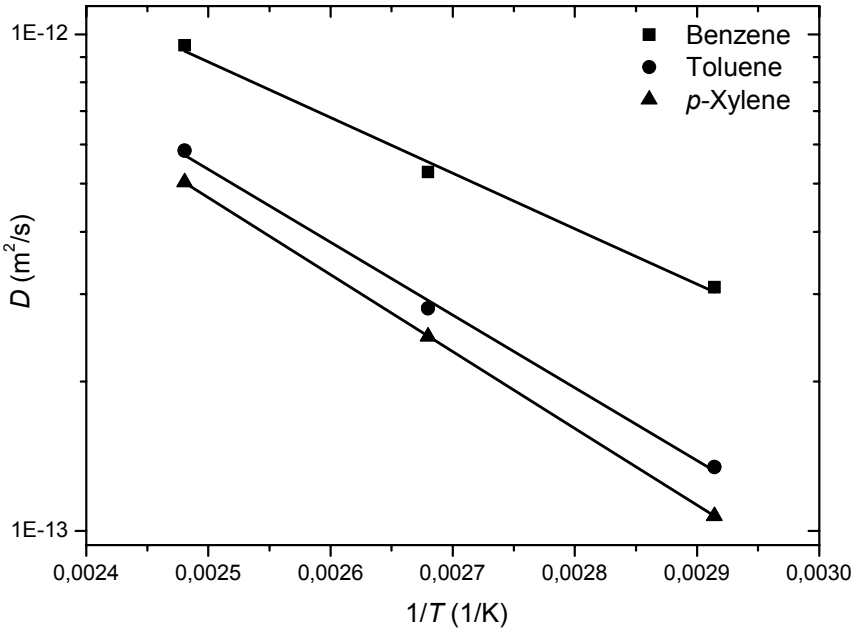

Figure 3.5: Arrhenius plot of benzene, toluene, and p-xylene for a single diffusion model with a Gaussian particle size distribution and surface resistance.

The standard deviations of the Gaussian particle size distribution obtained by fitting the experimental frequency responses are also summarized in Table 3.1. With increasing degree of substitution a broader distribution, characterized by an increasing standard deviation, is needed to adequately describe the frequency response indicating a fundamental problem with this approach. The representative frequency responses of the three sorbate molecules are shown in Figure 3.6. Even by directly comparing the frequency response, the significantly broader maxima in the phase function for p-xylene compared to benzene can be clearly observed.

The widths of the PDS obtained from the modeling of the frequency responses assuming only one diffusion process are in all cases larger (summarized in Table 3.1) than the equivalent PDS derived the Gaussian fit to the DLS data (the most realistic description of the PDS, see Fig. 3). The distribution obtained by SEM is slightly narrower, however, it fits very well the distribution by DLS. As the latter distribution is not an ideal Gaussian function, modeling using the experimental particle size distribution (obtained by DLS) was performed, but the results could not be differentiated from those assuming an ideal Gaussian distribution. This suggests that the particle size distribution cannot account for the widths and shapes of the characteristic FR functions.

Because the shape of the FR functions also varies with the type of molecule, phenomena

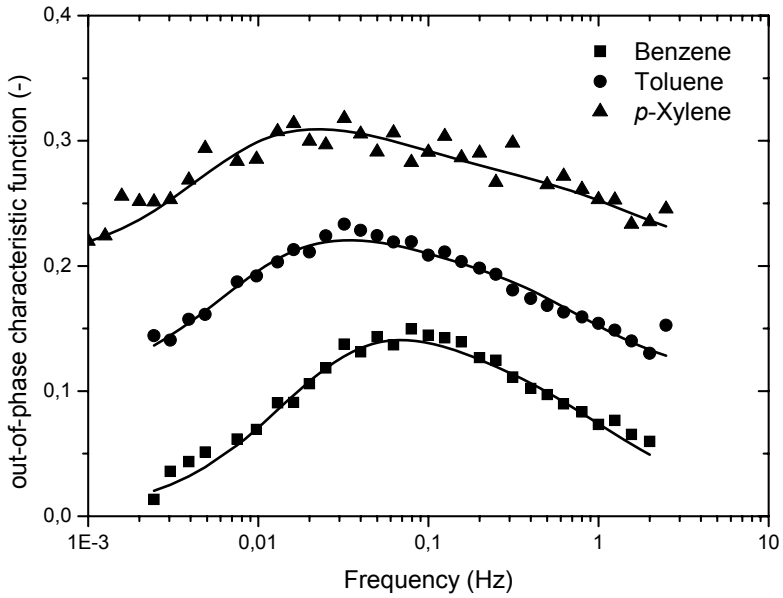

Figure 3.6: Out-of-phase frequency responses of benzene, toluene, and p-xylene at 403 K. The fits were obtained using a single diffusion model with a Gaussian particle size distribution and taking into consideration a surface resistance. The curves are shifted by 0, 0.1, and 0.2 respectively.

	T	D_1	D_2	D_{mean}	K_1	K_2	NRMS	E_{A1}	E_{A2}	E_{Amean}
	°C	10^{13} m^2/s	10^{13} m^2/s	10^{13} m^2/s			Error	kJ/mol	kJ/mol	kJ/mol
benzene	343	4.95	0.51	3.30	0.56	0.33	0.27			
	373	7.98	1.02	5.82	0.40	0.18	0.20	17	26	20
	403	11.20	2.08	9.02	0.35	0.11	0.16			
toluene	343	4.01	0.40	1.88	0.41	0.59	0.23			
	373	7.52	0.98	3.12	0.17	0.35	0.17	19	27	23
	403	11.00	1.49	7.74	0.23	0.12	0.20			
p-xylene	343	3.9	0.17	1.16	0.25	0.69	0.24			
	373	5.65	0.44	2.26	0.28	0.52	0.28	20	27	23
	403	10.90	0.93	3.85	0.12	0.29	0.33			

Table 3.2: Diffusivity data and additional fitting parameters obtained for a theoretical model assuming two processes with a constant Gaussian particle distribution of $1.49 \cdot 10^{-6}$ m

besides a broad particle size distribution must be included. At this point, two diffusion processes, as suggested in the previously literature, were taken into account to explain the distinct broadening of the frequency response with the size of the molecule used. In order to quantify the contributions of the particle size distribution and of the two diffusion processes to the overall broadening of the frequency response, modeling using a dual diffusion model was performed and the diffusivities are given in Table 3.2. The quality of the fits, indicated by the normalized root mean squared error (NRMS error), is substantially better than the one obtained by using a single process diffusion model (Table 3.1).

For all molecules the diffusivity of the fast process D_1 is higher and the diffusivity of the slow process is lower compared to the diffusivity obtained by a single diffusion model. For benzene the contribution of the slower process is minor compared to the cases of toluene and p-xylene (see Figure 3.7). In fact, for benzene the frequency response could also be modeled reasonably by assuming only one process in agreement with earlier studies (Jobic et al., 2000, Ruthven, 2007a, Snurr et al., 1993).

For toluene and p-xylene the difference between D_1 and D_2 increases in average from 8 to 15, respectively. This can be related to the broader frequency response of p-xylene, which requires a stronger separation of the diffusion processes, leading to the interesting effect, that the first diffusion process D_1 has nearly the same value for all molecules (see Figure 3.7), while the diffusion process D_2 is slower for p-xylene compared the toluene and benzene. The contribution of the two processes, however, is different for these molecules. This can be seen on the basis of K_1 and K_2, describing the relative contribution of both processes. In the case of benzene, the diffusion is dominated by the

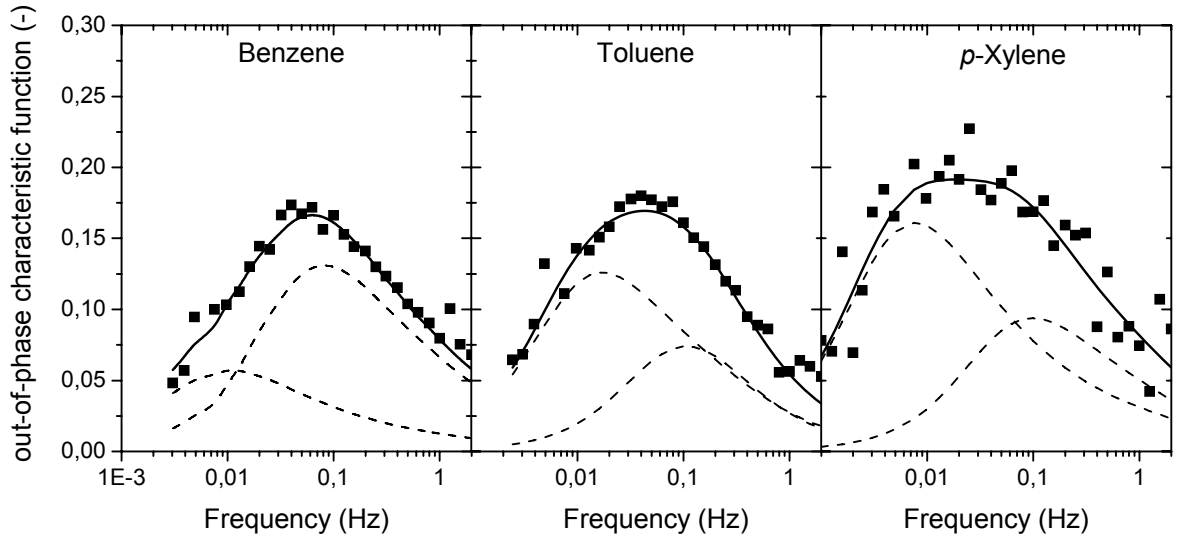

Figure 3.7: Out-of-phase frequency responses of benzene, toluene, and p- xylene at 373 K for a theoretical model assuming two processes. The dotted lines correspond to the two diffusion processes.

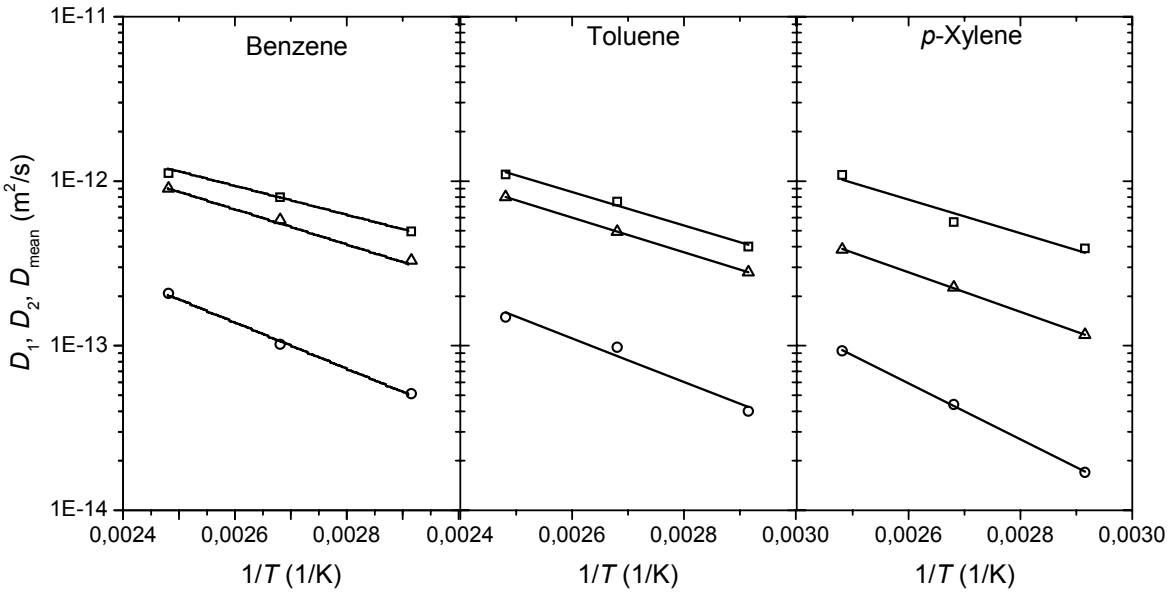

Figure 3.8: Arrhenius plots of benzene, toluene, and p-xylene for a theoretical model assuming two processes, a Gaussian particle distribution and surface resistance. The fast process D_1 is represented by a square, D_2 by a circle, and D_{mean} by a triangle.

first process, i.e., $K_1 > K_2$, while for p-xylene the contribution of the slower process D_2 is stronger ($K_2 > K_1$). Toluene lies in between. The resulting D_{mean} shows the same trend as the diffusivities in Table 3.1 obtained by assuming a single diffusion process. The temperature dependencies of D_1, D_2, and Dmean are shown by Arrhenius plots in Figure 3.8. For all molecules, the observed activation energy of the process (related to D_1) is significantly smaller compared to that of the second process.

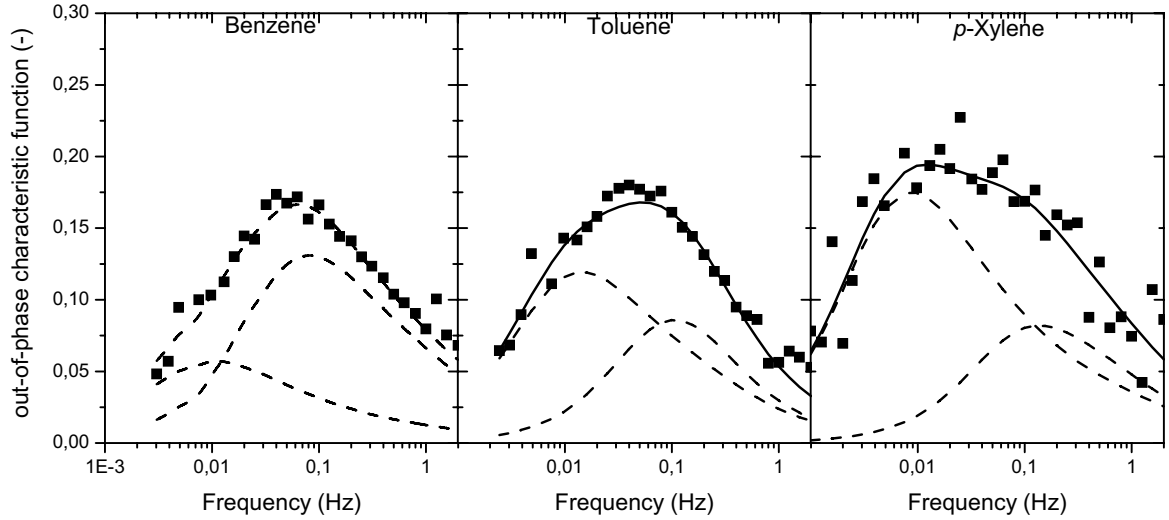

Figure 3.9: Out-of-phase frequency responses of benzene, toluene, and p- xylene at 373 K for a theoretical model assuming two processes with constant D_1. The dotted lines correspond to the two diffusion processes.

In a second step, these results were refined by assuming a fixed diffusivity for the faster transport pathway (D_1). This boundary condition was introduced with the speculation in mind that transport of molecules with identical minimum kinetic diameters in the straight channel of MFI should be invariant. The quality of the fitting process is comparable by these measures without changing the overall trends observed as can be seen in Table 3.3 and Figure 3.9.

3.4 Discussion

Bimodal frequency responses are usually observed for solids with two separated and unconnected channel systems, showing different diffusivities. Thus, after having excluded other possible factors for broadening of FR functions, the results of this study indicate that two distinct transport processes in the pores of MFI occur. However, as the two

	T	D_1	D_2	D_{mean}	K_1	K_2	NRMS	E_{A1}	E_{A2}	E_{Amean}
	°C	10^{13} m^2/s	10^{13} m^2/s	10^{13} m^2/s			Error	kJ/mol	kJ/mol	kJ/mol
Benzene	343	4.95	0.51	3.30	0.56	0.33	0.27			
	373	7.98	1.02	5.82	0.40	0.18	0.20	17	26	20
	403	11.20	2.08	9.02	0.35	0.11	0.16			
Toluene	343	4.95	0.38	2.13	0.38	0.61	0.22			
	373	7.98	0.81	3.45	0.21	0.36	0.18	17	27	23
	403	11.20	1.49	7.49	0.21	0.13	0.19			
p-Xylene	343	4.95	0.18	1.36	0.23	0.70	0.24			
	373	7.98	0.50	2.67	0.23	0.56	0.28	17	30	23
	403	11.20	0.92	4.27	0.14	0.29	0.34			

Table 3.3: Diffusivity data and additional fitting parameters obtained for a theoretical model assuming two processes with a constant Gaussian particle distribution of $1.49 \cdot 10^{-6}$ m. The diffusion coefficient D_1 was set constant to the value of benzene

types of channels are highly interconnected in ZSM-5, the question arises, how in such an environment a bimodal frequency response can be observed. In this context it should be emphasized that the relative contribution of two diffusion pathways increases as the maximum length of the aromatic molecules increases, i.e., in the sequence benzene < toluene < p-xylene. This leads to the puzzling suggestion that the larger aromatic molecules tend to stay in a particular pore and do not strongly mix between the channels at the intersection. The situation is even more complex, as the FR technique measures overall diffusivities encompassing all steps in the transport process, thus, requiring that the individual contributions are to be analyzed in order to understand the behavior in the pores.

The overall transport from the gas phase into the bulk of a ZSM-5 particle can be described by a series of consecutive elementary steps and two parallel diffusion processes as shown in Figure 3.10. We showed recently that the overall process of adsorption is dominated by a subtle balance between the initial adsorption on the external surface and the process of entering the micropores (Reitmeier et al., 2008). The rate of transport in the pores and especially the rate difference between the two diffusion pathways play a minor role in small crystals (below 100 nm). Under these conditions benzene, toluene and p-xylene appear to diffuse isotropically. While this was shown conclusively on a qualitative basis, a detailed quantitative analysis of the transport mechanism to describe the adsorption and diffusion properties of small (below 100 nm) ZSM-5 particles is currently under preparation.

Applying this model to large particles, the rate of transport in the particle contributes

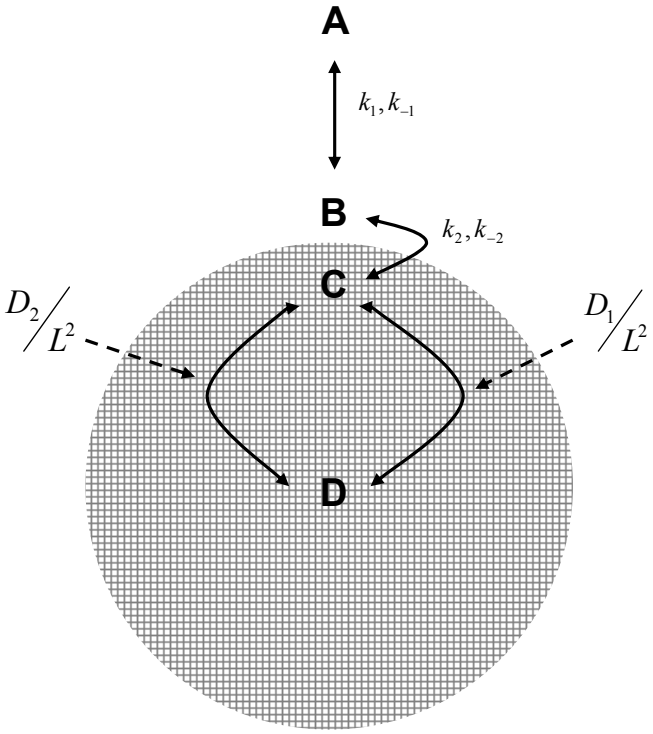

Figure 3.10: Schematic representation of the complete transport process from the gas phase (A), onto the particle surface (B), into the ZSM-5 pore sytem (C), and inside the particle (D). The two diffusion pathways through the straight and sinusoidial channels are represented by D_1 and D_2, the rate constants for each elementary step by k.

markedly to the overall adsorption rate. Thus, for small particles the processes at the external surface are dominating the rates of sorption, while with increasing particle size the importance of intracrystalline diffusion increases. This leads potentially to a stronger impact of the anisotropic diffusion in the particle.

The overall transport of benzene appears to occur through infrequent hops between adsorption sites predominantly in the intersections. This is also seen through the quantitative adsorption of benzene localized at the Brönsted acid sites indicating a residence time which is long on the timescale of IR vibrations (Jentys et al., 2006). Computational modeling (Snurr et al., 1994) suggests that reorientation of benzene within the channels is facile. Computed trajectories of benzene clearly indicate that benzene diffuses in both channels and is capable of switching between them without major hindrances.

In case of toluene and p-xylene the motion is more constrained, as, e.g., p-xylene

is only able to rotate in the intersections along the axis horizontal to the plane of the aromatic ring, as can be seen in Figure 3.11 as well as in Figure 3.1. Perpendicular rotations along the (100) plane are energetically difficult, as the length of p-xylene (0.99 nm) (Choudhary et al., 1997) exceeds the maximum diameter of the intersection (0.9 nm) (Liu et al., 2004). However, to switch from the straight into the sinusoidal channel this rotational motion has to occur, which requires passing the high energy barrier needed to distort the zeolite framework and/or the p- xylene molecule. Compared to benzene, which does not need to surpass an additional energetic or entropic barrier, the number of p-xylene molecules exhibiting the energy required is much lower leading to a drastically lower probability for p-xylene to switch between channels. The difficulty for molecules with an increasing aspect ratio to rotate would also explain the differences in the rates of transport in the straight and the sinusoidal channels. For the latter channel system partial rotations are required at each intersection leading so to a slower process.

It is important to note that the contribution of the slower transport pathway increases markedly with the aspect ratio of the molecule. This is surprising at first sight, because the diffusion constant for the faster pathway varied only in such small quantities (see Table 3.2) that we assumed it to be constant in the final fitting procedure (see Table 3.3 and figure 3.9). On the other hand the diffusion constant for the second pathway decreases with increasing aspect ratio, i.e., from benzene to toluene. This is attributed to the increasing difficulty for reorienting to access the next section of the sinusoidal channel after passing an intersection.

If one accepts for the moment the conclusion that the p-xylene is not able to switch between the straight and the sinusoidal channel, the relative fraction of molecules being transported along the two channels would depend upon the relative ratio of molecules entering the crystal via a straight or a sinusoidal pore. The sorption sites, i.e., the sites at which the molecules are located between jumps, are presumably located at the intersections. This is deduced from the fact that IR spectra indicate that all molecules adsorb in a 1:1 complex at Brønsted acid sites, which are located at the intersections. It also indicates that the residence time at sites in the channels different from OH groups must be short on the timescale of IR vibrations, as otherwise more molecules should be found adsorbed than OH groups interacting with sorbed molecules (Jentys et al., 2006, Mukti et al., 2007). However, the question arises, why the transport of aromatic molecules should increasingly proceed along the slower transport channel, i.e., the sinusoidal channel if the arguments in favor of the attribution are valid.

In order to explore the potential reasons let us discuss the elementary steps of the transport using first p-xylene as example. As outlined above, transport occurs through hopping between sites at intersections and the orientation at the intersection is primarily

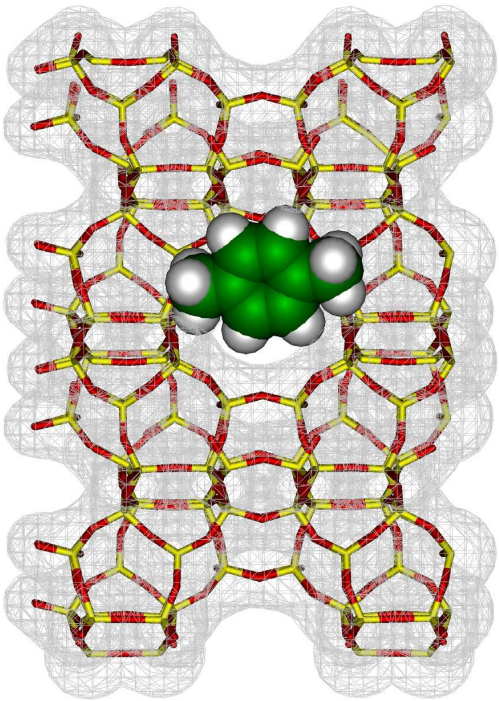

Figure 3.11: Schematic representation of a p-xylene molecule located in the intersection of the MFI framework.

given by the principal orientation of the molecule. The interactions with available Brønsted acid sites only lead to lateral interactions and a very modest reorientation of the sorbed molecule for orientations along the straight and the sinusoidal channels (Jentys et al., 2006, 2007, Mukti et al., 2007). Using canonical ensemble Monte Carlo simulations of p-xylene adsorption Song et al. (Song et al., 2002) showed that p-xylene adsorbs initially statistically at loadings of less than four molecules per unit cell with the alkyl groups along the sinusoidal or the straight channel. A molecule would hop to the next intersection, if it has the sufficient potential energy via thermal equilibration or receives it via an impact from another molecule. While the transport along the straight channel could eventually pass one of the sorption sites, for the sinusoidal channel this is not possible, because of the reorientation the molecules require at each intersection. Thus, one could assume an increasing fraction of p-xylene being adsorbed in an orientation along the sinusoidal channel. This preferred orientation is attributed primarily to kinetic reasons, while the sorbed state should be enthalpically equivalent in both channels. The somewhat higher activation energy of the transport through the sinusoidal channel indicates a lower minimum in the sorbed state, which is, however, more than compensated by a lower preexponential factor (suggesting lower transition entropy).

Therefore, not only the residence time (population) would be higher for the sorption complex oriented towards the sinusoidal channel, also the fraction of unsuccessful collisions with these sorbed molecules should be significantly higher than for molecules oriented along the straight channel. Such unsuccessful collision of molecules from the straight channel and molecules residing in the intersection directed along to the sinusoidal channel should lead to a significant retardation of the rate of transport of a fraction of molecules. Transferred to a simple kinetic model, it would suggest that a fraction of the molecules in the straight channels is transported with the same low rate as the molecules blocking these channels during the reorientation, which would add them to the characteristic wave function attributed to the slower process. We conclude, thus,that the relative high contribution of the slow pathway is related to two effects, a higher relative concentration of the molecules oriented along the sinusoidal channel and the retardation of a fraction of the molecules being transported in the straight channels.

3.5 Conclusions

The presence of two diffusion pathways for aromatic molecules in ZSM5 has been established. This was possible through rigorous exclusion of potential artifacts resulting from the presence of discrete particle size distributions or heat effects. The manifestation of two pathways increases with increasing aspect ratio of the aromatic molecule and

increasing size of the zeolite crystals. It should be emphasized that the importance of these processes may be absent for particles below 100 nm diameter, because under such conditions the relative transport steps at the external surface may begin to dominate.

The presence of two separate diffusion pathways is attributed to the sterically constrained reorientation of toluene and p-xylene. Energetically and entropically unfavorable rotational motions are required to switch from one channel system to the other. The transport in the straight channels is faster for all three molecules and most likely constant for all molecules having the same minimum kinetic diameter. The slower transport through the sinusoidal channels is attributed to the larger fraction of unsuccessful collisions necessary to change the direction at the intersections. This larger number of collisions is also concluded to be associated with a higher concentration of molecules oriented towards the sinusoidal channels. The heat of adsorption for the orientation of the molecules oriented towards the sinusoidal channel may be higher as inferred from the somewhat higher energy of activation for diffusion, while the low pre-exponential factor for the latter process is in line with the expected frequent collisions in order to be able to change directions, when diffusing in the sinusoidal channel. The increasing importance of the diffusion pathway in the sinusoidal channel with increasing aspect ratio of the aromatic molecule is attributed to a retardation of a fraction of molecules being transported in the straight channel.

The results presented establish for the first time unequivocally the role of anisotropic transport in MFI zeolites suggesting that a minimum size of crystals is required for the anisotropy to manifest. Moreover, this further indicates rigorously that molecular traffic control, as envisaged by Derouane and Gabelica (Derouane and Gabelica, 1980), can be experimentally realized for molecules with a diameter of gyration exceeding the space available for a free rotation at the intersections of molecular sieves.

4 Comparison of the Transport of Aromatic Compounds in Small and Large MFI Particles

This chapter was published in the Journal of Physical Chemistry C as research article:

Comparison of the transport of aromatic compounds in small and large MFI particles
Oliver C. Gobin, Stephan J. Reitmeier, Andreas Jentys, and Johannes A. Lercher, J. Phys. Chem. C; **2009**; 113(47), pp 20435-20444

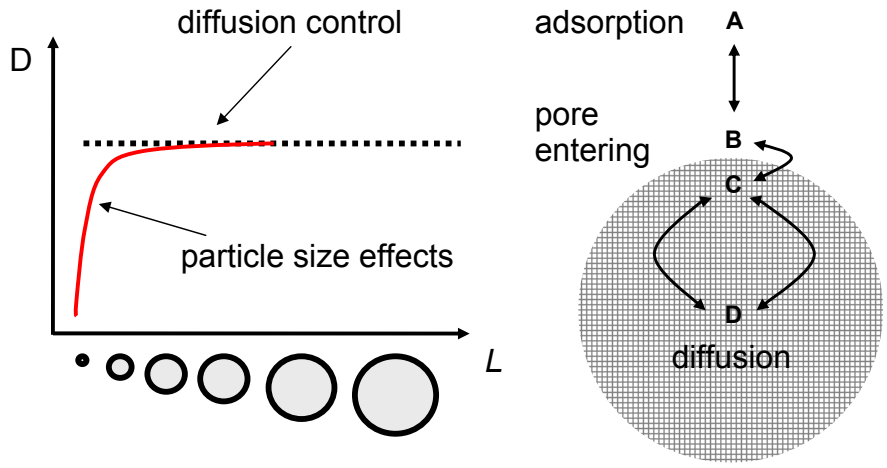

Abstract The diffusion of alkyl-substituted aromatic molecules in two H-ZSM-5 samples consisting of very small (< 100 nm) and large (∼3-4 μm) primary particles was investigated by means of the frequency response method. Analysis of the experimental data in combination with the theoretical modeling of the complete transport network shows that the details of the transport processes and the rate determining step depend on the particle size. With large particles, intracrystalline diffusion was rate determining for the overall diffusion, while for the small particles the diffusion was controlled by surface effects.

4.1 Introduction

The fundamental understanding of the catalytic and sorptive processes in microporous materials is essential for the development and tailoring of next generation materials (Davis, 2002). The overall mass transfer from the gas phase into the porous particle is generally influenced by a series of elementary steps (Jentys et al., 2005, Reitmeier et al., 2008). In particular, these are (i) sorption of the molecule at the outer particle surface, described by the sticking probability, (ii) entering into the pore, and (iii) intracrystalline diffusion processes. The mutual relation of these elementary processes subtly determines the overall transport process and it has been unclear whether or not a single rate determining step exists. Intracrystalline diffusion can be assumed to be rate determining, if the intracrystalline diffusivity D is not a function of the particle size or the characteristic length of diffusion L as the time constant of diffusion (L^2/D) is directly proportional to L^2. Thus, a series of identical materials with different particle sizes allows verifying this situation. If this is not the case, surface adsorption or pore entering might be other potentially rate limiting steps.

Among the zeolites industrially used in large scale, H-ZSM-5 (MFI structure) (Kokotailo et al., 1978, Olson et al., 1981) is a key component in many catalytic and separation processes (Corma, 1995). In the previous chapter (Gobin et al., 2009a) the intracrystalline diffusion of methyl substituted aromatic compounds in ZSM-5 was correlated to its complex crystal structure. The frequency response experiments showed a broadening of the characteristic functions with increasing degree of methyl substitution of the aromatic compounds studied, i.e., benzene, toluene, and p-xylene. This broadening is in part due to a size distribution of the particles in the powder sample and was described accordingly by a diffusion model including a distribution in the particle size. We concluded, however, that two kinetic processes, namely two diffusive flows in the straight and sinusoidal channels ZSM-5 exist leading to anisotropy of the diffusion and to an additional broadening of the frequency responses as a function of the molecule type. The overall transport from the gas phase into the bulk of a ZSM-5 particle can, therefore, be described by a series of consecutive elementary steps including two parallel diffusion processes. In contrast to this highly differentiating behavior of benzene, toluene, and p-xylene in the pores of large particles of MFI materials, small MFI crystals with primary crystal size smaller than 100 nm did not show such a differentiation between the aromatic molecules (Reitmeier et al., 2008).

To resolve this apparent discrepancy, the nature and role of the rate determining steps for the transport as function of the particle size is addressed in this contribution combining extensive characterization of the two materials with diffusion studies using the

frequency response technique. A kinetic model containing all elementary steps involved in transport of the aromatic molecules from the gas phase to the sites inside the pores is established via a detailed analysis of the experimental data.

4.2 Experimental section

4.2.1 Materials

Polycrystalline H-ZSM-5 samples with a Si/Al ratio of 45 and a particle size of < 100 nm and $\sim$3-4 μm were provided by Süd-Chemie AG. For diffusion measurements benzene, toluene, and p-xylene in spectroscopic grade (GC standard, $> 99.96\%$) provided by Sigma-Aldrich were used without further purification. The liquids were treated by several pump-and-freeze cycles to remove gaseous contaminations.

4.2.2 Physicochemical characterization

Nitrogen physisorption isotherms were measured using a PMI automated sorptometer at liquid nitrogen temperature (77 K), after outgassing under vacuum at 473 K for at least 6 h. The apparent surface area was calculated by applying the Brunauer-Emmett-Teller (BET) theory to the adsorption isotherms over a relative pressure range from 0.03 to 0.10. In the typical BET pressure range ($p/p_0 = 0.10$ to 0.30) the BET plot was not linear with a negative intercept, i.e., a negative BET K constant. In addition the Langmuir surface area was obtained by performing a Langmuir plot in the relative pressure range up to 0.10. The pore volumes were evaluated using the α_s comparative plot (Kruk et al., 1998) using nonporous hydroxylated silica (Gregg and W., 1982) as the reference adsorbent. Because of the limitations of the PMI instrument, the isotherms were measured at relative partial pressures higher than 10^{-5} p/p_0

Dynamic light scattering (DLS) measurements were performed on a Malvern Zetasizer Nano ZS. The samples were dispersed in water and kept in an ultrasonic bath prior to the measurements that were repeated at different concentrations several times. Scanning electron microscopy (SEM) images were recorded on a REM JEOL 5900 LV microscope operating at 25 kV with a resolution of 5 nm and a nominal magnification of $3.0 \cdot 10^6$. The morphology of the samples was studied using an ultrahigh resolution cold field emission scanning electron microscope (HR-SEM) operated at 1.5 to 30 kV (Hitachi S-5500). For SEM, the powdered samples were used without any pretreatment or coating. Transmission electron microscopy (TEM) was measured on a JEOL-2011 electron microscope operating

at 200 kV. Prior to the measurements, the powdered samples were suspended in ethanol solution and dried on a copper-carbon-grid. The X-ray powder diffraction patterns were measured on a Philips Xpert Pro XRD instrument operating with the energy of Cu-Kα_1-radiation at 40 kV using a Ni-filter to remove the Cu-Kβ- line. Data points were recorded using a spinner system with a 1/4 inch slit mask between 2θ angles of 5° to 70° with a step size of 0.017° and a scan speed of 115 s per step. The characterization of the acid sites with respect to concentration and distribution was described previously (Zheng, 2002).

4.2.3 Frequency response experiments

30 mg of powder sample were carefully dispersed on several layers of quartz wool at the bottom of a quartz tube in order to avoid artifacts from bed-depth effects. The sample tube was connected to a vacuum system, placed inside a heating oven and pumped to 10^{-7} mbar at room temperature. The samples were heated to 823 K with a ramp of 10 K/min and activated under vacuum below 10^{-7} mbar for one hour to remove adsorbed water. The sorbate gases were added with a partial pressure of 0.3 mbar into the system at temperatures between 333 and 423 K. After the sorption equilibrium was fully established, the volume of the system was modulated periodically by two magnetically driven plates sealed with UHV bellows in the frequency range of 0.001 to 5 Hz. The modulation resulted in a square-wave perturbation of the system volume with an amplitude of 1%. The pressure response of the system to the volume perturbation was recorded with an on- line Baratron pressure transducer (MKS 16A11 TCC). The amplitude and the phase lag of the frequency response were obtained by Fourier transformation of the pressure data. Nonlinear parameter fitting of the theoretical characteristic functions to the experimental frequency response was performed by using the CMA evolution strategy in Matlab (Hansen, 2006). The root mean squared error normalized to the variance of the data (NRMS error) was used as the objective function to be minimized. To ensure that the globally optimal parameter set was found, each optimization run was repeated three times with varying parameter sets of the evolution strategy.

The influence of heat or bed-depth effects was checked by variation of the sample amount and by the way the sample was placed in the sample tube, i.e., with and without dispersing the sample on quartz wool. In all cases the same frequency response was observed and therefore, we can exclude heat or bed-depth effects. In addition, modeling assuming a non-isothermal diffusion (Sun and Bourdin, 1993, Sun et al., 1993) where the time constant of heat transfer is in the same order as for the diffusion process was carried out for all data, and the consistency of the parameters was checked. The resulting

fit was poor in many cases and the obtained time constants were inconsistent, which gives further confirmation that heat effects are not significant in the present frequency response experiment under the conditions studied. An experimental error of less than 5% was obtained for the resulting FR parameters by performing the same experiment several times.

4.2.4 Numerical simulation of the transport network

Numerical simulations were performed in Matlab using the ordinary differential equation solver with 4^{th} order Runge Kutta time discretization or the state space solution in Matlab as implemented in the control system toolbox. The frequency response was obtained in two ways: the first option was to obtain the frequency response by solving the corresponding linear state space model. In the case of the second option the frequency response was by obtained applying small fluctuations, i.e., small changes to the initial conditions, to the set of ordinary differential equations at different frequencies. The initial conditions for the subsequent frequencies were obtained from the corresponding previous frequency. Subsequently, the in- and- out-of-phase characteristic functions were obtained just like the ones during the experimental frequency response measurement. The advantage of this method compared to the linear state space solution in Matlab is the possibility to directly solve the non- linear set of differential equations. The difference in the results, however, is not significant, as implicitly linearization is obtained by only applying small fluctuations. It is important to note that linearization is essential in order to obtain a meaningful frequency response. Non-linear frequency responses are dependent on the size of the fluctuation and may involve higher order frequency components, which are difficult to quantify. Parameter estimation was performed in all cases using the CMA evolution strategy in Matlab (Hansen, 2006).

4.3 Results

4.3.1 Particle size and surface morphology

For diffusion studies the precise investigation of the particle size is crucial as the time constant of diffusion L^2/D is directly proportional to the square of the particle size.

Particle size distributions (PSD), i.e., number densities of particles, with a mean diameter of 0.36 ± 0.17 μm for the sample with the small particles and 4.4 ± 1.5 μm for the sample with the large particles were obtained by DLS. The standard deviations

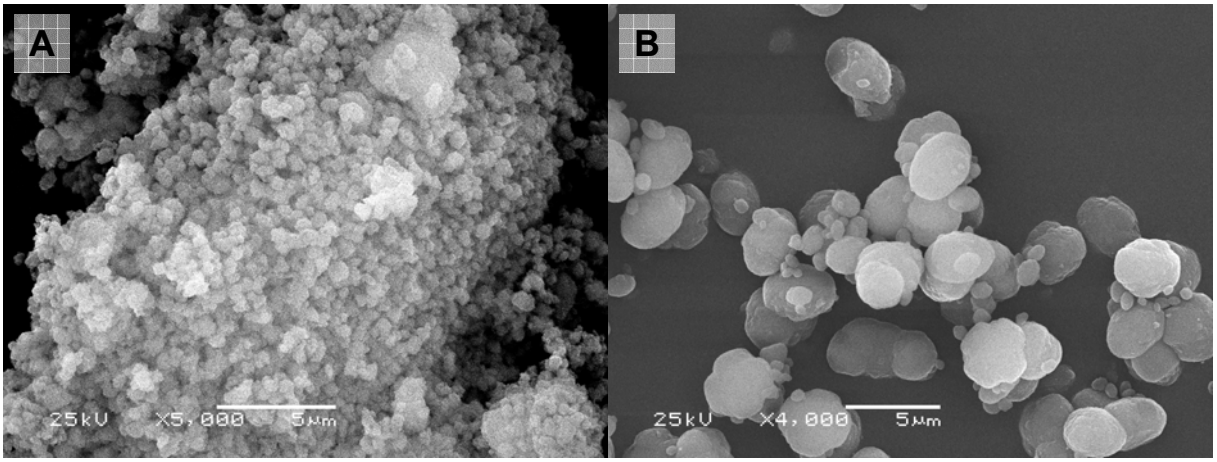

Figure 4.1: Scanning electron micrographs of the sample with (A) small and (B) large particles.

were obtained by a Gaussian fit to the DLS data. These two samples are denoted further on as the small and large crystal sample. In addition, the particle size distribution was estimated by SEM (Figure 4.1) and by TEM (Figure 4.2). An average diameter of 0.4 ± 0.2 μm and 3.9 ± 1.2 μm was obtained for the two samples by SEM, which is in acceptable agreement with the results by DLS. In the case of the small crystal sample, primary crystals of less than 0.1 μm were also observed by TEM (see Figure 4.2). In contrast, large and highly crystalline domains can be distinguished for the large crystal sample. Crystallinity was also checked by XRD (given in the supplementary information) and in both cases well defined reflections corresponding to the MFI structure were observed. By application of the Scherrer equation crystalline domains of about 40-50 nm were obtained for the sample with small particles, which is consistent with the primary crystalline size observed by TEM. For the sample with large particles sharper reflexes were observed and the application of the Scherrer equation indicates crystalline domains of about 200 nm. One should note, that the crystalline size obtained by the Scherrer equation does not necessarily correspond to the particle size, as defects in the crystals lead as well to a broadening of the XRD reflexes.

The nitrogen physisorption isotherms are shown in Figure 4.3. The amount of N_2 adsorbed in the micropores, determined from the adsorption branch up to a relative pressure of $p/p_0 = 0.2$, is identical for both samples, therefore, an identical micropore volume of 0.12 cm^3/g (and a BET surface area of 420 m^2/g) is obtained. Significant differences can only be seen in the meso- and macrostructure at higher pressures. A small amount of mesopores with diameters in the range below 4 nm are present in both samples, in addition, a small fraction of slit shaped mesopores with diameters up to 10^{-15} nm

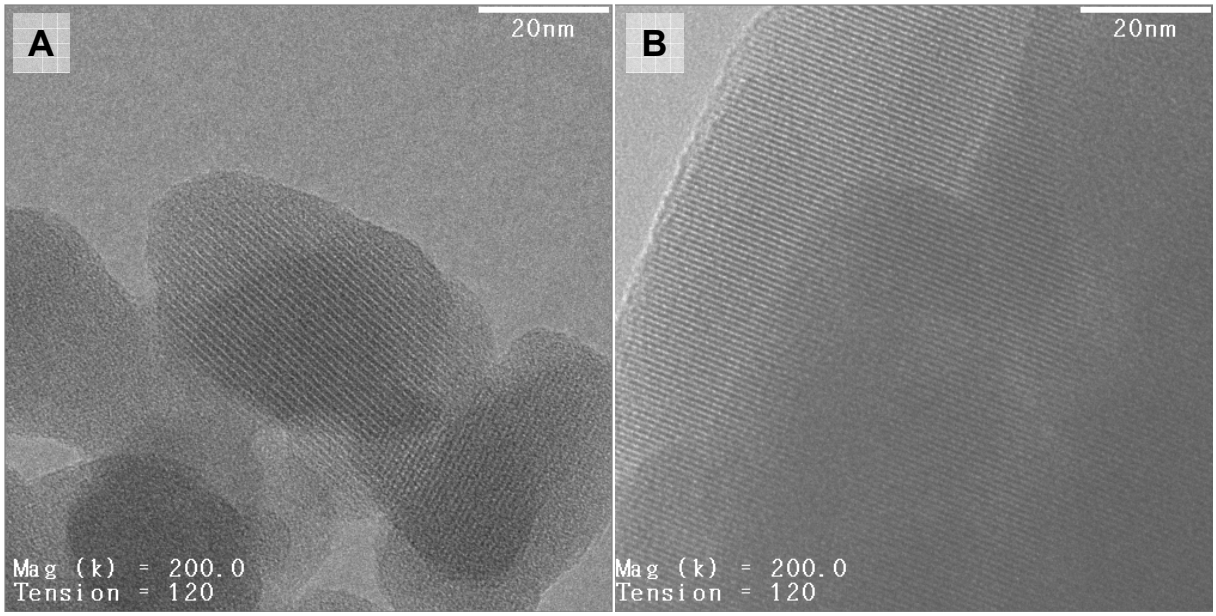

Figure 4.2: Transmission electron micrographs of the sample with (A) small and (B) large particles.

were observed for the sample with large particles. The most important differences were present in the pressure region above $p/p_0 > 0.8$, which is characteristic for macropores larger than 30 nm. These pores can be ascribed to the inter-particle voids formed by agglomeration of the primary particles and are, therefore, predominantly present in the small crystalline sample. This is consistent with the particle size obtained by DLS or SEM (360 ± 170 nm) which is significantly larger than the primary particle size by TEM (< 70 nm). The morphology of the sample, in particular the external surface area, presents the major difference between the two samples. The structural properties of the samples are summarized in Table 4.1.

sample	S_{BET} $\mathrm{m^2g^{-1}}$	V_{mi} $\mathrm{cm^3g^{-1}}$	V_{me} $\mathrm{cm^3g^{-1}}$	V_{ma} $\mathrm{cm^3g^{-1}}$	S_{ext} $\mathrm{m^2g^{-1}}$	V_{tot} $\mathrm{cm^3g^{-1}}$
small	423	0.12	0.04	0.22	65	0.38
large	421	0.12	0.07	0.03	6	0.22

Table 4.1: Structural properties of the ZSM-5 materials. S_{BET} is the surface area according to the BET theory, and S_{ext} the external surface area. V_{mi}, V_{me}, V_{ma}, and V_{tot} are the micropore, mesopore, macropore, and total pore volume, respectively, obtained as described in the experimental section by using the α_{s} comparative plot.

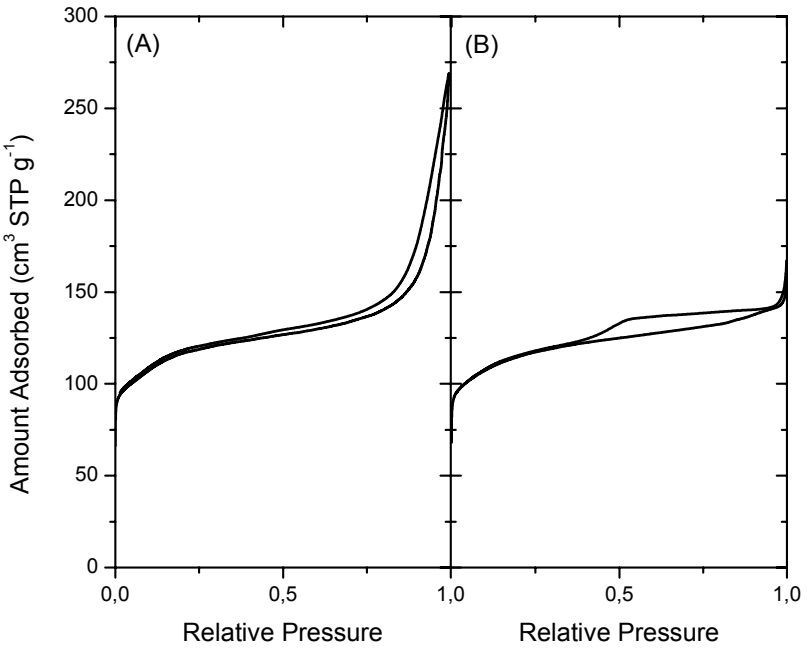

Figure 4.3: Nitrogen physisorption isotherms for the sample with (A) small and (B) large particles.

In order to better understand the surface morphology, HR-SEM measurements were performed and representative images are shown in Figure 4.4. The primary particles of the large sample, shown in Figure 4.4A and 4.4B, appear to be very rough and composed of smaller particles in the order of 50 to 100 nm. The question that arises at this point is if the large particles are agglomerates composed of small particles similar to the particles of the small crystal sample or if the particles are dense with a highly textured surface. In Figure 4.4D a representative cross section of a primary particle of the sample with the large particles is shown, which confirms the well-defined inner core of the primary particles. Other cross sections or broken pieces of the primary particles are shown in the supplementary information. From these images, and also based on the particle size obtained from XRD and on the nitrogen physisorption experiments, it seems highly unlikely that the primary particles of the large sample are agglomerates as in the case of the sample with small particles (Figure 4.4C). Therefore, we assume that the large particles consist of a homogenous core with the size corresponding to the characteristic length of diffusion.

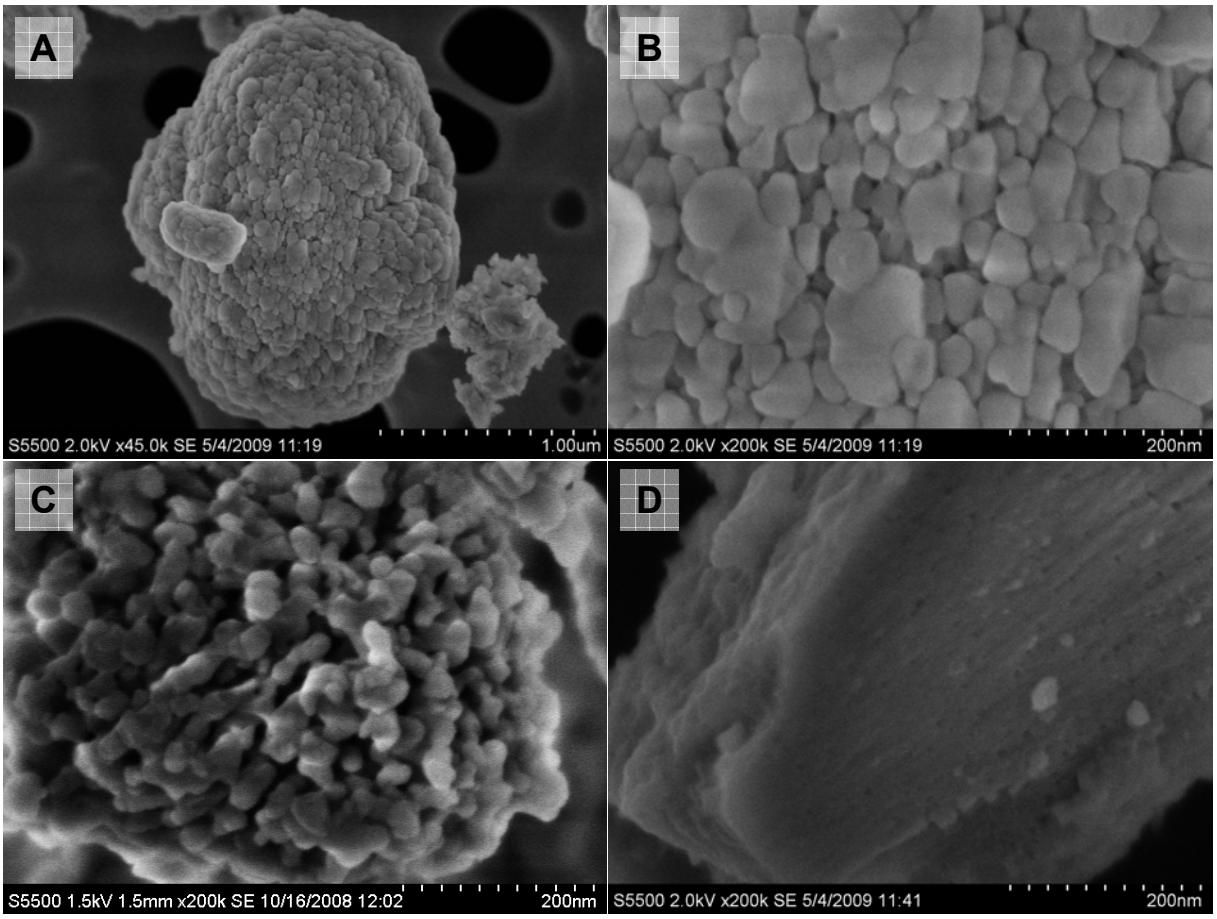

Figure 4.4: High resolution scanning electron micrographs for both samples. (A),(B) show the morphology of the primary particles of the large sample, (C) the morphology and the primary crystalites of the small sample, and (D) a representative cut-through of a primary particle of the large sample.

4.3.2 Transport measurements

The diffusivities of benzene, toluene, and p-xylene at temperatures between 343 and 403 K and the results from the frequency response analysis for the sample with large and small particles are summarized in Table 4.2 and 4.3, respectively. In the case of the sample with the small particles intracrystalline diffusion was assumed to be the rate determining step. For the analysis of the experimental frequency responses a model assuming a particle size distribution, as described in the previous chapter (Gobin et al., 2009a), was used. The out-of-phase frequency responses of benzene, toluene, and p-xylene for both samples at 403 K are compared in Figure 4.5. As already discussed (Gobin et al., 2009a) a distinct broadening of the frequency responses as a function of the degree of methyl substitution of the aromatic compounds was observed for the sample with the large particles, whereas for the sample with the small particles the standard deviation of the particle diameter (i.e. $\sim 0.2\mu$m) was the same for the three molecules studied. In contrast, for the sample with large particles the shape of the FR functions also varied with the type of molecule. Therefore, two diffusion pathways along the straight and the sinusoidal channels for aromatic molecules in ZSM-5 (Gobin et al., 2009a) were proposed, which result from the energetically and entropically unfavorable rotational motions for sterically more demanding molecules required when switching between the two channel systems. In addition, the relative contribution of the slow pathway increases with increasing degree of methyl substitution, i.e., for sterically more demanding molecules. This is related to two effects, a higher relative concentration of the molecules oriented along the sinusoidal channel and the retardation of a fraction of the molecules being transported in the straight channels. These effects are consistent with earlier FR studies and with simulations (Snurr et al., 1993, 1994, Song et al., 2002, Song and Rees, 2000), and with the molecular traffic control model of Derouane and Gabelica (1980) for molecules with a diameter of gyration close or exceeding the space available for a free rotation at the intersections of molecular sieves. The diffusivities of the two transport processes in the sample with large particles are summarized in Table 4.4. They were obtained by applying equations 2.45 and 2.46 with $n = 2$ for a dual diffusion process. The corresponding figures can be found in the previous chapter.

Comparing the time constants of the transport process obtained for the samples with small and large particles, it is remarkable to note that the time constants (L^2/D) are in the same order. This can be directly seen from the position of the maximum in the out-of-phase frequency response in Figure 4.5. As mentioned in the introduction, this cannot be the case, if in both samples the intracrystalline diffusion was observed. Assuming the intracrystalline diffusion to be the rate determining step, the diffusivities as given in Table 4.2 and 4.3 would be obtained. However, the calculated apparent

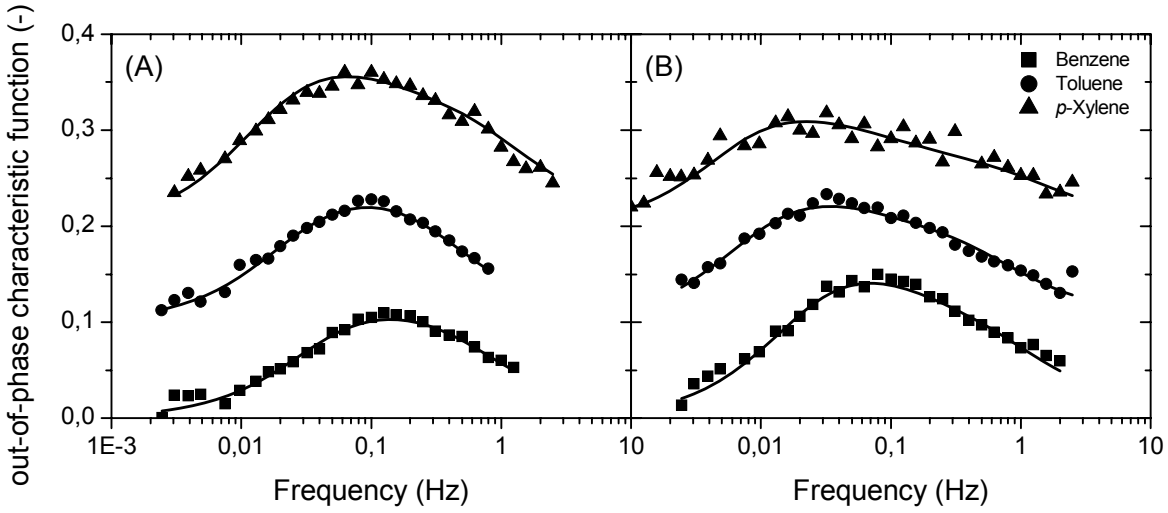

Figure 4.5: Out-of-phase frequency responses of benzene, toluene, and p- xylene at 403 K for the sample with (A) small and (B) large particles. The fits were obtained using a single diffusion model with a Gaussian particle size distribution and taking into consideration a surface resistance. The curves are shifted by 0, 0.1, and 0.2, respectively.

		T	L^2/D	D_{app}	K	NRMS-Error	E_A
		°C	s	x 10^{15} m^2/s			kJ/mol
benzene		343	32.5	3.96	0.73	0.26	
L =	3.59 x 10^{-07} m	373	17.6	7.34	0.46	0.19	23
σ =	2.12 x 10^{-07} m	403	10.0	12.9	0.29	0.16	
toluene		343	58.6	2.20	0.89	0.11	
L =	3.59 x 10^{-07} m	373	27.7	4.66	0.53	0.17	29
σ =	2.17 x 10^{-07} m	403	13.5	9.56	0.34	0.16	
p-xylene		343	132.9	0.97	0.77	0.30	
L =	3.59 x 10^{-07} m	373	52.0	2.48	0.57	0.32	35
σ =	2.32 x 10^{-07} m	403	21.4	6.02	0.39	0.19	

Table 4.2: Transport data and fitting parameters obtained for a theoretical model assuming one apparent diffusion process D_{app} with a Gaussian particle distribution as additional fitting parameter for the sample with small crystals.

		T °C	L^2/D s	D_{app} x 10^{15} m^2/s	K	NRMS-Error	E_A kJ/mol
benzene		343	62.4	3.09	0.84	0.28	
$L =$	4.39 x 10^{-06} m	373	36.5	5.28	0.57	0.21	21
$\sigma =$	2.22 x 10^{-06} m	403	20.3	9.50	0.46	0.17	
toluene		343	142.8	1.35	1.00	0.25	
$L =$	4.39 x 10^{-06} m	373	68.6	2.81	0.65	0.32	28
$\sigma =$	3.18 x 10^{-06} m	403	33.1	5.83	0.42	0.17	
p-xylene		343	169.1	1.14	0.91	0.26	
$L =$	4.39 x 10^{-06} m	373	78.3	2.46	0.78	0.30	29
$\sigma =$	4.28 x 10^{-06} m	403	38.2	5.04	0.41	0.35	

Table 4.3: Diffusivity data and fitting parameters obtained for a theoretical model assuming one processes with a Gaussian particle distribution as additional fitting parameter for the sample with large crystals.

diffusivity of the sample with small particles is two orders of magnitude lower compared to the sample with the large particles. In addition, the apparent activation energies of the transport process are higher for the sample with small particles (see Table 4.3 and Figure 4.6). This situation in combination with the fact that broadening of the out-of-phase characteristic functions as a function of the molecule type was not observed for the sample with small particles is clear evidence that different rate limiting steps in the transport processes were observed depending on the particle size.

4.4 Discussion

In order to understand the complex transport processes in both samples, a transport network involving all relevant elementary steps was developed, as shown schematically in Figure 4.7. It is composed of surface adsorption, pore entering and intracrystalline diffusion inside the particle. Each transport step was assumed to depend on the relative occupancy of the corresponding neighbor site, thus, involving non-linear relationships between each state. The following non-linear set of ordinary differential equations (summarized as equation 4.1) was developed based on Figure 4.7 and can be used to describe the transport process in both samples.

	T °C	D_1 10^{13} m^2/s	D_2 10^{13} m^2/s	D_{mean} 10^{13} m^2/s	K_1	K_2	NRMS-Error	E_{A1} kJ/mol	E_{A2} kJ/mol	E_{Amean} kJ/mol
benzene	343	4.95	0.51	3.30	0.56	0.33	0.27			
	373	7.98	1.02	5.82	0.40	0.18	0.20	17	26	20
	403	11.2	2.08	9.02	0.35	0.11	0.16			
toluene	343	4.01	0.40	1.88	0.41	0.59	0.23			
	373	7.52	0.98	3.12	0.17	0.35	0.17	19	27	23
	403	11.0	1.49	7.74	0.23	0.12	0.20			
p-xylene	343	3.90	0.17	1.16	0.25	0.69	0.24			
	373	5.65	0.44	2.26	0.28	0.52	0.28	20	27	25
	403	10.9	0.93	3.85	0.12	0.29	0.33			

Table 4.4: Diffusivity data and additional fitting parameters obtained for a theoretical model assuming two processes with a constant Gaussian particle distribution of 1.49 x 10^{-6} m for the sample with large crystals.

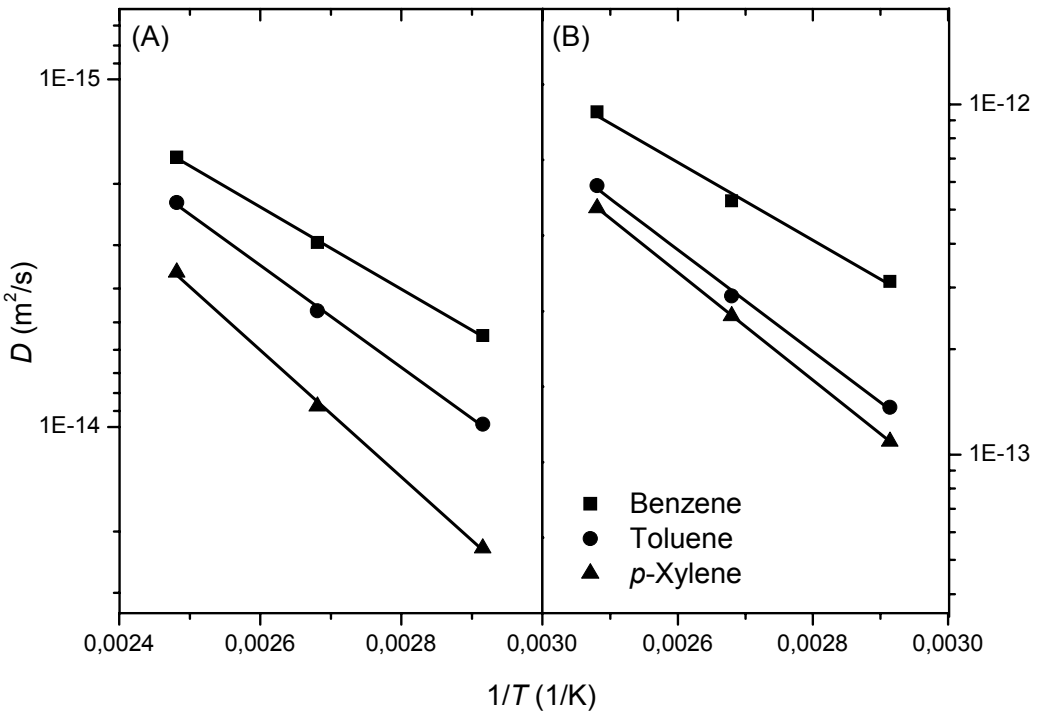

Figure 4.6: Arrhenius plots of the apparent diffusivities for the sample with (A) small and (B) large particles. It is assumed, that in both cases the intracrystalline diffusion is the rate determining step.

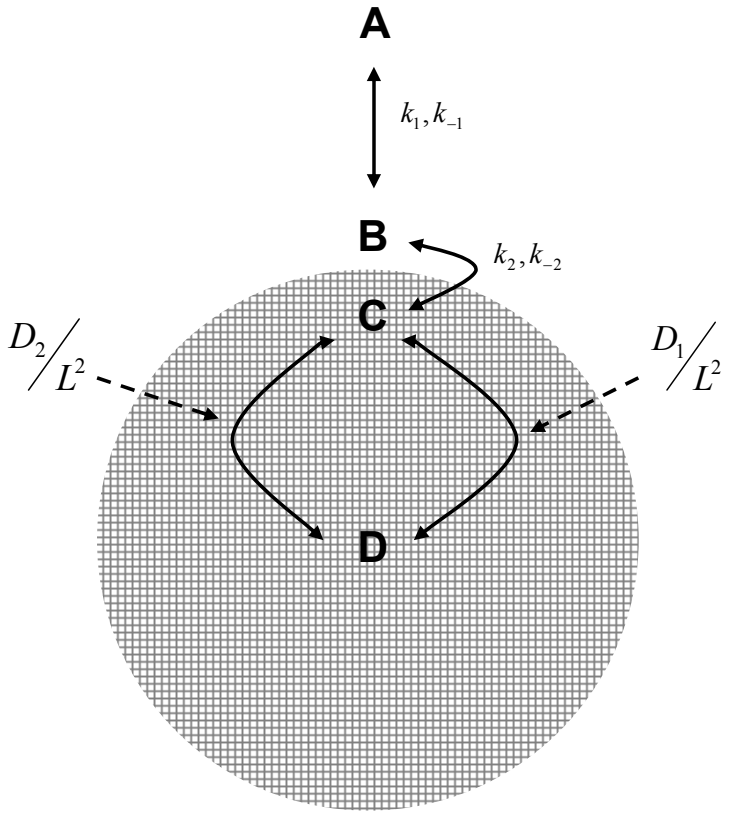

Figure 4.7: Schematic representation of the complete transport process from the gas phase (A), onto the particle surface (B), into the ZSM-5 pore sytem (C), and inside the particle (D). The two diffusion pathways through the straight and sinusoidial channels are represented by D_1 and D_2, the rate constants for each elementary step by k.

$$
\begin{aligned}
\frac{1}{RT}\cdot\frac{\mathrm{d}p}{\mathrm{d}t} &= k_{-1}c_B - k_1\frac{p}{RT}\cdot\frac{\delta_{B,\max}}{\delta_{\max}}\left(1-\theta_B\right)\\
\delta_{\max}\cdot\frac{\mathrm{d}c_B}{\mathrm{d}t} &= k_1\frac{p}{RT}\cdot\delta_B\left(1-\theta_B\right) - k_{-1}c_B\cdot\delta_{\max} +\\
&\quad k_{-2}c_C\cdot\delta_B\left(1-\theta_B\right) - k_2c_B\cdot\delta_C\left(1-\theta_C\right)\\
\delta_{\max}\cdot\frac{\mathrm{d}c_C}{\mathrm{d}t} &= k_2c_B\cdot\delta_C\left(1-\theta_C\right) - k_{-2}c_C\cdot\delta_B\left(1-\theta_B\right) +\\
&\quad \frac{D_1}{L^2}c_{D1}\cdot\left(1-\theta_C\right) - \frac{D_1}{L^2}c_C\cdot\delta_{D1}\left(1-\theta_{D1}\right) +\\
&\quad \frac{D_2}{L^2}c_{D2}\cdot\delta_C\left(1-\theta_C\right) - \frac{D_2}{L^2}c_C\cdot\delta_{D2}\left(1-\theta_{D2}\right)\\
\delta_{\max}\cdot\frac{\mathrm{d}c_{D1}}{\mathrm{d}t} &= \frac{D_1}{L^2}c_C\cdot\delta_{D1}\left(1-\theta_{D1}\right) - \frac{D_1}{L^2}c_{D1}\cdot\delta_C\left(1-\theta_C\right)\\
\delta_{\max}\cdot\frac{\mathrm{d}c_{D2}}{\mathrm{d}t} &= \frac{D_2}{L^2}c_C\cdot\delta_{D2}\left(1-\theta_{D2}\right) - \frac{D_2}{L^2}c_{D2}\cdot\delta_C\left(1-\theta_C\right)
\end{aligned}
\tag{4.1}
$$

where p and c_i correspond to the pressure and concentration of the corresponding state i, $k_{1/-1}$ to the rate constants for adsorption, $k_{2/-2}$ to the rate constants for pore entering and D_n/L^2 to the intracrystalline diffusion processes.[pic]is the total number of sites and θ_i the fractional coverage of the corresponding site i. $\delta_{\max}$ is the total number of all sites (B,C, D_1 and D_2). For small fluctuations, i.e., after linearization, higher order terms are small and can be neglected. State B represents the concentration on the particle surface, state C the concentration in the ZSM-5 structure just below the surface, and state D the concentration at the center of the particle. The most important simplification of the transport network is the modeling of the intracrystalline diffusion assuming a first-order kinetic process. Analytical solutions of the 2$^{\text{nd}}$ Ficks law are generally series of exponential functions, however, by neglecting all higher order terms, an exponential decay is obtained, which can be modeled by a first order kinetic process.

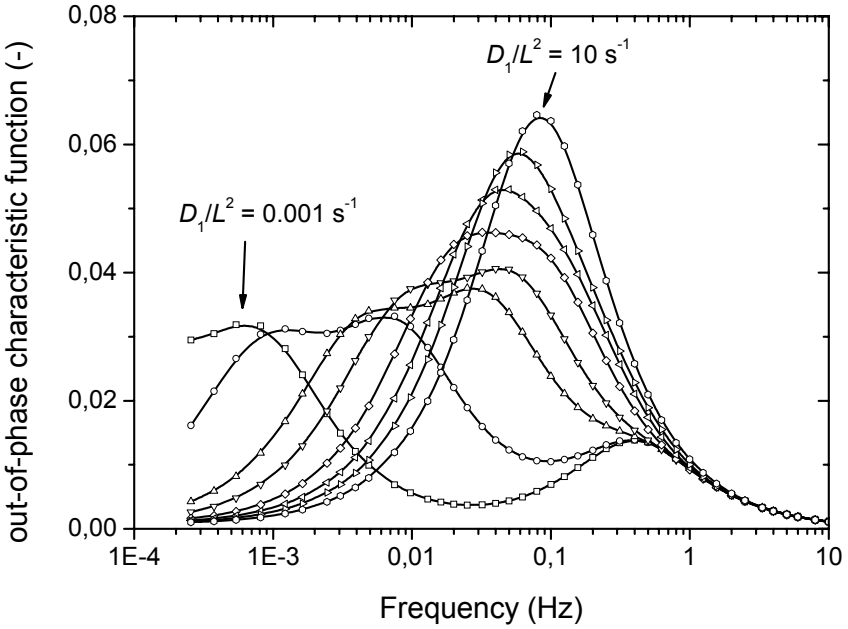

Figure 4.8: Simulated out-of-phase characteristic functions of a system, where the time constants for the diffusion processes were varied over a range from $D_1/L^2 = 0.001$ s^{-1} to 10 s^{-1}. D_1 corresponds to the fast diffusion process. The second diffusion process D_2 was set to $0.1 \cdot D_1$.The adsorption and pore entering kinetics, as well as the number of sites, were kept constant ($k_1 = 10$ s^{-1}, $k_{-1} = 10000$ s^{-1}, $k_2 = k_{-2} = 0.5$ s^{-1}).

Figure 4.8 shows a series of computed out-of-phase characteristic functions for a system where the time constants for the diffusion processes were varied over four orders of magnitude, thus, simulating the behavior of a series of samples with varying characteristic

diffusion length. The adsorption and pore entering kinetics, as well as the number of sites, were kept constant ($k_1 = 10$ s^{-1}, $k - 1 = 10000$ s^{-1}, $k_2 = k_{-2} = 0.5$ s^{-1}) and set to values which are close to the one we expect from the experiments conducted. The initial adsorption was considered to be fast compared to the pore entering. Two diffusive flows with diffusivities differing by one magnitude are assumed to be present, as suggested by the experimental results obtained for the diffusion of p-xylene in the sample with large particles. One can clearly see in Figure 4.8 that two distinct peaks at low frequencies are present, if the rate of diffusion is small compared to the one of pore entering. In addition, a distinct peak related to the pore entering kinetics is visible at high frequencies. By gradually decreasing the particle size the rate of diffusion of both diffusive flows increases and leads to a shift of the peaks in the frequency response to higher frequencies and to a narrowing of the out-of-phase function of the frequency response. A further decrease of the particle size yields in a faster rate of diffusion compared to the pore entering and consequently only one kinetic process is visible. Unexpectedly, this process lies at lower frequencies compared to the rate of pore entering. This series shows clearly the relation between the internal and the external transport kinetics. In the case of the sample with small particles, the rate of diffusion is much higher than the one of pore entering, which becomes the rate limiting step and consequently only one kinetic process can be observed in the frequency response. The shift of the process to slightly lower frequencies compared to the mere pore entering is attributed the presence of the forward and backward steps (microscopic reversibility). If the rate of diffusion is fast compared to the pore entering, the concentration at state C (Figure 4.7) is low which leads to a decreased backward rate. In contrast, if the rate of diffusion is low, the concentration at state C is high leading to a higher backward rate and to a shift of the pore entering peak in the frequency response to higher frequencies. This shows the complexity of such a system, in which the rates of a single elementary step are directly related to the kinetics of the preceding or succeeding steps. The model, however, explains why only one peak in the frequency response can be seen in the case of a very fast diffusion process due to small particles, although two intracrystalline diffusive flows which differ by one magnitude are still present.

Slow diffusion processes or, correspondingly, large particles, lead to a lower diffusion rate compared to the pore entering process. Therefore, the diffusion process becomes the rate limiting step and is apparent in the frequency responses. This situation is perfectly in line with the results observed for the substituted aromatic compounds in the two samples and is also consistent with previous findings (Mirth et al., 1993, Muller et al., 1994). It also explains why the observed activation energy of the process is higher for the small sample, for which the observed kinetic process is dominated by adsorption and pore entering and not intracrystalline diffusion.

Recent studies (Tzoulaki et al., 2008a,b, 2009) have shown that surface barriers are observable on many microporous materials including ZSM-5. Molecules from the gas phase have to overcome these barriers on the crystal boundary in order to enter the pore system. In the case of very small particles, the transport is governed by surface effects, including surface barriers. It is interesting to note that the activation energy of the transport process obtained for the sample with small particles is higher than the one of the sample with large particles, where the transport is governed by intracrystalline diffusion. In our recent findings on surface effects (Jentys et al., 2007, Reitmeier et al., 2008, 2009a), we attributed surface barriers to entropic effects, such as the reorientation of the molecules required to surpass the surface boundary layer. Higher activation energy for the sample with small particles, however, would suggest an enthalpic nature of these barriers, which is not in agreement with our previous results. We therefore suggest, that the higher activation energy is related to a higher sorption enthalpy on the surface due to a larger concentration of surface defect sites in the case of the sample with small particles.

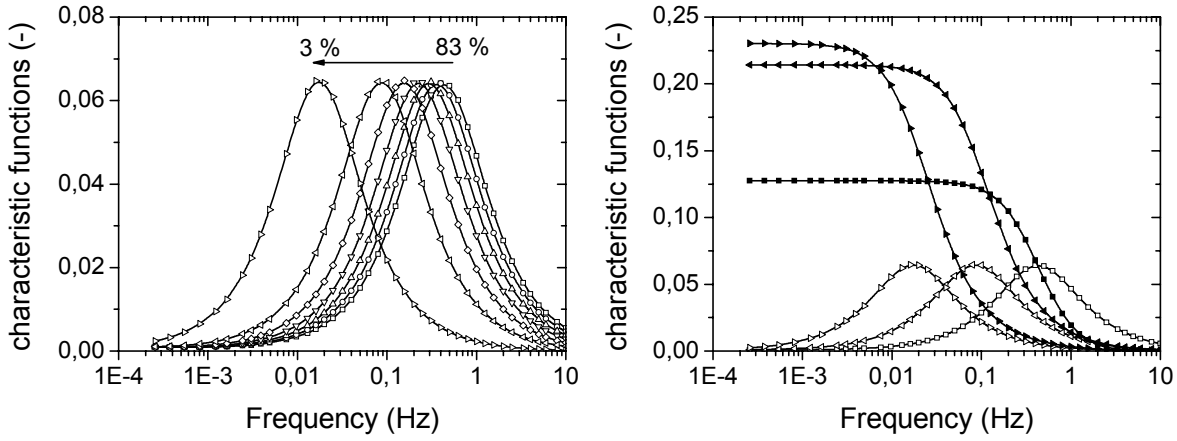

Figure 4.9: Simulated characteristic functions of a system, where the time constants for the diffusion processes were fast, i.e., $D_1/L^2 = 100$ s^{-1}, compared to the adsorption and pore entering kinetics ($k_2 = k_{-2} = 0.5$ s^{-1}). Only the number of pore entering sites was varied from 3% to 83% relative to the total number of site.

In order to better understand the transport in the samples investigated in this work, in addition to the variation of the rate constants, the weighting of the relative contributions of each state by varying the number of sites δ has to be also considered. A faster internal diffusion rate compared to the pore entering step leads to a convolution of the transport mechanisms resulting in a single peak in the frequency response. This peak slightly shifts

to lower frequencies compared to the peak resulting from the pore entering as shown in Figure 4.8. As udiscussed in the previous paragraph the shift is due to a decreased rate at state C. A series of frequency responses computed by changing the relative contribution of the diffusion and of the pore entering process assuming a fast internal diffusion while maintaining the rate constants of each step constant is shown in Figure 4.9. In all cases only the pore entering step is visible in the frequency response. In the case of a more pronounced pore entering process, the in- and out-of-phase functions are overlapping as typically observed for a mere adsorptive system (Yasuda, 1994a). This effect can also be reproduced by changing the relative contribution of intracrystalline diffusion and pore entering.

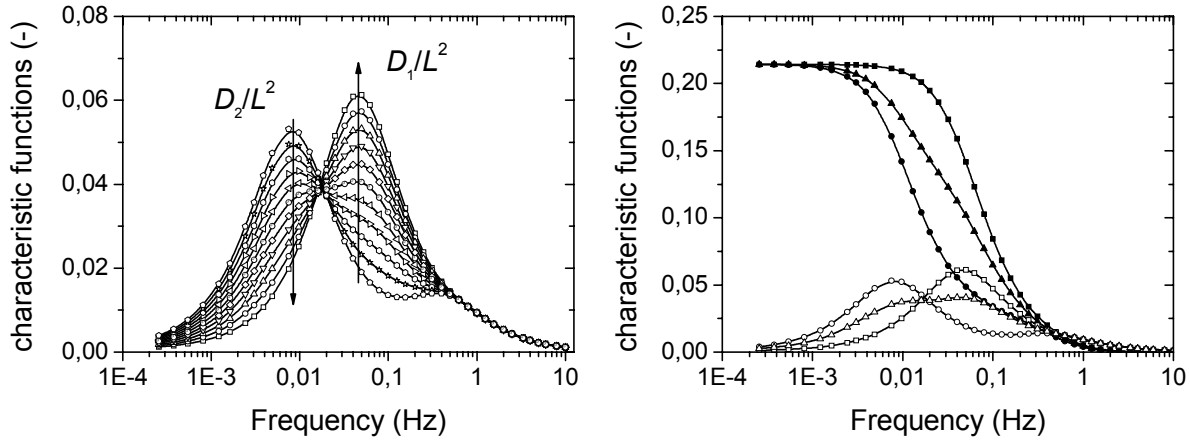

Figure 4.10: Simulated characteristic functions of a system, where the contribution for the diffusion processes was varied from 0% to 100% relative to each other ($D_1/L^2 = 0.1$ s^{-}1 and $D_1/L^2 = 0.01$ s^{-1}). The adsorption and pore entering kinetics, as well as the number of sites, were kept constant ($k_1 = 10$ s^{-1}, $k_{-1} = 10000$ s^{-1}, $k_2 = k_{-2} = 0.5$ s^{-1}).

A second effect can be explained by variation of the relative contribution of the kinetic processes. In all cases depicted in Figure 4.8, the peak at higher frequencies resulting from the faster diffusion process was more pronounced compared to the diffusion peak at lower frequencies. In contrast, however, the experimental frequency responses obtained for the sample with large particles always show a more pronounced peak at lower frequencies as can be seen in Figure 4.5. As discussed by in the previous chaper (Gobin et al., 2009a) and confirmed by the results of this work, the fraction of the molecules in the straight channels is transported with the same low rate as the molecules blocking these channels during the reorientation, which leads to a more pronounced low frequency process. In the proposed model in this work, this can be described by

changing the relative contribution of each diffusion pathway, as shown in Figure 4.10, where a series of out-of-phase frequency responses was calculated by only varying the relative number of sites of the two diffusive flows. In this case the number of sites can be regarded as weighting factors related to the number of molecules involved in the transport at the corresponding rate and a clear transition between the diffusive flows can be observed. Similar to the previous case where the rates were varied (see Figure 4.8), the process related to pore entering (i.e., the peak at higher frequencies in the frequency response) becomes apparent, when the slow diffusion process dominates, due to the stronger separation of the kinetic processes in the frequency response.

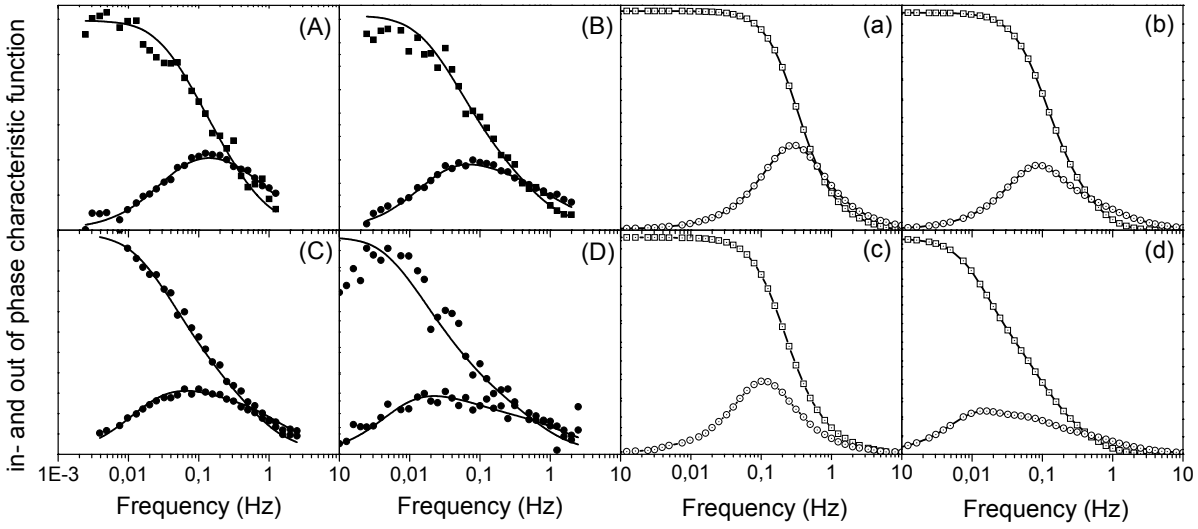

Figure 4.11: Comparison of experimental (A/B/C/D) and simulated (a/b/c/d) characteristic functions of benzene (A/B, a/b) and p-xylene (C/D, c/d) in the sample with small (A/C, a/c) and large (B/D, b/d) particles. The parameters for the simulations were chosen according to the experimental data obtained in several previous studies. Only the contribution of pore entering and diffusion processes was varied relative to each other. Particle size effects were not considered.

To validate the observed results and the conclusions made herein, the model was directly used to describe the experimental frequency responses. One should note that a direct fitting of the experimental data is not reasonable, as the number of parameters is too high and different parameter sets may produce similar results. We, therefore, followed a different strategy in order to verify the results using the theoretical model. The experimental parameters obtained using various experiments (Jentys et al., 2007, Reitmeier et al., 2008, 2009a) were directly taken and incorporated into the model. In

addition, reasonable choices for inaccessible parameters and some simplifications were made. All the steps were assumed to be in equilibrium except the initial adsorption at the surface. The adsorption was considered to be fast with a considerably higher rate for the desorption, which is in line with the low sticking probability previously observed (Reitmeier et al., 2008). The rate constants of the pore entering were obtained from infrared (IR) pressure step experiments as previously reported. Using variations in coverage determined by IR spectroscopy it is possible to directly investigate surface effects and to differentiate between the various sites present in the acidic H-ZSM-5 samples. The intracrystalline diffusion constants were obtained from the frequency response experiments on the sample with large particles. The time constants of diffusion for both samples were calculated assuming that the intracrystalline diffusion is the same for both samples by using the corresponding characteristic length. These values are consistent with the one obtained using the diffusivities reported in the literature (Ruthven, 2007a) and are summarized in Table 4.5. The density of sites or the contribution of the kinetic process were used as normalized scaling parameters and only varied relative to each other. They can be regarded as fitting parameters in order to describe the previously discussed effects. The results of the simulations are directly compared to the experimental results in Figure 4.12 and in Figure 4.11 in the supplementary information. Figure 4.11 shows the same results as Figure 4.12 , however, without incorporation of particle size effects.

adsorbate	sample	pore entering		diffusion 1		diffusion 2	
		k	contribution	D_1/L^2	contribution	D_2/L^2	contribution
benzene	small	0.5 s^{-1}	67%	100 s^{-1}	33%	-	-
p-xylene	small	0.5 s^{-1}	44%	100 s^{-1}	22%	10 s^{-1}	33%
benzene	large	0.5 s^{-1}	44%	0.05 s^{-1}	56%	-	-
p-xylene	large	0.5 s^{-1}	33%	0.05 s^{-1}	22%	0.005 s^{-1}	44%

Table 4.5: Simulation parameters used in order to reproduce the experimental frequency responses shown in Figure 4.5 and 4.12.

The main features of the experimental results can be reproduced very well using this kinetic model. Only one peak is present for the sample with small particles, which slightly shifts as a function of the molecule type, exactly as observed experimentally. For benzene in the sample with large particles also only one peak can be seen, however, located at lower frequencies as the peak for the small sample. For p-xylene two diffusion peaks become apparent and lead to a stronger broadening of the frequency response compared to benzene. The results are in all cases similar to the frequency response experimentally observed. This is remarkable, as the only parameters which were adjusted were the relative contribution of the transport processes and the total number of sites.

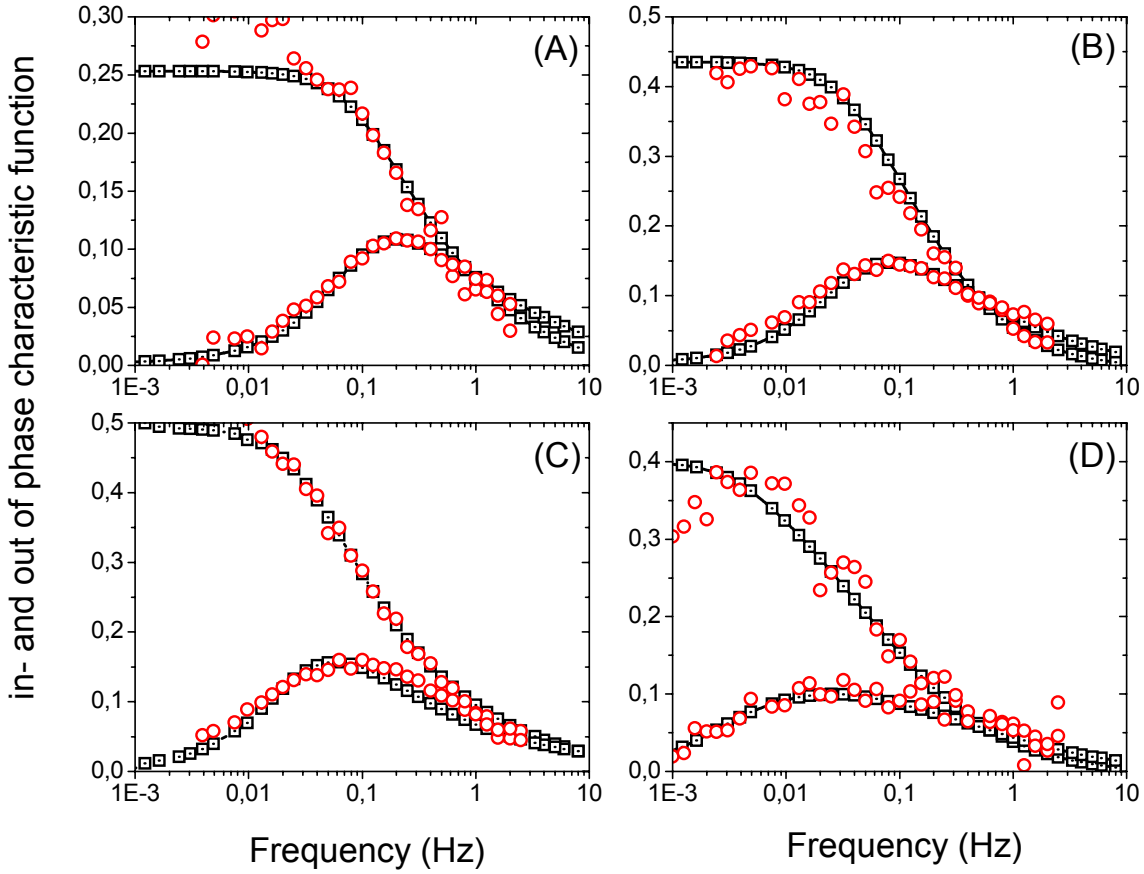

Figure 4.12: Comparison of experimental (circle) and simulated (square) characteristic functions of benzene (A/B) and p-xylene (C/D) in the sample with small (A/C) and large (B/D) particles. The parameters for the simulations were chosen according to the experimental data obtained in several previous studies, including the variance of the particle size distribution. Only the contribution of pore entering and diffusion processes was varied relative to each other.

All other parameters, including the particle size distribution, were directly obtained from the experimental results. It can be seen, that also the overlapping of the in- and out-of-phase function can be reproduced. Only for the sample with small particles, the overlapping is not as pronounced as in the case of the experimental data.

Overlapping of the characteristic functions can be attributed to two effects, which cannot be differentiated as both lead to exactly identical characteristic functions. First, an overlapping is observed in the case of an adsorptive system, where the contribution of external surface adsorption is high or in the same order as the intracrystalline diffusion (Yasuda, 1991). Second, an overlapping is also observed in the case of macropore diffusion (Jordi and Do, 1993, Sun et al., 1994). In the case of the small sample, a significant contribution of macropore diffusion is present. As macropore diffusion was not implemented in the theoretical model, the overlapping cannot be described perfectly. In contrast, in the case of the sample with large particles, a lower amount of macropores are present as can be seen in the isotherms in Figure 4.3, and the theoretical model is able to describe precisely the observed effects.

Based on the results and the discussions above, a major general conclusion with respect to the measurement of diffusivities by macroscopic methods can be made. If the time constant of the diffusion process is small, i.e., a fast diffusion or small particles, a macroscopic method will not be able to measure the mere diffusion, but a complex interplay between surface adsorption, pore entering, and intracrystalline diffusion. This situation still holds, even if the accuracy and time resolution of the apparatus is very high, as for instance in the case of a hypothetical frequency response apparatus able to perform high quality pressure perturbations at high frequencies up to 100 Hz. We conclude, therefore, that independently of the macroscopic method, intracrystalline diffusion can be only measured, if the time constants are distinctly larger than the one of the surface processes. For zeolitic systems, we have shown that the time constants of surface processes are in the order of 1s, therefore, it is suggested, that the diffusion time constant L^2/D must be at least one magnitude larger, i.e. > 10 s. This is for instance the case for benzene diffusion in ZSM-5 ($D \approx 10^{-13}$ m^2/s) composed of particles of at least 1-2 μm, or for o-xylene in ZSM-5 ($D \approx 10^{-16}$ - 10^{-17} m^2/s) (Klemm and Emig, 1997) for particles in the nanometer range (10 - 100 nm). A faster diffusion process or smaller particles will lead to a complex and practically inseparable convolution of multiple kinetic processes masking the intracrystalline diffusion.

4.5 Conclusions

A new model based on frequency response kinetics, able to describe the complex relation between surface transport and diffusion, is proposed. In ZSM-5 samples composed of primary particles below 100 nm the transport of benzene, toluene, and p-xylene is governed by the rate of surface adsorption and pore entering. Diffusion processes cannot be investigated under these conditions, as the rate of diffusion is considerably higher than the one of the surface processes. Although being fast, the diffusion processes still influences the overall transport in a subtle way. In contrast, in particles larger than 1 μm, the diffusion process becomes apparent. Two diffusion pathways for aromatic molecules in ZSM-5 are present, leading to diffusion anisotropy in ZSM-5 for sterically more demanding aromatic molecules.

For any system composed of nano-sized particles, we suggest that a complete description of the transport processes requires knowledge of the intrinsic transport properties, i.e., elementary steps and rate constants, in order to understand the complex interplay of these transport mechanisms. Any interpretation of the results obtained from a macroscopic method for measuring intracrystalline diffusion without knowledge of these intrinsic properties will suffer from the limitation that the rates of the intracrystalline diffusion processes have to be considerably lower than the ones of the surface adsorption and pore entering. If this is not the case, the intracrystalline diffusion will be masked and only separable from the other kinetic processes if the intrinsic properties are known.

5 Role of the surface modification on the transport of hexane isomers in ZSM5

This chapter was published in the Journal of Physical Chemistry C as research article:

Role of the surface modification on the transport of hexane isomers in ZSM5
Oliver C. Gobin, Stephan J. Reitmeier, Andreas Jentys, and Johannes A. Lercher J. Phys. Chem. C; **2011**; 115(4), pp 1171–1179

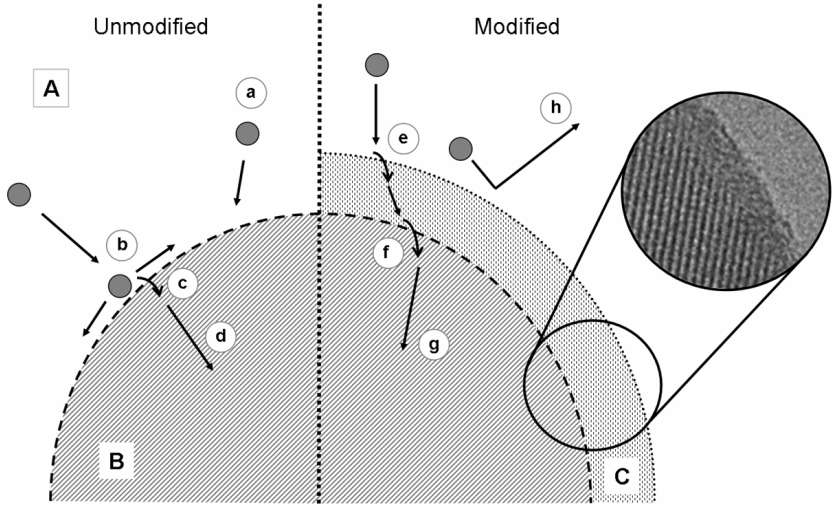

Abstract The role of the surface modification on the transport properties of nano-sized ZSM-5 particles was investigated by the analysis of the sorption kinetics of hexane isomers. The rate of diffusion is enhanced by this modification, if the initial adsorption is the limiting step, i.e., for n- hexane, 2-methylpentane, 3-methylpentane. If the intracrystalline transport is the rate determining step, i.e., for 2,2-dimethylbutane, the surface modification leads to a significantly decreased sorption rate. This reduction in the transport rate is caused by a lower pre-exponential factor, i.e., it is entropically induced. Due to the surface modification a certain fraction of the pores is completely blocked for the sterically demanding molecules reducing the probability of entering the pores. The results show that surface modification of microporous materials allows selectively enhancing or decreasing the transport rate of defined systems.

5.1 Introduction

Recent studies have shown that surface effects may strongly influence molecular transport and shape selectivity of zeolites and in particular of ZSM-5 (Kortunov et al., 2004, Reitmeier et al., 2009b,c, Wloch, 2003, Zhang et al., 2009, Zheng et al., 2006). The nature of these surface modifications and their impact on the transport rates is, however, only partially understood. The sorption rate is enhanced for samples composed of very small particles, which are surface modified with tetraethyl orthosilicate (TEOS) using chemical liquid deposition (Reitmeier et al., 2009a,b). In contrast, physical vapor deposition of differently sized silica sources showed a negative effect on the sorption rates (Chmelik et al., 2007). The properties of the surface can only be characterized by macroscopic transport experiments, if the rate determining steps are either the surface adsorption or the pore entering step. In other words, the overall rate constant of intracrystalline diffusion has to be fast compared to the overall rate constant of the surface kinetics. As reported in a recent contribution by Gobin et al. (2009b), the analysis of systems, in which all involved steps are kinetically significant is possible, however, it requires additional information on transport properties.

In several recent publications (Reitmeier et al., 2009a,b, Zheng et al., 2003) we reported and discussed the effects of surface modification of ZSM-5 by chemical liquid deposition of TEOS on the transport properties of aromatic molecules, i.e., benzene, toluene, and p-xylene. For benzene and toluene, the sticking coefficient increased after applying a surface layer leading to faster transport to acid sites in the pores in the modified materials (Reitmeier et al., 2009b). This specificity of the impact of the surface modification depends on the structure of the surface that influences the rate of the initial sorption of the molecules from the gas phase, i.e., the first elementary steps in the kinetic network of diffusion (Gobin et al., 2009a, Reitmeier et al., 2009a,b) and the reorientation of the molecules in the surface layer. Both effects enhance the sticking probability due to the larger pore openings compared to the parent ZSM-5 pores. The facile reorientation of molecules in the surface layer and enhances their access into the zeolite pore system (Reitmeier et al., 2009a). A kinetic transport model composed of gas phase adsorption, pore entering, and intracrystalline diffusion allowed us to verify the presence and to quantify the rates of these steps (Reitmeier et al., 2009b).

In this study, the transport of hexane isomers is investigated with these parent and surface modified materials. Compared to the diffusion of benzene, toluene, and p-xylene two major differences are evident, i.e., hexane isomers are more flexible and their critical molecule diameter changes significantly from n-hexane to 2,2-dimethylbutane. Relevant molecular dimensions of the molecules such as the length of the molecules and their

critical diameter are given in Table 5.1 (Cavalcante and Ruthven, 1995). The critical diameter is defined here as the diameter of the smallest cylinder that circumscribes the molecule considering the van der Waals radii. It can be seen that this diameter increases from 0.43 nm for n-hexane to 0.63 nm for 2,2- dimethylbutane resulting in a dramatic change of the transport properties. Note that the critical diameter is independent of the length of the main carbon chain and depends only on the methyl substitution of the main carbon chain.

Compound	Abbrev.	crit. diameter nm	length nm
n-hexane	nH	0.43	1.07
2-methylpentane	2MP	0.54	0.94
3-methylpentane	3MP	0.54	0.94
2,3-dimethylbutane	23DMB	0.58	0.81
2,2-dimethylbutane	22DMB	0.63	0.81

Table 5.1: Dimensions of the hexane isomers used as sorbates (in nm) in this study. The critical diameter is the diameter of the smallest cylinder that circumscribes the molecules. All values were estimated based on bond angles and bond length using van der Waals radii for the outer atoms (Cavalcante and Ruthven, 1995).

ZSM-5 is composed of two interconnected pore systems, one with straight channels with a diameter of about 0.53 x 0.56 nm, and the other with slightly smaller sinusoidal channels with a diameter of 0.51 x 0.55 nm. Though the pore size of ZSM-5 is smaller than the critical diameter of 2,2-dimethylbutane it diffuses and adsorbs in ZSM-5. This can be explained by the fact that both diameters are calculated from van der Waals radii and are, hence, not rigid parameters. Additionally, the zeolite lattice is flexible and can be distorted in the process of sorbing molecules (van Koningsveld and Jansen, 1996) or expanded as a function of the temperature (Webster et al., 1999).

Herein, we are reporting the transport properties of iso-hexane molecules in nano-sized H-ZSM-5 particles with and without modification of the outer surface. The results are compared to the recently reported transport measurements of aromatic compounds in the same type of materials (Gobin et al., 2009a,b, Reitmeier et al., 2009a,b).

5.2 Experimental section

5.2.1 Materials

As parent material, a commercial, polycrystalline H-ZSM-5 sample with a Si/Al ratio of 45 was used. The particle size and morphology was investigated using several techniques. Dynamic light scattering (DLS) and scanning electron microscopy (SEM) showed that the sample was composed of larger agglomerates with a mean diameter of 0.36 ± 0.17 μm. The primary particle size, i.e., the size relevant for the interpretation of transport experiments, was found to be below 100 nm by transmission electron microscopy (TEM) and X-ray diffraction (XRD) (Gobin et al., 2009b). Post-synthetic modification of the external zeolite surface was performed by chemical liquid deposition (CVD) of tetraethyl orthosilicate (TEOS) according to Zheng et al. (Zheng, 2002, Zheng et al., 2003). Typically, 1.5 ml TEOS (4 wt% SiO_2) and 10 g zeolite were dispersed in 164.50 g hexane and heated at 353 K under reflux for one hour. Afterwards hexane was evaporated in a rotary evaporator. The resulting powder sample was dried before calcination at 823 K for at least 8 h. This procedure was repeated three times, resulting in an amorphous silica layer of about 3 nm. For transport measurement n-hexane (nH), 2-methylpentane (2MP), 3-methylpentane (3MP), 2,3-dimethylbutane (23DMB), and 2,2-dimethylbutane (22DMB) in spectroscopic grade (GC standard, $> 99.96\%$) provided by Sigma- Aldrich were used without further purification. The liquids were treated by several pump-and-freeze cycles to remove gaseous contaminations.

5.2.2 Physicochemical characterization

Nitrogen physisorption isotherms were measured using a PMI automated sorptometer at liquid nitrogen temperature (77 K), after outgassing under vacuum at 473 K for at least 6 h. The apparent surface area was calculated by applying the Brunauer-Emmett-Teller (BET) theory to the adsorption isotherms over a relative pressure range from 0.03 to 0.10 p/p_0. In the typical BET pressure range ($p/p_0 = 0.10$ to 0.30) the BET plot was not linear with a negative intercept, i.e., a negative BET K constant. In addition the Langmuir surface area was obtained by performing a Langmuir plot in the relative pressure range up to 0.10 p/p_0. The pore volumes were evaluated using the α_s comparative plot (Kruk et al., 1998) using nonporous hydroxylated silica (Gregg and W., 1982) as the reference adsorbent. Because of the limitations of the PMI instrument, the isotherms were measured at relative partial pressures higher than 10^{-5} p/p_0. DLS measurements were performed on a Malvern Zetasizer Nano ZS. The sample was dispersed in water and kept in an ultrasonic bath prior to the measurements that were repeated at different

concentrations several times. SEM images were recorded on a REM JEOL 5900 LV microscope operating at 25 kV with a resolution of 5 nm and a nominal magnification of 3.0 x 10^6. The morphology of the samples was studied using an ultrahigh resolution cold field emission scanning electron microscope (HR-SEM) operated at 1.5 to 30 kV (Hitachi S-5500). For SEM, the powdered samples were used without any pretreatment or coating. TEM was measured on a JEOL-2011 electron microscope operating at 200 kV. Prior to the measurements, the powdered samples were suspended in ethanol solution and dried on a copper-carbon-grid. The X-ray powder diffraction patterns were measured on a Philips Xpert Pro XRD instrument operating with the energy of Cu-Kα_1-radiation at 40 kV using a Ni-filter to remove the Cu-Kβ-line. Data points were recorded using a spinner system with a quarter inch slit mask between 2θ angles of 5° to 70° with a step size of 0.017° and a scan speed of 115 s per step. The characterization of the acid sites with respect to concentration and distribution was described previously (Zheng, 2002).

5.2.3 Gravimetric sorption and uptake experiments

The gravimetric sorption capacities of the molecules as well as the slow transport kinetics of 2,2-dimethylbutane were measured on a Setaram TG-DSC 111 thermoanalyzer. In order to avoid bed depth and thermal effects a low amount of powder sample (10 mg) was dispersed in quartz wool. Activation was performed at 823 K for 1 h with a heating rate of 10 K min^{-1} under vacuum ($p < 10^{-7}$ mbar). The weight increase and the thermal flux were measured during equilibration with the sorbate at 343, 373, and 403 K using small pressure steps up to 13 mbar. The heats of adsorption were directly obtained by integration of the observed heat signal, whereas the entropies of adsorption were calculated using the Gibbs-Helmholtz equation. Uptake curves were normalized and analyzed using a 1D diffusion model (Crank, 1979).

5.2.4 Infrared spectoscopy

Experimental Setup: A high vacuum system equipped with a system for periodic volume modulation was combined with a Bruker IFS 66 v/S infrared spectrometer using a vacuum cell for infrared spectroscopic measurements in transmission mode. The sorbate partial pressures were measured by a MKS Baratron (MKS 616A11) pressure transducer. For fast time-resolved rapid scan experiments periodic volume modulations with an amplitude of $\delta V = \pm 5\%$ were generated by a pair of flexible UHV bellows and synchronized with the recording of the infrared spectra (Jentys et al., 2005). These small variations of the system volume are necessary to exclude adiabatic effects due to local exothermicity

otherwise interfering with the transport kinetics of the sorbate. A complete description of the full instrumental setup and the measurement principle of the fast-time resolved infrared spectroscopy is published elsewhere in detail (Jentys et al., 2005, Zheng et al., 2004).

Sample preparation and activation: The powdered zeolite samples were pressed into self-supporting wafers ($\backsim$20 mg cm^{-2}) and subsequently inserted into a gold ring sample holder inside a vacuum IR cell. Preliminary evacuation below 10^{-5} mbar at 403 K for several hours was followed by activation under vacuum below 10^{-7} mbar at 823 K for 1 h using an incremental heating rate of 5 K min^{-1} before sorbate gas was added. The IR spectra were recorded with a resolution of 4.0 cm^{-1} for sorption and 8.0 cm^{-1} for transport experiments at a temperature of 343 K.

Fast time-resolved infrared spectroscopy: Sorbate gas was added with partial pressure of 0.10 mbar at 343 K. A series of 100 IR spectra with time resolution of 600 ms was recorded during 400 modulation cycles. The resulting data was processed according to Jentys et al. (Jentys et al., 2005, 2006). In order to verify that system non-idealities do not influence the measurements, so called blank or empty measurements were performed in addition. It was found, that that the influence of the system non-idealities on the measurement is only minor and does not influence the quantitative results.

In order to directly compare the surface coverage of the adsorbed species all spectra were baseline corrected and normalized to the integral of the overtone lattice vibration bands between 2105 and 1740 cm^{-1} of the IR spectra of the activated H-ZSM-5 samples. Quantification of the sorbate concentration changes was obtained by integration of the characteristic C-H and C-C stretching vibrational bands (1406 - 1506 cm^{-1} for C-C and 2740 - 3020 cm^{-1} for C-H) assuming a constant molar extinction coefficient obtained by gravimetric equilibrium measurements. Herein, for the surface modified sample, the data was corrected by the mass of the non-adsorbing surface overlayer (12 wt% SiO_2). The concentration change after reaching equilibrium ΔC_{eq} and the characteristic time constant of the sorption τ was obtained according to Jentys et al. (Jentys et al., 2005, 2006) by fitting the concentration profiles with first-order exponential functions as given for the adsorption and for the desorption in equation 5.1 and 5.2:

$$\Delta c(t) = \Delta c_{\mathrm{eq}} \cdot \left[1 - \exp\left(\frac{-t}{\tau}\right)\right] \;\forall\, 0 < t \leq t_{\mathrm{p}}/2 \tag{5.1}$$

$$\Delta c(t) = \Delta c_{\mathrm{eq}} \cdot \exp\left(-\frac{t - t_{\mathrm{p}}/2}{\tau}\right) \;\forall\, t_{\mathrm{p}}/2 < t < t_{\mathrm{p}} \tag{5.2}$$

Herein t_{p} denotes the time period of the modulation cycle. The initial sorption rate is given by equation 5.3:

$$r = \frac{\mathrm{d}\Delta C(t)}{\mathrm{d}t} = \frac{\Delta c_{\mathrm{eq}}}{\tau} \tag{5.3}$$

5.2.5 Calculation of sticking probabilities on zeolites

The sticking probabilities α of the sorbate molecules were calculated according to Equation 5.4, which was derived in detail in our previous studies (Reitmeier et al., 2009c).

$$\alpha = \frac{4 \cdot r \cdot R \cdot T}{\overline{u} \cdot N_{\mathrm{A}} \cdot (p_2 - p_1)} \tag{5.4}$$

Herein $\overline{u}$ denotes the mean gas velocity of the sorbate molecule in the gas phase, p_i the pressure limits within the volume modulation cycle during in-situ infrared spectroscopy, r the initial rate defined in equation 5.3, N_{A} the Avogadros number, T the temperature and R the general gas constant.

5.2.6 Theoretical calculations

Density functional theory (DFT) calculations of the sorbate molecules were performed in Gaussian 03 using the B3LYP32 exchange-correlation functional together with the 6-31G basis set. Additional parameters were Opt=CalcFC and Pop=Minimal.

5.3 Results

The parent sample is a polycrystalline ZSM-5 material with primary crystallites with diameters of below 100 nm as obtained by analysis of the XRD pattern using the Scherer equation (for XRD patterns see Figure S1 in the supplementary material). In addition, TEM indicates the presence of particles with high crystallinity of 50 to 80 nm size, which is consistent with the results by XRD. Using DLS and SEM it can be seen, that the primary particles form agglomerates with an average diameter of $0.36 \pm 0.17\mu$m. The inter-particle void formed by the agglomeration of the primary particles is in the range of 30 to 50 nm, as obtained by analysis of the nitrogen physisorption isotherm (given in Figure S2 in the supplementary information). Pore volumes obtained from nitrogen physisorption are compiled in Table 5.2. After correction of the deposited SiO_2 amount, the micropore volume is identical for both parent and surface modified sample. A slight increase in the mesopore volume with diameters of about 1.5 nm can be observed, which is related to the sponge like pore structure of the deposited surface overlayer (Reitmeier et al., 2009a). The modification can be seen by TEM in Figure 5.1 as an amorphous surface layer with an average thickness of 3.0 nm.

The results from gravimetric equilibrium adsorption experiments are given in Table 5.3. After correction of the mass of the deposited surface layer, the results are identical for

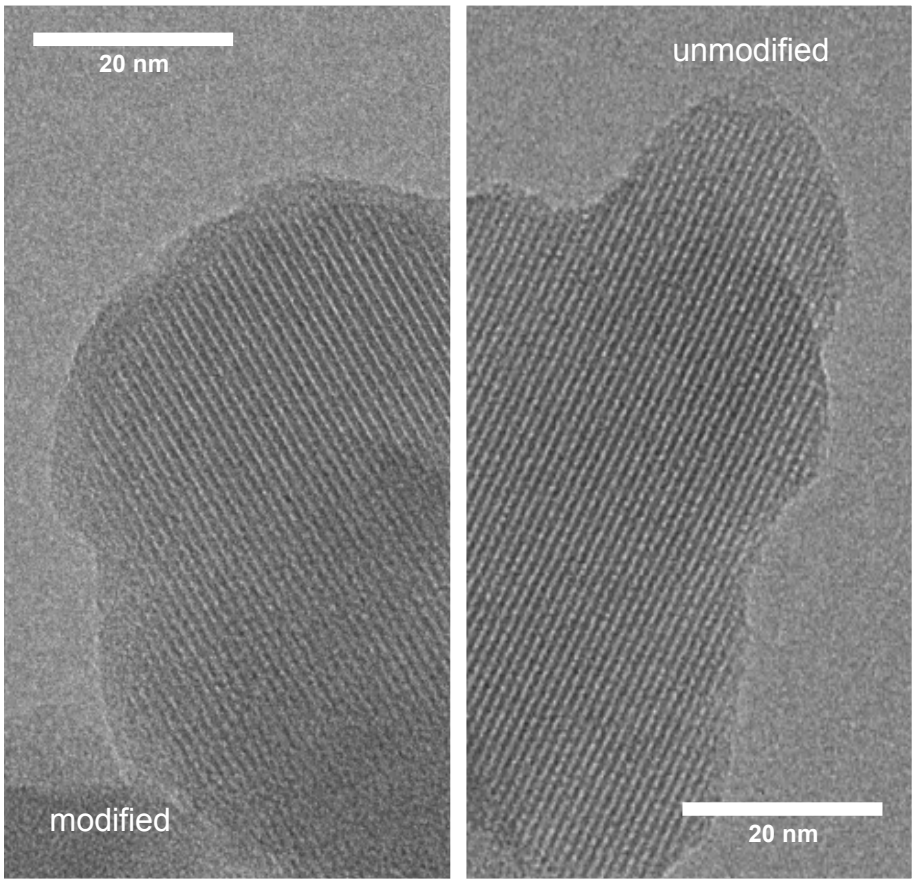

Figure 5.1: Transmission electron micrographs of (right) the unmodified ZSM-5 and (left) three-fold modified ZSM-5 sample. The surface layer consisting of amorphous SiO_2 covering the crystalline core is clearly seen (left).

Sample	S_{BET} m^2/g	V_{mi} cm^3/g	V_{me} cm^3/g	V_{ma} cm^3/g	V_{tot} cm^3/g
Parent MFI	423	0.121	0.0173	0.225	0.364
Modified MFI	383	0.113	0.0308	0.178	0.322
Modified MFI x 112%	429	0.127	0.0345	0.200	0.361

Table 5.2: Structural parameters obtained from the analysis of the N2- physisorption isotherm. The BET surface area S_{BET}, micropore volume V_{mi}, mesopore volume V_{me}, macropore or interparticle volume V_{ma}, and the total pore volume V_{tot} are given for the parent and the modified sample. In addition, the values of the modified material after correction of the deposited SiO_2 amount are also included.

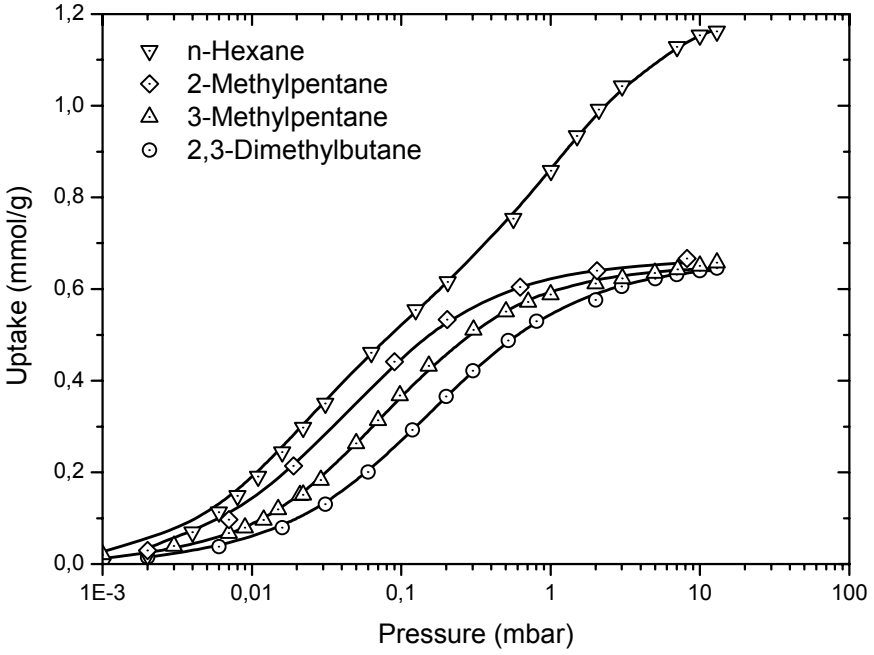

Figure 5.2: Gravimetric adsorption isotherms of n-hexane, 2-methylpentane, 3-methylpentane, and 2,3-dimethylbutane at 343 K.

both samples, as the pores of the surface modification are not adsorbing at these pressures. The surface modification, therefore, only affects the transient and not the equilibrium of the sorption properties. The corresponding isotherms at 343 K are shown in Figure 5.2. Additional isotherms are included in the supporting information. The sorption properties of the parent and modified sample were also checked by analysis of the IR adsorption isotherms. Also in this case, after correction of the mass of the non-adsorbing overlayer pores, the same amount was adsorbed and, therefore, we conclude, that the zeolite pore system has not been compromised by the surface treatment.

The gravimetric isotherms were measured up to 13 mbar and, thus, a complete filling of the pore system was not achieved for all isomers. Under these condition, hexane shows a two step adsorption isotherm that can be modeled by assuming a dual Langmuir model (Cavalcante and Ruthven, 1995). The isotherms of the single branched isomers 2MP and 3MP as well as of the di-branched isomers can be modeled by a single Langmuir model. The maximum possible loading for the iso-hexanes as theoretically calculated by **?** is 8 (nH), 7 (2MP), 6.3 (3MP), and 4 (23DMB / 22DMB) molecules per unit cell. Only for 23DMB and 22DMB the maximal loading was achieved at a pressure of 13 mbar (at 343 K). In the case of the single branched molecules (2MP and 3MP) only the first Langmuir component is visible up to 13 mbar, the second part only becomes apparent at higher

Sorbate	ΔH kJ/mol	ΔS J/mol	θ_{max1} / θ_{max2} mmol/g	K(343 K) 10^3 (-)	K(373 K) 10^3 (-)	K(403 K) 10^3 (-)
nH	-72	-121	0.65 / 0.57	49.1	5.82	1.24
2MP	-70	-121	0.65	24.3	3.97	0.70
3MP	-65	-111	0.64	14.2	2.51	0.54
23DMB	-64	-113	0.64	7.13	1.22	0.29
22DMB	-63	-106	0.65	11.9	2.42	0.54

Table 5.3: Summary of the gravimetric equilibrium data for the sorbates. The equilibrium constant K of the first Langmuir component and the maximum loadings θ_{max1} and θ_{max2} were obtained by fitting the isotherms with a Langmuir model for the branched isomers and a dual Langmuir model for n-hexane.

pressures, which is consistent with results reported previously (Cavalcante and Ruthven, 1995, Sommer et al., 2003). In the case of n-hexane, a higher loading with a partial filling of the second type of sorption sites is already observed at pressures below 13 mbar. The Langmuir fitting parameters, i.e., maximal loading and equilibrium constants, are summarized in Table 5.3 together with the enthalpies and entropies of adsorption. As expected, the heats of adsorption show a slight trend depending on the length of the main carbon chain. The heat of adsorption of 22DMB is the lowest and close to the one of n-pentane. The other isomers show values in between. This is attributed to the fact, that the heat of adsorption is directly related to the strength of dispersive interactions of the molecule with the zeolite host. The molecules orientate along the walls in order to maximize the van-der- Waals interactions. n-Hexane has the longest main carbon chain, and, thus, the interaction with the pore walls is the highest. The other isotherms require statistically less space on the surface, however, in contrast more space in the pore void. Thus, the van-der-Waals interactions are lower, resulting in lower enthalpies of adsorption. In addition, more space is required in the pores, thus, at a given pressure, the loading of the iso- hexanes is lower than the one of n-hexane. 22DMB can be seen as the extreme case, for which the maximum loading is significantly lower, as the adsorption only takes place in the ZSM-5 intersections and a filling of the ZSM-5 channels is energetically not possible under the tested conditions (Cavalcante and Ruthven, 1995, Sommer et al., 2003).

An inverse trend can be observed for the entropies of adsorption. n-Hexane loses a larger fraction of entropy during adsorption than 22DMB. This larger loss of entropy is associated with the stronger bonding that reduces the residual degrees of freedom. Such compensation between the enthalpy and entropy of adsorption has also been reported

for the adsorption of alkanes in other zeolites (Bond et al., 2000, Denayer et al., 1998, Eder and Lercher, 1997, Eder et al., 1997). From IR isotherms it can be seen, that the concentration adsorbed on the surface silanol groups is very low compared to the total number of molecules adsorbed. From both, the IR and gravimetric isotherms at a pressure of 0.1 mbar, a strong preferential adsorption on the bridging silanol groups was observed being accompanied by non-specific adsorption in the ZSM-5 pores.

Contrary to the equilibrium experiments, for which effects of the surface modification were not observed, transient transport experiments showed marked differences between the parent and the surface modified sample. The time constants from the rapid scan experiments obtained by integration of the specific SiOHAl IR bands and of the C-C or C-H IR bands were in all cases the same within the experimental error range. However, in order to investigate the transport involving all molecules adsorbed in the ZSM-5 lattice, the results for the C-C or C-H IR bands are reported herein. For both samples, the uptake of all molecules except 22DMB was very fast with time constants below 10 s. It is not reasonable to analyze such fast processes by gravimetric analysis as the relaxation time of the gravimetric system itself is in the range of 1 to 5 s. Therefore, the kinetics was followed using time resolved infrared spectroscopy. The results for both parent and modified sample are visualized in Figure 5.3 together with the quantitative evaluation and the equilibrium loadings at 0.1 mbar in Table 5.4.

Sample	Sorbate	τ	θ_{eq}	ΔC_{eq}	Δr
		s	molec./UC	μmol/g	μmol/(g · s)
parent	nH	2.32	2.99	4.91	2.11
	2MP	4.89	2.60	5.16	1.05
	3MP	5.22	2.14	5.92	1.14
	23DMB	6.49	1.53	5.88	0.91
modified	nH	1.42	2.99	4.91	3.45
	2MP	1.41	2.60	5.16	3.65
	3MP	2.31	2.14	5.92	2.56
	23DMB	7.26	1.53	5.88	0.81

Table 5.4: Time constants τ, loading θ_{eq}, equilibrium concentration changes ΔC_{eq}, and rates Δr of the transport obtained from the IR concentration profiles.

For the parent sample the time constants or the sorption rates were found to vary in the order nH > 2MP ≈ 3MP > 23DMB, whereas for the surface modified sample the order changes: 2MP ≈ nH > 3MP > 23DMB. The rates of the molecules nH, 2MP, and 3MP were significantly enhanced by the surface modification. Interestingly, 23DMB

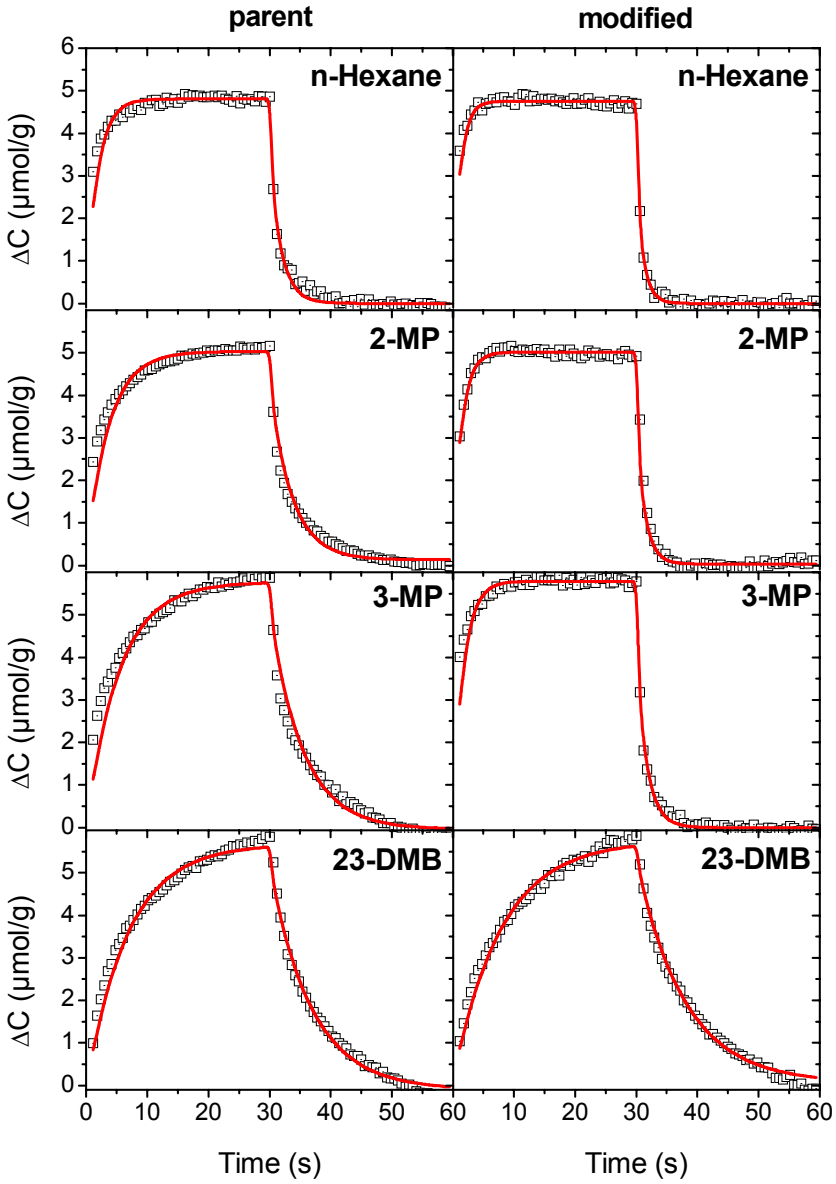

Figure 5.3: Changes in coverage of the C-C IR band at 343 K, for the parent (left) and modified (right) sample. A volume perturbation of (5% around the equilibrium pressure of 0.10 mbar was applied.

showed a slight decrease in the rate. Similar sorption effects were already observed for aromatic compounds as discussed by Reitmeier et al. in recent publications (Reitmeier et al., 2009a,b).

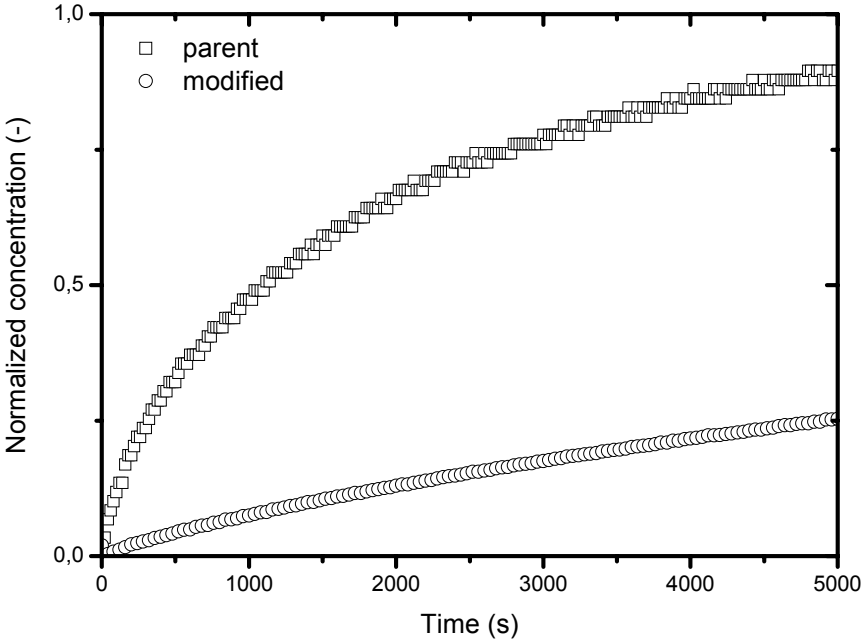

Figure 5.4: Gravimetric uptake of 2,2-dimethylbutane at 343 K for the parent and modified ZSM-5 sample.

Figure 5.4 shows the influence of the surface modification on the gravimetric uptake of 22DMB at 343 K. As the uptake was much slower compared to the other isomers, the kinetics was measured by gravimetry. A strong decrease in the uptake rate was observed upon surface modification. Assuming an intracrystalline controlled diffusion process as the dominant transport mechanism for 22DMB, diffusivities as summarized in Table 5.5 are obtained. For the parent sample, a diffusivity of 10^{-19} to 10^{-20} m^2/s was observed, which is consistent with the literature value of 22DMB diffusion in ZSM-5 (Boulicaut et al., 1998). For the surface modified sample, a decrease in diffusivity of one order of magnitude was observed. Interestingly, the activation energies obtained by analyzing the temperature dependence of the uptake (see Figure 5.5) were found to remain nearly constant as can be seen in Table 5.5. The pre-exponential factor of the Arrhenius term shows, however, a pronounced change. This can easily be seen in Figure 5.5 as the slope of the Arrhenius plots remains nearly constant, whereas the intercept changes by about half an order of magnitude (see Table 5.5).

	T K	τ s	D 10^{-19} m^2/s	E_A kJ/mol	k 10^{-4} s
parent	343	34.1	2.94		
	373	8.36	12.0	58	52.5
	403	1.62	61.6		
modified	343	325	0.31		
	373	79.4	1.26	62	1.14
	403	12.3	8.14		

Table 5.5: Time constants τ, diffusivities D, energies of activation E_A, and pre-exponential factor k of the Arrhenius term obtained from the gravimetric uptake of 2,2-dimethylbutane.

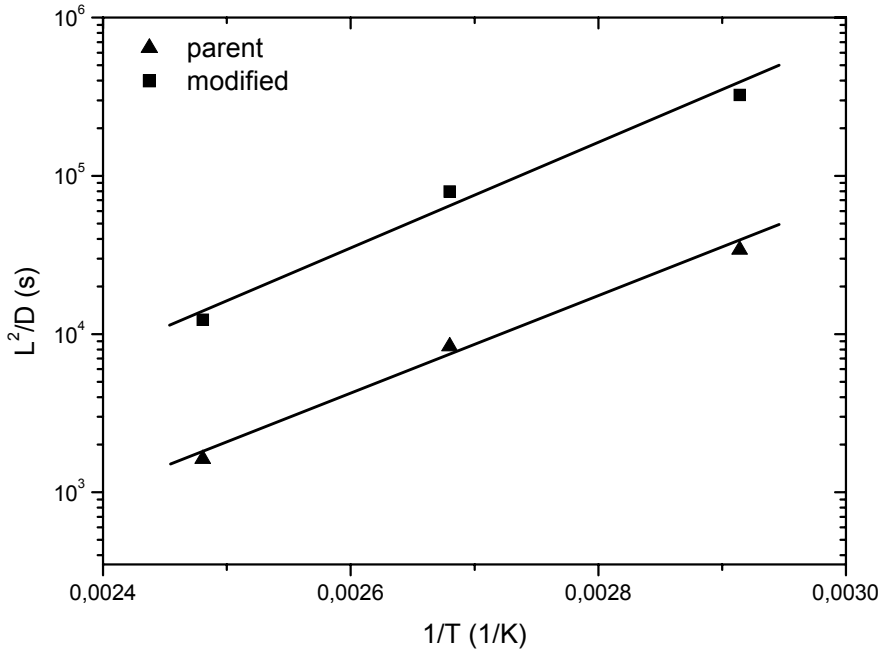

Figure 5.5: Arrhenius plots of the time constants of 2,2-dimethylbutane uptake for the parent and modified sample.

5.4 Discussion

From the analysis of the sorption properties, it is obvious that they do not account for the observed effects. Their interpretation requires the understanding of the steps involved during the transport of gas phase molecules into the porous particle (Gobin et al., 2009a, Reitmeier et al., 2009b). This situation is schematically represented in Figure 5.6 for the unmodified and for the modified zeolite. In particular the steps involved in the transport from the gas phase (A) to the zeolite (B) are: the sorption of a molecule on the external surface (a+b), described by the probability that a gas phase molecule is adsorbed on the external surface of the particle after collision, i.e., the sticking probability, the entering into the pore (c), and the intracrystalline diffusion (d). For the surface modified zeolite, in between the gas phase (A) and the zeolite (B) an amorphous layer (C) is present, changing the properties of the surface and of the subsequent transport steps (e) to (g).

In the series of transport steps, the rate limiting step seems to be shifted from a situation that is limited by adsorption and pore entering for hexane, 2MP and 3MP to a situation limited by intracrystalline diffusion in the case of 22DMB. This assumption can be checked by calculation of the intracrystalline diffusion time constant assuming a primary particle size of 50 to 100 nm using the corrected vapor phase diffusivities of nH (5x10^{-13} m^2/s), 2MP (10^{-13} to 2x10^{-14} m^2/s), 3MP (2x10−14 m^2/s), 23DMB (10^{-15} m^2/s), and 22DMB (10^{-18} - 10^{-19} m^2/s) at 70 °C in ZSM-5 as reported in the literature by Boulicout et al.31. Diffusion time constants of 10^{-2} to 10^{-1} s would be obtained for nH, 2MP, and 3MP. For 23DMB and 22DMB time constants in the range of 2 to 10 s (23DMB) and 10^3 to 10^4 s (22DMB) would be expected. This clearly confirms the assumption, that the system is adsorption limited for nH and the one-time methyl substituted alkane molecules 2MP and 3MP. In contrast, for 22DMB the system is limited by intracrystalline diffusion, while for 23DMB all kinetic steps are of similar rate as the calculated time constant of intracrystalline diffusion is similar to the one observed by uptake experiments.

In the following, the effects on systems which are adsorption limited will be discussed first. Besides nH, 2MP and 3MP also the transport of benzene and toluene as reported and discussed in several previous studies1,8 is adsorption limited. The first step of the kinetic transport network is the sticking of the molecules to the external surface of the particle, which can be quantified by the sticking probability. The experimentally obtained sticking probabilities along with theoretical calculations of the moments of inertia, the rotational partition functions and the derived theoretical sticking probabilities are given in Table 5.6. Low sticking probabilities in the order of 10^{-6} are obtained for all the hexane isomers. The sticking probability can in general be regarded as the successful

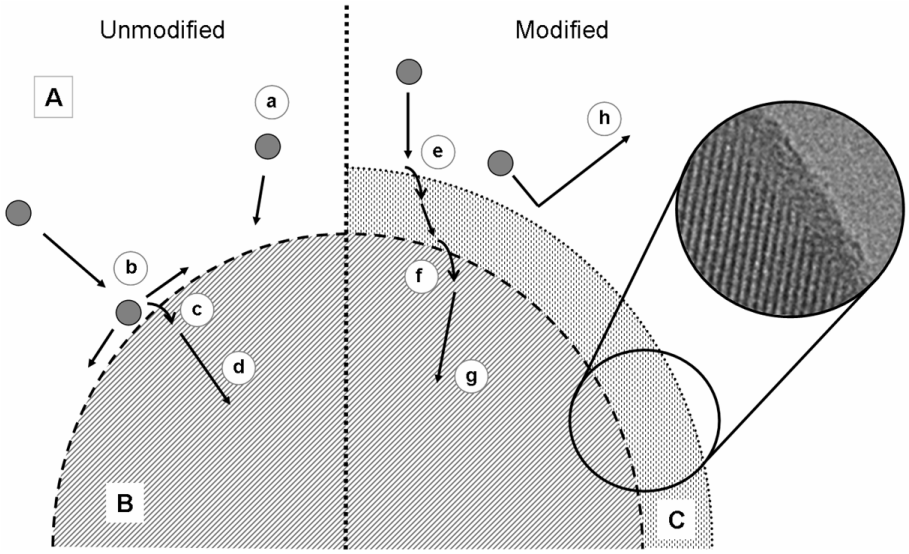

Figure 5.6: Scheme illustrating the interconnected sorption and transport pathways on unmodified (left) compared to surface modified (right) zeolites. For the unmodified one, gas phase molecules (A) collide and adsorb on the zeolite (B) surface in a weakly bound physisorbed state (a+b), which is followed by pore entering (c) and intracrystalline diffusion (d). On modified zeolites, molecules do not collide with the zeolite surface anymore, but with the amorphous silica surface overlayer (C) and with a certain probability, they can directly enter (e) the overlayer porosity. A subsequent step (f) is necessary here to access the crystalline zeolite core hidden below this overlayer, shown in the TEM inset. Molecules not trapped onto the surface are instantaneously rejected to the gas phase (h) (Reitmeier et al., 2009b)

trapping of the molecules originating from the gas phase into a weakly bound physisorbed state. As discussed by Reitmeier et al. (Reitmeier et al., 2009c) four interconnected factors influence the absolute value of the sticking coefficient α: (1) the degrees of translational and rotational freedom lost, (2) the initial entropy of the gas phase molecule, (3) the compensation of the heat of sorption, and (4) the geometrical dimensions of the molecules that determine the space occupied on the surface. According to van Santen and Kramer (1995), van Santen and Niemantsverdriet (1995), the observed (apparent) sticking coefficient is given by the product of the theoretical sticking coefficient $\alpha^{\#}$, which is determined by the first two factors, and the trapping coefficient χ, which is determined by the latter two factors:

$$\alpha = \chi \cdot \alpha^{\#} \tag{5.5}$$

The theoretical sticking coefficient can be theoretically calculated when the rotational q_{rot} and vibrational q_{vib} partition functions of the molecules in the gas phase and adsorbed on the surface are known:

$$\alpha^{\#} = \frac{q_{\mathrm{rot}}^{\mathrm{surf}} \cdot q_{\mathrm{vib}}^{\mathrm{surf}}}{q_{\mathrm{rot}}^{\mathrm{gas}} \cdot q_{\mathrm{vib}}^{\mathrm{surf}}} \tag{5.6}$$

Herein, the rotational partition function q_{rot} assuming free rotation around all principal axes (x, y, z) is given by:

$$q_{\mathrm{rot}}^{\mathrm{gas}} = \frac{1}{\delta} \left(\frac{8\pi^2 kT}{h^2} \right)^{3/2} \cdot \sqrt{\pi I_x I_y I_z} \tag{5.7}$$

The expression for the theoretical sticking coefficient $\alpha^{\#}$ given in equation 5.6, already accounts for the reduction of the translational degrees of freedom, assuming that the molecule looses one degree of freedom (from three to two) upon sorption (van Santen and Kramer, 1995). The required moments of inertia for the hexane isomers were calculated using Gaussian after energy minimization of the structure of the molecule. It is noted, that different conformations of the alkane molecule lead to slight changes in the moments of inertia, or in the respective rotational partition function. From theoretical calculations performed by Vansteenkiste et al. (2005), the partition function may be overestimated at most by 18%, which is still reasonable for the estimation given in this work. In addition, it is assumed in a first approximation, that only the free gas phase rotations are hindered during the trapping of the molecule on the surface, while changes in the vibrational contributions are of minor importance and will be neglected in our estimations.

Assuming total loss of all external rotational degrees of freedom upon sorption, the theoretical sticking coefficients as given in Table 5.6 are obtained. Compared to the sticking probabilities derived for the aromatic molecules in previous studies (Reitmeier et al., 2009b,c), the experimental sticking probabilities are about one order of magnitude

sorbate	σ	I_x	I_y	I_z	q_{rot}	α_{theory}	α_{parent}	α_{mod}	χ_{parent}	χ_{mod}
	-	10^{-45} kg m^2	10^{-45} kg m^2	10^{-45} kg m^2	x 10^5	x 10^{-6}	x 10^{-6}	x 10^{-6}	-	-
nH	2	0.58	7.50	7.76	1.28	7.82	2.08	3.39	0.27	0.43
2MP	1	1.28	4.99	1.15	1.19	8.39	1.04	3.59	0.12	0.43
3MP	2	1.29	4.60	5.34	1.24	8.05	1.12	2.52	0.14	0.31
23DMB	2	2.02	2.95	4.54	1.14	8.74	0.89	0.79	0.10	0.09
22DMB	1	1.98	3.41	3.43	2.12	4.71	-	-	-	-

Table 5.6: Symmetry number σ, moments of inertia along the principal axes I_x, I_y, I_z, rotational partition function q_{rot}, theoretical and experimental sticking probabilities α, and trapping coefficients χ of the sorbates on the ZSM-5 samples. Calculations were performed in Gaussian and theoretical sticking probabilities were calculated by statistical thermodynamics assuming total loss of the external rotational degrees of freedom upon sorption. It is important to note, that the experimental values for 23DMB and 22DMB are influenced by intra-crystalline diffusion and, therefore, can not be compared to the data of nH, 2MP, or 3MP.

larger. This can be explained by the fact that all carbon atoms are sp^3 hybridized, leading to more internal degrees of rotational freedom that are preserved during adsorption into a weakly bound physisorbed state for the alkanes compared to the aromatic molecules. In addition, the heat of adsorption and the space required on the surface is higher for the alkane molecules leading to relatively high trapping coefficients χ of about 0.10 to 0.30 for the parent sample to about 0.40 for the modified sample were obtained (Table 5.6).

Compared to the trapping coefficient of the aromatic molecules, the values for the hexane isomers are one magnitude higher. This is attributed to the fact, that the trapping coefficient describes the probability of a molecule to be trapped into a physisorbed state due to exothermic collision on a surface (van Santen and Kramer, 1995, van Santen and Niemantsverdriet, 1995) and, as stated before, it is directly related to the space the molecule requires on the surface and to the accommodation of energy. In this context, it can be noted that the alkane molecules studied inherently possess more vibrational degrees of freedom (3N-6) compared to the aromatics (comparable number of C atoms). This allows for a much better dissipation of the energy released upon collision and of the heats released upon adsorption. It is interesting to see that with increasing dimensions on the surface the trapping coefficient increases (see Table 5.6). n-Hexane shows the highest trapping coefficient, as it has the highest heat of adsorption and, due to its length, it requires statistically more space on the surface as for instance 2,3-DMB.

Upon modification, for all molecules, which are not limited by intracrystalline diffusion,

i.e., nH, 2MP, and 3MP, the trapping and also the sticking coefficient increases. This is due to the fact that the probability of a direct pore entering from the gas phase into the small zeolite pores ($\backsim$0.55 nm) is very low according to Skoulidas and Scholl (2000). In contrast, direct pore entering of the molecules into the larger pores ($\backsim$1.5 nm) of the amorphous surface layer is possible, as the ratio of the pore diameter and the sphere that the rotating molecule takes up is more favorable leading to a marked increase of the initial trapping probability (in Figure 5.6, step e). This situation is identical to the one described previously for the aromatic compounds, and it shows, that the remarkable way of sorption enhancement reported for aromatic compounds is also valid for flexible molecules.

2,2-dimethylbutane is a molecule that barely fits into ZSM-5 and, therefore, the transport investigated in this study is limited by intracrystalline diffusion. Due to this fact, this molecule is a very interesting candidate for the investigation of certain properties of the surface layer, which cannot be observed for smaller and adsorption limited molecules. Upon modification, the transport of 22DMB decreases by one order of magnitude as reported in Table 5.5. This cannot be explained by a decreased sticking coefficient. According to the theoretical estimates compiled in Table 5.6 and to the equilibrium measurements in Table 5.3, a trapping and sticking coefficient very similar to the one of the other hexane isomers would be expected.

Experimentally, however, the determination of the sticking coefficient is not possible, as the transport is not determined by the surface processes. In Table 5.5 the activation energy of the 22DMB transport process is given. It can be easily seen, that the activation energy does not change upon modification, which is an indication that the energy surface is identical for both the parent and modified sample. Only an additional entropic barrier is created, as the pre-exponential factor of the Arrhenius relation (see Table 5.5) is decreases by half an order of magnitude after surface modification. In conclusion, the surface modification does not change the intrinsic transport for 22DMB, that is, the diffusion inside the ZSM-5 framework, but creates a major entropic surface barrier. This is confirmed by the fact that after correction of the deposited SiO_2 mass, the micropore volume is the same for the parent and for the modified sample as given in Table 5.2. Therefore, blocking of intracrystalline pores due to a possible hydrolysis of TEOS upon modification can be excluded.

The physical nature of the created surface barrier can be in principle: (1) a complete blocking of a certain amount of pore openings, (2) a narrowing of the pore openings by the silica deposition, or (3) that the flexibility of the zeolite framework is affected by the amorphous silica layer, leading to more rigid pore openings. All three possibilities have in common, that they introduce an additional barrier to the transport. The first option,

however, differs from the two others. In this case mathematically the characteristic length of the diffusion pathway is increased, leading to an increased number of molecule reorientations in order to find an open pore, whereas the physical nature of the open pore itself is not changing. Options (2) and (3) are hard to differentiate and a combination of both effects is reasonable to assume. In both cases, reorientation and distortion of the molecule as well as of the zeolite framework are necessary for the successful entering into the pores of the zeolite. Due to the fact that the activation energy of the transport of 22DMB is not changing, and thus, an entropic surface barrier is expected, only option (1), that is, a complete pore blocking is reasonable for 22DMB. In the case of options (2) or (3) a change in the activation energy would be expected, as additional energy is required in order to distort either the zeolite framework or the molecule itself. A complete pore blocking of a certain number of surface pores is consistent with previous studies, where the surface properties were investigated by adsorption of di-tert-butyl-pyridine (DTBPy) (Zheng, 2002). It was found, that 28% of the total bridging hydroxyl groups interacted with DTBPy, and thus, must be located at the zeolite surface in the pore mouth region. After modification 76% of these sites were removed by the silica deposition. These pore openings are likely to be completely blocked for 22DMB, and, thus, confirm the entropic nature of the surface barrier. Interestingly, one should note, that the transport of 22DMB was first limited by intracrystalline diffusion for the parent sample. After modification and creation of an important entropic barrier at the surface, the limiting step of the overall transport shifts to the pore entering step, that is then also significantly more demanding.

sorbate	Direct pore entering and pre-orientation	Surface barrier	Intracrystalline diffusion	Observed effect
nH	enhancing	no effect	no effect	enhanced
2MP	enhancing	no effect	no effect	enhanced
3MP	enhancing	no effect	no effect	enhanced
23DMB	enhancing	no effect	limiting	no effect
22DMB	enhancing	negative	limiting	negative
benzene	enhancing	no effect	no effect	enhanced
toluene	enhancing	no effect	no effect	enhanced
p-xylene	enhancing	negative	no effect	negative

Table 5.7: Summary of the rate enhancing (green) and decreasing effects (red), and the resulting observed effect on the overall transport for iso-alkanes and aromatic compounds.

In conclusion, the surface modification increases the sticking and trapping of molecules smaller than the pores of the amorphous surface layer. This can be related to an increased direct pore entering probability as reported in detail for aromatic molecules by Reitmeier et al. (2009b) (Figure 5.6, step e). Once a molecule is trapped, the pore entering into the zeolite lattice is also enhanced, as the molecule orientates and is guided to the parent zeolite pores (Figure 5.6, step f). This situation leads to an enhanced adsorption and pore entering rate compared to the unmodified sample in the case of molecules with small critical diameters, i.e., critical diameters that are distinctly smaller than the pores of the parent zeolite. For molecules with similar or even slightly larger pore diameters, the surface modification leads to a decreased pore entering rate (Figure 5.6, step f), as an additional entropic surface barrier is created as described in the last section. In other words, the rate of the pore entering step for the unmodified zeolite (Figure 5.6, step c) is faster compared to the pore entering for the modified sample (Figure 5.6, step f) for molecules with critical diameters similar or even larger than the parent zeolite pores. This situation is in principle independent of the rate of the intracrystalline diffusion. However, if the intracrystalline diffusion is very slow and, thus, rate limiting, the favorable sorption enhancing effect of the amorphous layer is not visible anymore, and the overall transport is independent of the surface modification or is decreased, due to the creation of an additional entropic surface barrier. This is the reason, why a sorption enhancing effect was not observed up to now for zeolitic systems composed of large ($> 100\mu$m) zeolites crystallites (Chmelik et al., 2007). In table 5.7, all these effects are summarized in order to give a clear overview of the different systems. The results of the aromatic compounds obtained in previous studies (Gobin et al., 2009a, Reitmeier et al., 2009b) are also included in this Table.

5.5 Conclusions

Surface modification by chemical liquid deposition of TEOS can be used to post-synthetically modify the transport properties of nano-sized ZSM-5 crystals. If the transport of the guest molecules is not limited by intracrystalline diffusion and the size of the molecule is distinctly smaller than the pore diameter of the surface overlayer, a sorption enhancing effect can be observed. The surface modification, however, creates a significant entropic surface barrier, if the critical diameter of the adsorbed molecules is similar or distinctly larger compared to the ZSM- 5 lattice pores. The physical nature of this barrier can be a combination of a pore blocking or narrowing and an increased rigidity of the pore entrances due to the surface overlayer. For molecules distinctly smaller than the ZSM-5 pores, no additional entropic barrier is created. These conclusions are valid for rigid aromatic molecules, i.e., benzene, toluene, and p-xylene, as well as for flexible linear or non-linear alkanes as shown by the sorption of the hexane isomers within this work. This confirms the general feasibility of tailoring transport properties by surface modification of zeolites.

6 Diffusion in Circularly Ordered Mesoporous Silica Fibers

This chapter was published in the Journal of Physical Chemistry C as research article

Diffusion in circularly ordered mesoporous silica fibers
Oliver C. Gobin, Hatem Alsyouri, Andreas Jentys, and Johannes A. Lercher J. Phys. Chem. C; **2011**; 115(17), pp 8602–8612

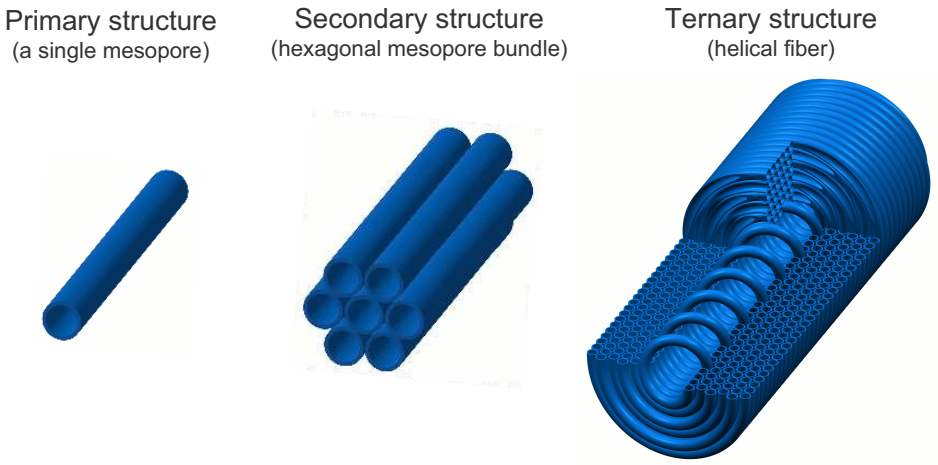

Abstract The investigation of transport processes in complex hierarchical materials is reported based on diffusion measurements of n-hexane and mesithylene in circularly ordered mesoporous silica fibers. Using the frequency response method, it is possible to differentiate between several kinetic processes occurring in the silica fibers. By comparing theoretical calculations based on the complex hierachical structure with the experimental results from the frequency response experiments, a clear identification of the transport pathways in the fibers is reported. Three pathways were observed: diffusion in axial, tangential, and radial direction. All these processes are occurring in parallel. The radial diffusion is the dominant process and is governed by intrawall transport. Transport in axial direction overlaps the radial diffusion and can be either governed by intrawall or by mesopore transport. Cracks or defects at the surface enable diffusion in tangential direction, which is the third kinetic process experimentally observed.

6.1 Introduction

Ordered mesoporous fibers (Kleitz et al., 2001, Marlow et al., 2000) are an interesting novel type of materials of the M41 S family, with a unique morphology and internal structure. The cylindrical shape of the fibers is formed by hexagonally-packed tubular pores, similar to those of MCM-41, which are coiled around the central axis of the fiber (Marlow et al., 2007). Silica fibers possess longer pores compared to particulate MCM-41 materials. This feature can be attractive for applications employing the pores as nanoreactors such as extrusion polymerization where properties of polymer chains can be influenced by the pore length (Ye et al., 2003). The complex internal structure of these fibers, however, is not fully understood. For instance, it is unclear, if diffusion perpendicular to the fibers is important or if the diffusion only takes place across the fibers inside the mesopores. Recently, the interpretation of diffusion results (Alsyouri and Lin, 2005) of different probe molecules was controversially discussed (Lin and Alsyouri, 2006, Marlow and Stempniewicz, 2006), but there is still a lack of a clear identification of the diffusive processes inside such fibers.

In the last decades the frequency response (FR) method has been adapted to measure diffusion in porous solids (Yasuda, 1994a). One conceptual advantage of this method is the possibility to measure the significant kinetics of a system simultaneously with option to disentangle the individual contributions subsequently. Therefore, this technique allows to identify multiple diffusive flows inside the mesoporous silica fibers and to quantify the contribution of these processes. Such clarification is especially useful in understanding the behavior of mesoporous silica fibers in real applications. For example, this morphology is being prepared as membranes for applications as modulated nanoreactors, where the silica fibers are grown as plugs inside the openings of straight pore supports (Seshadri et al., 2010). In oder to understand how solutes and products pass through the supported helical pores of the silica plugs a clear identification and quantification of the diffusion mechanisms in this class of materials is required.

In this work, the diffusion of n-hexane and mesitylene was investigated by means of the frequency response method. Two fiber samples, with a different average fiber length were investigated, in order to identify the dependence of the diffusional time constant with the length of the fibers.

6.2 Experimental section

6.2.1 Materials

Mesoporous silica fibers were prepared by the self-assembly method as described in detail by Alsyouri and Lin (2003), Ye et al. (2003). Tetrabutylorthosilicate (TBOS) silica precursor was added on the top of a pre-mixed water solution containing cetyltrimethylammonium bromide (CTAB) surfactant and HCl acid without mixing creating a two-phase mixture. The silica fibers grow under quiescent conditions at the interface. After two weeks, the silica product were collected, dried and calcined at 823 K. The silica product contains fibers of various lengths accompanied by particles with various shapes. Therefore, samples containing uniform fibers and non-fibrous particles were separated by sieving. The fiber length was subsequently reduced by crushing the sample containing uniform fibers.

6.2.2 Physicochemical characterization

Nitrogen physisorption isotherms were measured using a PMI automated sorptometer at liquid nitrogen temperature (77 K), after outgassing under vacuum at 473 K for at least 6 h. The apparent surface area was calculated by applying the Brunauer-Emmett-Teller (BET) theory to the adsorption isotherms over a relative pressure range from 0.10 to 0.30 p/p_0. The pore volumes were evaluated using the α_s comparative plot (**?**) using nonporous hydroxylated silica (Gregg and W., 1982) as the reference adsorbent. In addition, calculations based on the non-local density functional theory (NLDFT) were performed using the Quantachrome Autosorb 1 software. As DFT kernel, the nitrogen equilibrium model at 77 K on silica was used. Because of the limitations of the PMI instrument, the isotherms were measured at relative partial pressures higher than $10^{-5}p/p_0$. SEM images were recorded on a REM JEOL 5900 LV microscope operating at 25 kV with a resolution of 5 nm and a nominal magnification of 3.0 x 10^6. For scanning electron microscopy (SEM), the powdered samples were used without any pretreatment or coating. Transmission electron microscopy (TEM) was measured on a JEOL-2011 electron microscope operating at 200 kV. Prior to the measurements, the samples were suspended in ethanol solution and dried on a copper-carbon-grid. The X-ray powder diffraction (XRD) patterns were measured on a Philips X'pert Pro XRD instrument operating with the energy of Cu-K_α1-radiation at 40 kV using a Ni-filter to remove the Cu-K_β-line. Data points were recorded using a spinner system with a 1/4 inch slit mask between 2θ angles of 1.5° to 8° with a step size of 0.017° and a scan speed of 115 s per step.

6.2.3 Gravimetric sorption experiments

The gravimetric sorption capacities of the molecules were measured on a Setaram TG-DSC 111 thermoanalyzer. Activation was performed at 823 K for 1 h with a heating rate of 10 K min^{-1} under vacuum ($p < 10^{-7}$ mbar). The weight increase and the thermal flux were measured during equilibration with the sorbate using small pressure steps up to 13 mbar. The heats of adsorption were directly obtained by integration of the observed heat signal.

6.2.4 Frequency response experiments

30 mg of powder sample was carefully dispersed on several layers of quartz wool at the bottom of a quartz tube in order to avoid artifacts from bed- depth effects. The sample tube was connected to a vacuum system, placed inside a heating oven and pumped to 10^{-7} mbar at room temperature. The samples were heated to 823 K with a ramp of 10 K/min and activated under vacuum below 10^{-7} mbar for one hour to remove adsorbed water. The sorbate gases were added with a partial pressure of 0.3 mbar into the system at temperatures between 333 and 423 K. After the sorption equilibrium was fully established, the volume of the system was modulated periodically by two magnetically driven plates sealed with UHV bellows in the frequency range of 0.001 to 5 Hz. The modulation resulted in a square-wave perturbation of the system volume with an amplitude of (1 %. The pressure response of the system to the volume perturbation was recorded with an on- line Baratron pressure transducer (MKS 16A11 TCC). The amplitude and the phase lag of the frequency response were obtained by Fourier transformation of the pressure data. Nonlinear parameter fitting of the theoretical characteristic functions to the experimental frequency response was performed by using the CMA evolution strategy in Matlab (Hansen, 2006). The root mean squared error normalized to the variance of the data (NRMS error) was used as the objective function to be minimized. To ensure that the globally optimal parameter set was found, each optimization run was repeated three times with varying parameter sets of the evolution strategy.

The influence of heat or bed-depth effects was checked by variation of the sample amount and by the way the sample was placed in the sample tube, i.e., with and without dispersing the sample on quartz wool. In all cases the same frequency response was observed and therefore, we can exclude heat or bed-depth effects. An experimental error of less than 5% was obtained for the resulting FR parameters by performing the same experiment several times.

6.3 Results

6.3.1 Characterization results

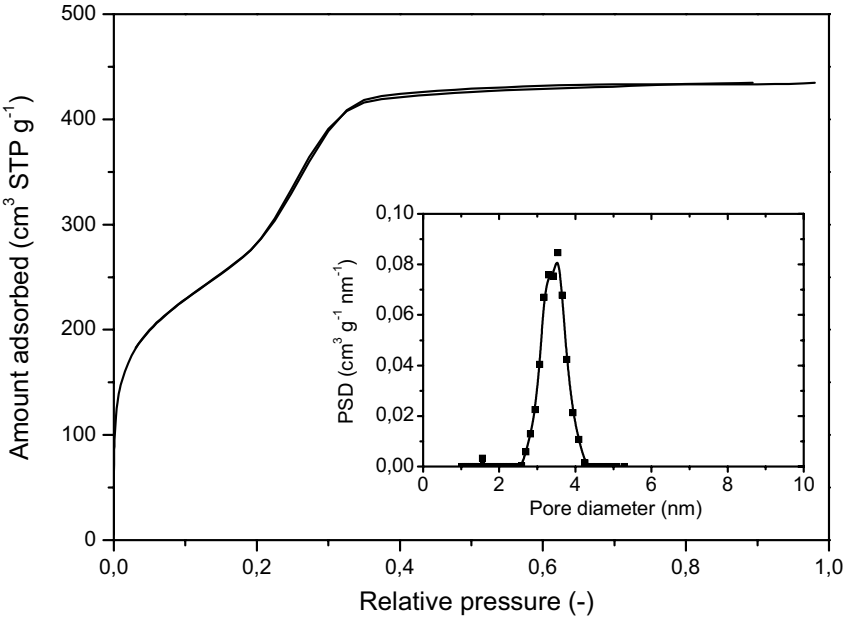

Figure 6.1: N_2-Physisorption isotherm and the DFT pore size distribution (inset).

The internal structure of the fibers was analyzed by XRD, TEM, and nitrogen physisorption. The reflections of the XRD pattern given in Figure 6.2 correspond to a hexagonal mesophase clearly showing the (100), (110), and (200) reflections. The internal hexagonal structure of the fibers was confirmed by TEM images as shown in Figure 6.3. From the XRD pattern a $d(100)$ spacing of $d = 3.72$ nm and a unit cell parameter of $a_0 = 2/\sqrt{3} \cdot d_{100}$ =4.30 nm can be calculated. The pore structure was furthermore analyzed by nitrogen physisorption. The isotherm shown in Figure 6.1 is a typical type IV isotherm with a high initial adsorption at low pressures and a well defined capillary condensation step at $0.3p/p_0$ indicating a very uniform and narrow pore structure. By applying the BET theory a surface area of $S_{\mathrm{BET}} = 1008$ m^2/g was calculated. The pore volumes were obtained using the t- and α_s-comparative plot method. In both cases an intercept close or below zero was observed, which is a clear confirmation that no or only a very small amount of micropores are present very similar to the situation in MCM-41.

A total pore volume of $V_{\mathrm{tot}} = 0.64$ cm^3/g and a mesopore volume of $V_{\mathrm{me}} = 0.63$ cm^3/g was obtained. A mesoporosity $\epsilon_{\mathrm{me}} = \rho V_{\mathrm{me}}/(1 + \rho V_{\mathrm{tot}})$ of 0.58 was calculated assuming a constant framework density of $\rho = 2.2$ g/cm^3 (Chen et al., 2004, Sayari et al., 1997). The pore size can also be obtained by geometrical considerations

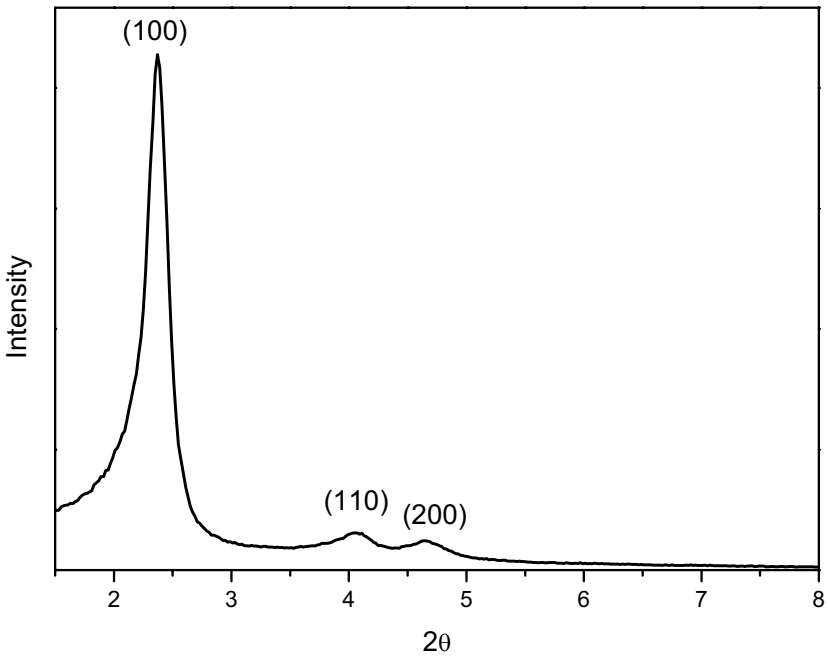

Figure 6.2: XRD pattern of the fiber sample.

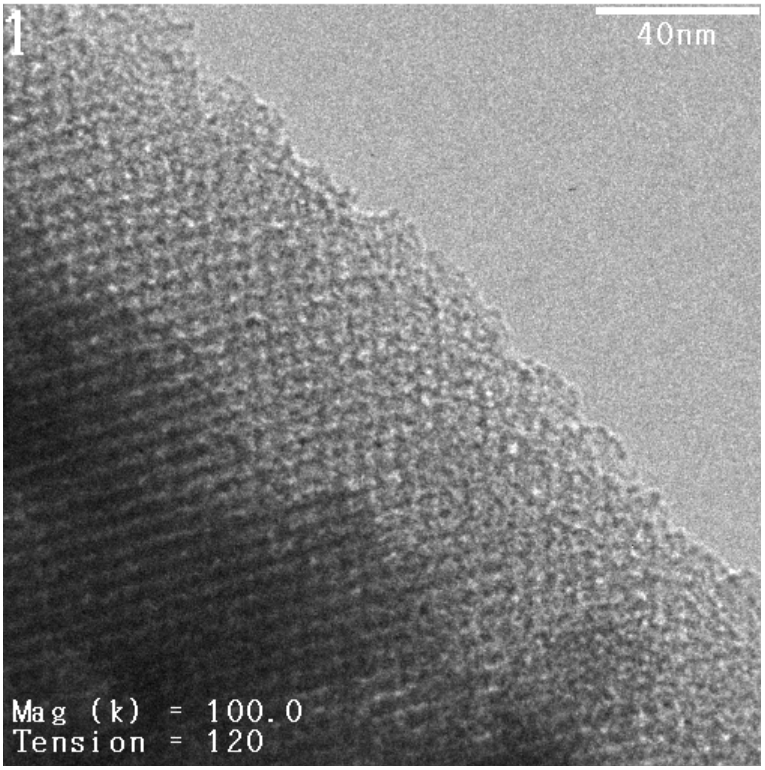

Figure 6.3: TEM micrograph of the fiber sample.

$w_{\mathrm{pore}} = c \cdot d \cdot (\rho V_{\mathrm{me}}/(1+\rho V_{\mathrm{me}}))^{1/2}$, where $c = 1.213$ from the XRD $d(100)$ spacing and the mesopore volume V_{me} (Sayari et al., 1997). Using this relation, a pore size of $w_{\mathrm{pore}} = 3.44$ nm was calculated. This pore size is in good agreement with the pore size $w_{\mathrm{DFT}} = 3.53$ nm obtained from the DFT pore size distribution as can be seen in the inset of Figure 6.1. Consistent with the results from the α_{s}-plot, only one pore population could be identified from the DFT calculations. No micropores are visible in the pore size distribution. By application of the BJH analysis an average pore diameter of $w_{\mathrm{BJH}} = 2.35$ nm pores was obtained. It is known that the BJH-theory systematically underestimates the pore size, therefore this pore size is considered to represent a physically wrong value. The pore wall thickness can be calculated from the difference between the pore size and the unit cell parameter. In the case of the DFT calculations a wall thickness of ∼0.85 nm is obtained. All the structural properties of the sample are summarized in Table 6.1.

S_{BET}	V_{mi}	V_{me}	V_{tot}	w_{BJH}	w_{DFT}	w_{d}	ϵ
m^2/g	cm^3/g	cm^3/g	cm^3/g	nm	nm	nm	-
1008	0.01	0.63	0.64	2.35	3.53	3.44	0.58

Table 6.1: Textural properties of the fibers. V_{mi}, V_{me}, and V_{tot} are the micropore, mesopore, and total pore volume as obtained by the α_{s}-plot. w_{BJH}, w_{DFT}, w_{d} is the mesopore diameter as obtained by BJH, DFT, and by geometric considerations from XRD. ϵ is the mesoporosity.

The particle morphology was studied using SEM. It can be easily seen that the as synthesized material contains two types of particles. These are nearly uniform fibers with a length up to a few millimeters and a thickness of 15 to 25 μm and small spherical particles. These particles are denoted as small rotational symmetric particles according to Marlow et al. (2007). Their diameter is similar to the thickness of the fiber and their internal structure is also composed of ordered hexagonally arranged mesopores belonging to the class of SBA-3 materials (Marlow et al., 2007). A differentiation between fibers and the small rotational symmetric particles is only possible by XRD by performing several measurements at different sample orientations (Marlow et al., 2005). In this case, the relative intensities of the XRD reflections change. For diffusion measurements a high uniformity of the particles drastically facilitates the interpretation. Therefore, the small particles were separated from the fibers by sieving in order to have a sample only composed of fibrous shapes. This sample is denoted as parent fiber sample. Subsequently, the fiber length was reduced by mechanically breaking the fibers, resulting in a sample predominantly composed of small fiber pieces denoted as crushed fiber sample. In Figure 6.4 the SEM images of the sample containing the parent fibers (a), the non-uniform and

small rotational symmetrical particles (b), and the crushed fibers (c) are shown. It can be easily seen, that the length of the crushed fibers was drastically reduced. By SEM an average length of about 50 μm was obtained, in contrast to an average length of the parent fibers of about 300 μm.

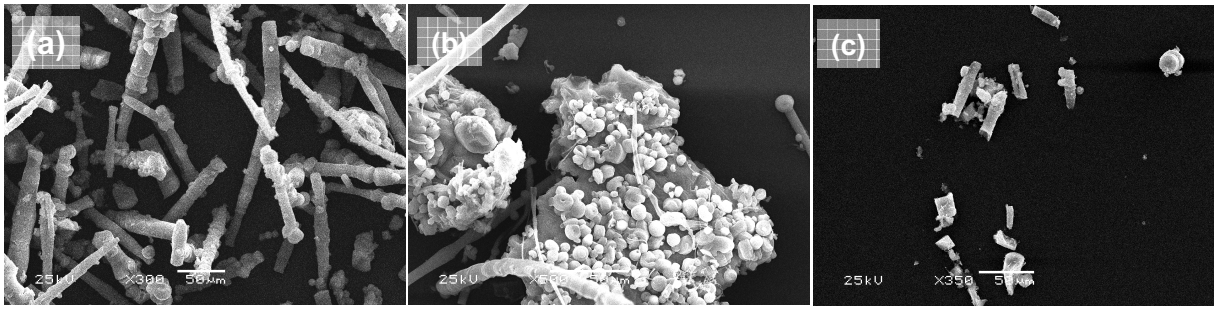

Figure 6.4: SEM images of the fiber sample. (a) the parent sample only containing fibers, (b) the fraction of non-fibrous particles, and (c) the crushed fiber sample.

Important for the quantitative evaluation of the transport experiments is the knowledge of the adsorption properties of hexane and mesitylene at the corresponding temperatures. The adsorption isotherms for mesitylene are shown in Figure 6.5. Up to 13 mbar the isotherms are in all cases linear, and therefore a simple Henry isotherm was used to fit the experimental data. Relatively low dimensionless weight-based Henry constants of 101, 32, and 10 at 70 °C, 100 °C, and 130 °C and a heat of adsorption of 44 kJ/mol were obtained for mesitylene.

6.3.2 Frequency response results

The frequency response results were performed using n-hexane and mesitylene as probe molecules on the parent and crushed fiber sample. The frequency responses of n-hexane for the parent and crushed fiber sample at 30 °C are shown in Figure 6.6. In all cases it can be clearly seen, that the in-phase characteristic function is not approaching zero at high frequencies and, thus, the in- and out-of-phase characteristic function are not crossing in the measured frequency range. This unusual behavior was observed for the first time in this system. An improper reference or blank measurement would be an explanation for such characteristic function. The reference measurement, however, was repeated several times in order to verify and validate the measurements and in all cases characteristic functions showing this behavior were obtained.

Beside an improper reference measurement, the only physically reasonable explanation is a second fast kinetic process located in the high frequency range above 10 Hz. Due

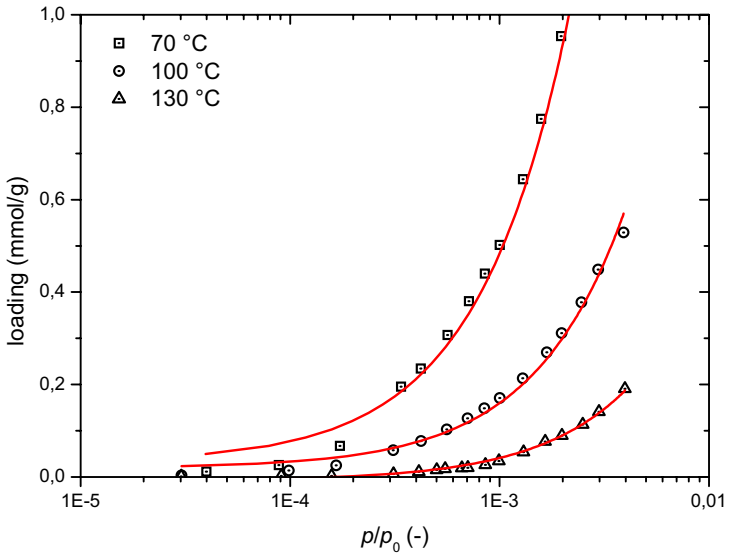

Figure 6.5: Sorption isotherms of mesitylene at 70 °C, 100 °C, and 130 °C of the fiber sample. The fits are linear fits based on Henry's law.

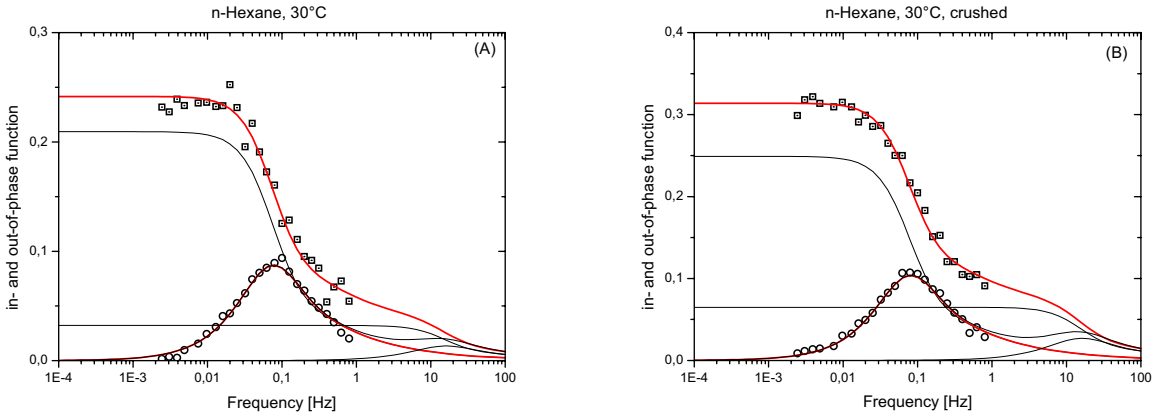

Figure 6.6: Frequency responces of n-hexane in (a) the parent, and (b) the crushed sample at 30 °C.

to the limitation of the frequency response apparatus, such high frequencies cannot be directly measured; however, such a fast process would exactly show the characteristics we observe in the frequency response. That is, the fast kinetic process is not visible in the out-of-phase characteristic function, whereas it appears indirectly as an offset in the in-phase characteristic function of the frequency response. Assuming two kinetic processes, the experimental n- hexane frequency responses can be fitted with a high accuracy. The exact location, that is, the exact time constant of the fast kinetic process cannot be unambiguously determined as the location is given by the out-of- phase characteristic function. Therefore, an arbitrary time constant located in the frequency region above 10 Hz was assumed. Only the amplitude of the response, that is, the relative number of molecules involved in this transport step (K_{FR} value in equation 2.47) can be accurately determined by the offset of the in-phase characteristic function. In Table 6.2 the kinetic data obtained from the fitting of the experimental frequency responses of n- hexane is given.

Sample	T	τ_1	τ_2	$K_{\mathrm{FR},1}$	$K_{\mathrm{FR},2}$	$K_{\mathrm{FR},1} + K_{\mathrm{FR},2}$	$\frac{K_{\mathrm{FR},1}}{K_{\mathrm{FR},1}+K_{\mathrm{FR},2}}$	σ
	°C	s	s	-	-	-	-	s
parent	30	20.9	0.10	0.21	0.03	0.24	0.87	0
crushed	30	19.9	0.10	0.19	0.05	0.24	0.79	0

Table 6.2: Frequency response data for n-hexane. τ_1 is the kinetic process visible in the frequency response, τ_2 is the kinetic process at high frequencies, that can not be directly measured. The exact value of this process is not known. $K_{\mathrm{FR},1}$ and $K_{\mathrm{FR},2}$ are the contributions of the processes as given by equation 2.47. $K_{\mathrm{FR},1}/(K_{\mathrm{FR},1} + K_{\mathrm{FR},2})$ is the relative contribution of τ_1, and σ is the variance of the distribution as obtained by the fitting.

Due to the fact that the characteristic length of the transport process is not known, only the time constants (L^2/D), not the diffusivities, are given in Table 6.2. Corresponding diffusivities can be calculated by assuming a certain characteristic length L of the diffusion pathway. From Table 6.2, it can be seen that the time constants of the slow kinetic process, i.e., $\tau_1 \approx 20$ s, are identical for the parent and crushed sample. The shape of the out-of-phase frequency response is very narrow and can be nicely fitted by an ideal 1D diffusion model (Figure 6.6). No convolution of multiple diffusion processes due to a distribution in particle size or a distribution of diffusivities is present for n-hexane in the parent and crushed fiber sample, i.e., the variance σ was set to zero during the fitting as given in Table 6.2. From the K_{FR} values obtained by fittingby fitting the experimental frequency responses, the contribution of the very fast transport process at frequencies

higher 1 Hz and of the slow process can be calculated. In Table 6.2 the values along with the relative contribution of the slow process to the overall transport $K_{\mathrm{FR},1}/(K_{\mathrm{FR},1}+K_{\mathrm{FR},2})$ are given. Herein the K_{FR} values were corrected by the corresponding sample mass. The dominant process with a contribution of 80% is the slow transport process for both samples. A very slight increase of the contribution of the fast process can be observed for the crushed sample.

Sample	T	τ_1	τ_2	$K_{\mathrm{FR},1}$	$K_{\mathrm{FR},2}$	$K_{\mathrm{FR},1}+K_{\mathrm{FR},2}$	$\frac{K_{\mathrm{FR},1}}{K_{\mathrm{FR},1}+K_{\mathrm{FR},2}}$	σ
	°C	s	s	-	-	-	-	s
parent	70	71.3	0.10	2.25	0.28	2.53	0.89	4.97
	100	32.4	0.10	1.14	0.38	1.52	0.75	3.00
	130	24.1	0.10	0.87	0.38	1.26	0.69	2.93
crushed	70	51.6	0.10	2.07	0.43	2.50	0.83	9.46
	100	28.9	0.10	1.23	0.45	1.68	0.73	4.50
	130	23.3	0.10	1.07	0.50	1.57	0.68	3.85

Table 6.3: Frequency response data for mesitylene. Parameters and variables are given in the description of Table 6.2.

In order to measure the transport with a molecule large enough not to diffuse through small micropores in the framework, the transport of mesitylene was also investigated. The transport was distinctly slower than the one of n-hexane, therefore, higher temperatures were used to perform the experiments. For n-hexane the investigation of several temperatures was not possible, as the intensity of the frequency response was already very low at a temperature of 30 °C. The unusual type of frequency response (Yasuda, 1994a) observed for n-hexane was also seen for mesitylene. That is, a kinetic process at high frequencies not directly visible anymore in the investigated frequency range had to be assumed in order to fit the experimental data. In Figure 6.7 and Table 6.3 the corresponding measurements and parameters used for the fitting are summarized. Again, very similar results between the parent and the crushed sample are obtained. The time constants are nearly the same within the experimental error range. A slight trend to shorter time constants can be seen in the crushed sample. The slow transport process is again dominating the whole transport, with a contribution of 70% to 90% depending on the temperature. It was found, that at 130 °C the fast process at high frequencies has a larger contribution compared to its contribution at 70 °C (see Table 6.3). In addition, for mesitylene, the out-of-phase function of the frequency response could not be fitted by an ideal diffusion model. In contrast to the results of n- hexane, a particle size distribution, or, mathematically equivalent, a distribution of the diffusivities within the sample had to

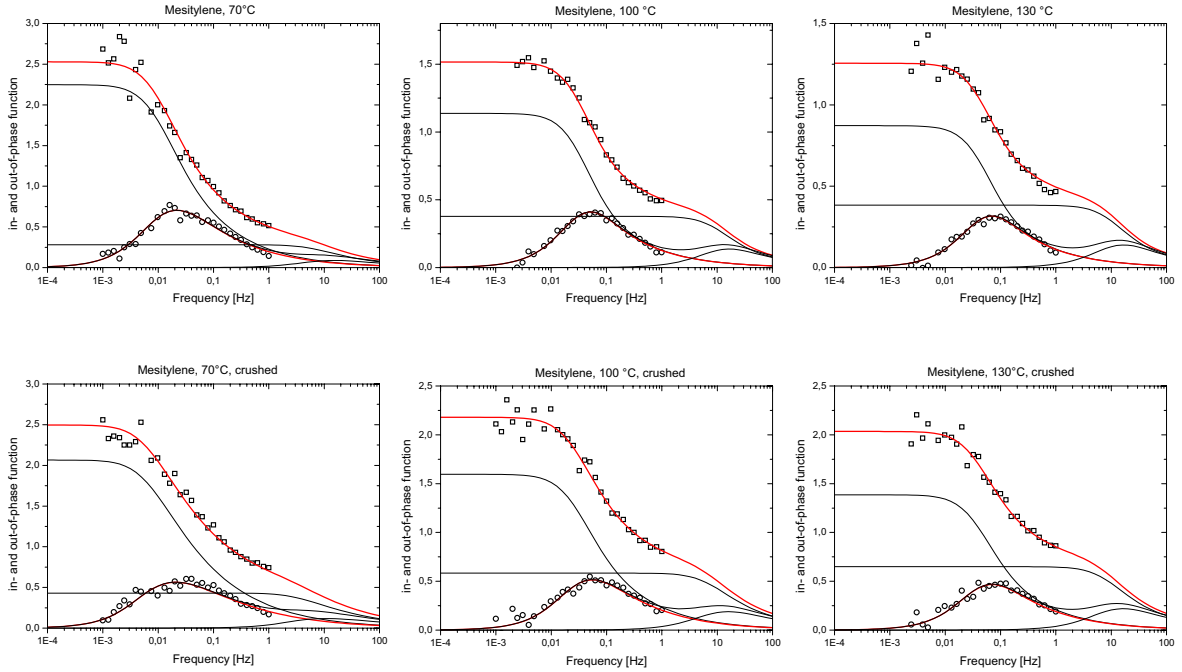

Figure 6.7: Frequency responces of mesitylene in (a) the parent, and (b) the crushed sample at 70, 100, and 130 °C.

be assumed. The variance σ of this distribution was found to be temperature-dependent as can be seen in Table 6.3.

The apparent activation energy of the slow transport process as obtained from the temperature depence of τ_1 in Table 6.3 was calculated to about 20 kJ/mol for the parent and about 16 kJ/mol for the crushed sample. The activation energy is lower for the crushed sample, mainly due to the difference in the time constants at 70 °C. It should however be noted, that the experimental frequency response of mesitylene in the crushed fiber sample shows a second peak, that may be related to an additional third kinetic process. Also presence of a distribution of the time constants and the fact that this distribution is temperature dependent leads to the conclusion that a third kinetic process at frequencies in the range of 10 to 100 Hz must be present for mesitylene. Therefore, the time constant may not accurately represent the correct time constant of the underlining process and, thus, the measured activation energies of the parent and crushed sample are not significantly different.

6.4 Discussion

Mesoporous fibers are hierarchically structured materials with a primary, secondary, and tertiary structure (Marlow et al., 2007). In order to understand and to quantify the diffusion in this system all three domains have to be considered. The primary structure is composed of the cylindrical mesopores and secondary micropores in framework as shown in Figure 6.8A. In this domain, the diffusion can be characterized by diffusion in the mesopore channels D_p and diffusion in micropores or larger cracks in the pore walls D_w. It is reasonable to assume that the diffusion in the mesopore channels is Knudsen diffusion influenced by the surface adsorption, i.e., surface diffusion (Ruthven et al., 2009). Such kind of system, where both surface diffusion and mesopore Knudsen diffusion exist can be represented by an effective diffusivity in the mesopores $D_\mathrm{eff,p}$ by embedding both surface diffusion and pore diffusion coefficient:

$$D_\mathrm{eff,p} = \frac{\epsilon_\mathrm{me} D_\mathrm{p} + (1-\epsilon_\mathrm{me}) K D_\mathrm{S}}{\tau \cdot [\epsilon_\mathrm{me} + (1-\epsilon_\mathrm{me}) K]} \tag{6.1}$$

where ϵ_me is the mesopore void fraction, and $(1-\epsilon_\mathrm{me})$ the adsorbed liquid. The products $\epsilon_\mathrm{me} D_\mathrm{p}$ and $(1-\epsilon_\mathrm{me}) K D_\mathrm{s}$ are the corresponding diffusion processes in the gas phase of the mesopores and in the adsorbed phase on the surface. K is the dimensionless Henry's constant based on particle volume. τ is the tortuosity of the mesopores. For MCM-41 materials, i.e., cylindrical pores, $\tau = 1.12$ was calculated by Salmas and Androutsopoulos (2001). The term $[\epsilon_\mathrm{me} + (1-\epsilon_\mathrm{me}) K]$ represents the capacity of the system to accommodate adsorbed molecules in both phases.

In the case of the diffusion in the mesopores it is reasonable to assume a Knudsen diffusion flow described by:

$$D_\mathrm{p} = D_\mathrm{K} = \frac{4}{3} \frac{r_\mathrm{p}}{2} \sqrt{\frac{8RT}{\pi M}} \tag{6.2}$$

where $r_\mathrm{p} = w_\mathrm{d}/2$ is the average radius of the mesopores, M the molar mass of the molecule, R the molar gas constant, and T the temperature. If micropores or cracks in the structure are present, the surface diffusion is identical to the intrawall diffusion in the adsorbed phase:

$$D_\mathrm{s} = D_\mathrm{w} \tag{6.3}$$

The second structural domain as shown in Figure 6.8B is composed of the primary cylindrical mesopores arranged in an ordered hexagonal pore array similar to the pore arrangement in MCM-41 materials. In this domain, the diffusion can be characterized by an effective diffusion parallel $D_{\mathrm{eff},\parallel}$ and perpendicular $D_{\mathrm{eff},\perp}$ to the mesopores. Assuming that the gas phase capacity in the pore is mush less than the adsorbed capacity

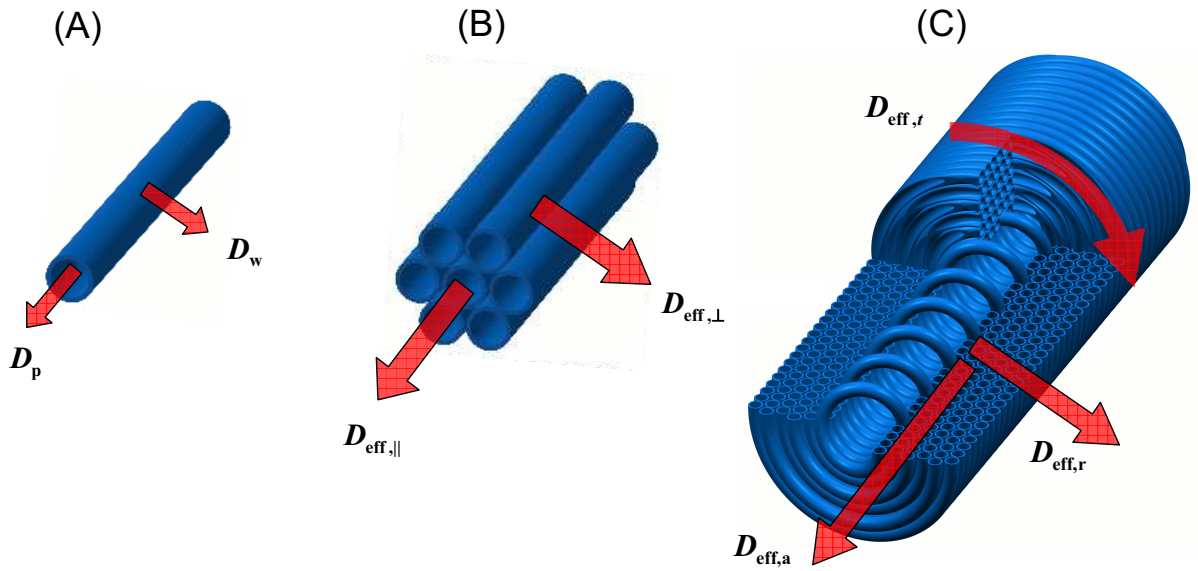

Figure 6.8: Schematic representation of the three structural domain present in mesoporous silica fibers. (A) corresponds to the primary structure, (B) to the secondary structure, and the representation (C) to the ternary structure. The primary structure is a single mesopore, the secondary structure corresponds to a hexagonal arrangement of these mesopores. In the ternary structure, these mesopore boundles form helical fibers. The possible diffusion pathways in each structural domain are indicated by arrows.

$\epsilon_{me} \ll (1-\epsilon_{me})K$, the effective diffusion coefficients are related to D_p and D_w by the following equations:

$$D_{eff,\parallel} = D_{eff,p} \tag{6.4}$$

$$\approx \frac{\epsilon_{me}}{K_H} \cdot \frac{D_K}{\tau} + \frac{D_w}{\tau} \tag{6.5}$$

$$D_{eff,\perp} = \frac{\left[\epsilon_{me} D_K^{-1} + (1-\epsilon_{me})\left(K D_w\right)^{-1}\right]^{-1}}{\tau\left[\epsilon_{me} + (1-\epsilon_{me})K\right]} \tag{6.6}$$

$$\approx \frac{D_w}{\tau} \tag{6.7}$$

where $K_H = \epsilon_{me} + (1-\epsilon_{me})K$ (Gobin et al., 2007a). Herein it was assumed for $D_{eff,\perp}$ that the intra-wall diffusion D_w is mush slower than D_K, leading to an effective diffusion perpendicular to the mesopores that is only determined by D_w.

The ternary structure of the fibers can be described by three new effective diffusivities according to Marlow et al. (2007): the tangential diffusion ($D_{eff,t}$), radial diffusion ($D_{eff,r}$), and axial diffusion direction ($D_{eff,a}$) as shown in Figure 6.8C. Thereby, only the radial

and the axial diffusivities are the ones, that are visible by macroscopic measurements, and, therefore, represent the two possible kinetic processes visible in the experimental frequency responses. The tangential diffusion is not visible by a macroscopic measurement technique, as in an ideal fiber no open mesopores in tangential direction are present as can be easily seen in Figure 6.8c. The diffusivities are related to the effective diffusivities $D_{\text{eff},\parallel}$ and $D_{\text{eff},\perp}$ by the following equations:

$$D_{\text{eff,t}} = D_{\text{eff},\parallel} \tag{6.8}$$

$$D_{\text{eff,r}} = D_{\text{eff},\perp} \tag{6.9}$$

$$D_{\text{eff,a}} \approx D_{\text{eff},\perp} + \frac{D_{\text{eff},\parallel}}{\tau_{\text{fiber}}} = D_{\text{eff},\perp} + \int_0^R \frac{L_{\text{fiber}}}{L_{\text{pore}}(r)} \mathrm{d}r \cdot D_{\text{eff},\parallel} \tag{6.10}$$

$$\tag{6.11}$$

where $L_{\text{pore}}(r)$ is the length of the primary mesopore as a function of the helix radius r. The macroscopic properties R and L_{fiber} are the (measurable) radius and length of the fiber. If the pitch (h) of the helix is known, the length of the primary mesopore can be obtained by geometrical calculations as a function of the fiber length L_{fiber} and of the helix radius:

$$L_{\text{pore}}(r) = 2\pi r \cdot \sqrt{1 + \left(\frac{h}{2\pi r}\right)^2} \cdot \frac{L_{\text{fiber}}}{h} \tag{6.12}$$

A schematic of orientation and dimensions of the helical pore orientation inside the fiber is shown in Figure 6.9. The tortuosity of the fiber is given by: $\tau_{\text{fiber}}(r) = L_{\text{pore}}(r)/L_{\text{fiber}}$. If a minimal pitch equal to the unit cell parameter a_0 is assumed ($h_{\min} = 4.30$ nm) the following maximal tortuosities are obtained: $\tau_{\text{fiber}} = 15$ for a helix radius very close to the center ($r = 1$ nm), and $\tau_{\text{fiber}} = 30000$ for a helix with a radius identical to the fiber radius (r = 20 μm). Larger pitches result in lower tortuosities, as for instance a pitch of 10 $h_{\min}$ gives $\tau_{\text{fiber}} = 5$ in the fiber center and $\tau_{\text{fiber}} = 3000$ at the edge of the fiber. As an important conclusion, the diffusion time constant in axial direction would strongly depend on the radius of the corresponding mesopore helix in the fiber, thus leading to a distribution of the diffusion time constant and to a convolution of multiple axial diffusion processes.

In order to understand the complex situation present in these fibers, the experimental results are compared in the following with the results of the quantitative evaluations of the diffusivities according to equations 6.1 to 6.12. Due to the fact that the surface area at the end of the fibers is a very small fraction of the total surface area of the fibers, a low contribution of the axial diffusion process is expected if diffusion in radial direction is possible. Several studies by Marlow and Stempniewicz (2006), Marlow et al. (2007), Stempniewicz et al. (2007) showed that the radial diffusion pathway is the dominant one.

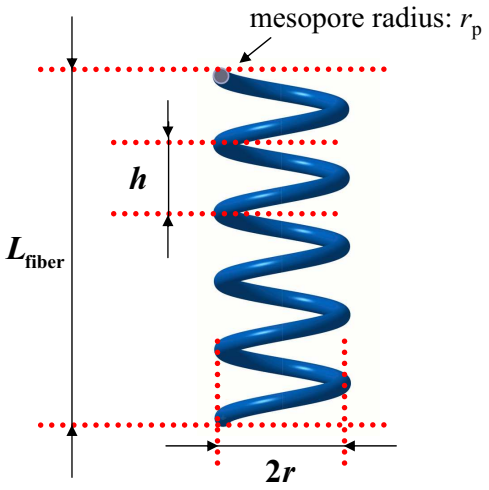

Figure 6.9: Schematic representation of an internal helical mesopore.

This was concluded based on several facts: first, modification of the outer surface leads to a distinct change in the uptake, second, the concentration gradient of Rhodamine 6G (Rh6G) followed by light microscopy showed no gradient at the fiber end but a continuous depletion was observed. However, these experiments do not unambiguously show that radial diffusion is possible, as these observations could also be explained by a strong surface barrier at the end of the fibers. Therefore, in this study, the average fiber length was shortened in order to analyze the diffusion as a function of the length of the fiber.

Sample	Compound	T (°C)	K_H (-)	D_K	$D_{eff,\perp}$ $D_{eff,r}$	$D_{eff,\parallel}$ $D_{eff,t}$	$D_{eff,a}^{c,h_1}$	$D_{eff,a}^{e,h_1}$	$D_{eff,a}^{c,h_2}$	$D_{eff,a}^{e,h_2}$
parent	mesitylene	70	101	17779	2.2	93	8.4	2.2	21	2.2
	mesitylene	100	32	18539	4.8	304	25	4.8	66	4.9
	mesitylene	130	10	19270	6.5	1009	74	6.5	208	6.8
	n-hexane	30	13	19734	7.5	790	60	7.5	166	7.8
crushed	mesitylene	70	101	17779	3.0	94	9.3	3.0	22	3.1
	mesitylene	100	32	18539	5.4	304	26	5.4	66	5.5
	mesitylene	130	10	19270	6.7	1009	74	6.7	209	7.0
	n-hexane	30	13	19734	7.9	790	61	7.9	166	8.1

Table 6.4: Calculated effective diffusivities in the fiber samples for n- hexane and mesitylene. The effective diffusivities in axial direction are given in the core 'c' or at the edge 'e' of the fiber calculated for a pitch of $h_1 = 4.30$ nm and $h_2 = 43$ nm. The units of all the diffusivities are 10^{-12} m^2/s.

If the axial diffusion pathway is significant, the diffusion time constants should differ

by more than one order of magnitude. However, such a dependence was not observed, as the main diffusion process was found to be independent of the fiber length. This confirms the assumption that the dominant transport process is the radial effective diffusion. In Table 6.4 the calculated effective diffusivities for n-hexane and mesitylene are given. Based on these facts, for the calculations, the radial diffusion process was associated to the experimentally obtained τ_1 (see Table 6.2 and 6.3), as the process given by τ_1 is the dominating transport process, which that is observed in the frequency response experiments. According to equation 6.6, this diffusivity is identical to the intrawall diffusion.

From the results in Table 6.4 some interesting conclusions can be drawn. The effective tangential diffusivity in the mesopores ($D_{\text{eff},\parallel}$) as given in equation 6.4 is strongly dependent on the temperature and may differ by several orders of magnitude compared to the Knudsen diffusion. This is the case, as the effective diffusion in this mesoporous material is strongly lowered by the adsorption capacity as described by the Henry law. A similar situation was also recently found for the diffusion in large pore SBA-15 and SBA-16 materials (Gobin et al., 2007a,b, Hoang et al., 2005).

Interestingly the activation energy of nearly 46 kJ/mol of the effective diffusion in mesopores $D_{\text{eff},\parallel}$ is much larger than the one experimentally observed for the main diffusion process in the mesopores (15 to 20 kJ/mol) as reported in Table 6.5. This is another clear indication, that the main diffusion process is not determined by the diffusion in the mesopore channels of the fiber material. The effective diffusion in the mesopores, i.e., the tangential effective diffusion $D_{\text{eff},\parallel} = D_{\text{eff,t}}$ is, however, only theoretically relevant, as this diffusivity can not be observed by a macroscopic technique.

E_{A}(exp)	$E_{\text{A}}(D_{\text{K}})$	H_{ads}	$E_{\text{A},\parallel}$ $E_{\text{A,t}}$	$E_{\text{A},\perp}$ $E_{\text{A,r}}$	$E_{\text{A,a}}$(c,h_1)	$E_{\text{A,a}}$(e,h_1)	$E_{\text{A,a}}$(c,h_2)	$E_{\text{A,a}}$(e,h_2)
21.0	1.5	44.4	45.6	21.0	41.6	21.0	44.1	21.6

Table 6.5: Activation energies of the diffusivities present in the fibers, and the heat of adsorption of mesitylene in the parent sample. All values are given in kJ/mol. Nomenclature is identical to the one given in Table 6.4.

The other relevant diffusion process is the effective axial diffusion $D_{\text{eff,a}}$ as given in equation 6.10. As can be easily seen, this diffusivity is influenced by both effective diffusivities perpendicular to the main mesopore channels, i.e., the intrawall diffusion, and by the effective diffusion in the mesopores itself divided by the tortuosity of the mesopores in the fiber. A value of $D_{\text{eff,a}}$ close to $D_{\text{eff,r}}$ signifies that also the axial process is determined by the intrawall diffusity and not by the diffusion in the mesopore channels.

In Table 6.4 several effective axial diffusivities are given for mesopores located in the center of the fiber ('c') and at the edge ('e') for a pitch of the mesopore helix of $h_1 = 4.30$ nm and $h_2 = 43$ nm. It can be easily seen, that the effective axial diffusivities obtained for mesopores located at the edge of the fibers are entirely determined by $D_{\text{eff},\perp}$, i.e., by the intrawall diffusion. This is also confirmed by the analysis of the activation energies reported in Table 6.5. The activation energies of the effective axial diffusion in the center ($E_{\text{A,a}}(c) = 42$ to 44 kJ/mol) approaches the one of the effective tangential diffusion ($E_{\text{A,t}}$ = 45.6 kJ/mol), whereas the activation energy of the effective axial diffusion at the edge ($E_{\text{A,a}}(e) = 21$ to 22 kJ/mol) approaches the one of the radial diffusion ($E_{\text{A,r}}$ = 21 kJ/mol). This finding is remarkable, as it clearly shows that even in the axial fiber direction the diffusion is to a large extent given by the intrawall transport and not by the primary mesopore structure. Only the helical mesopores located in or close to the fiber center show an effective axial diffusion that is faster than the radial diffusion.

The findings reported herein in combination with the results from Marlow et al. (2007) strongly suggest that perpendicular connections between the mesopore channels are present, leading to a radial transport in the fibers. The exact type of these connections is, however, still unclear. Interestingly, the analysis of the N_2-physisorption isotherm indicates no pore population in the micropore range below 2 nm. This can be explained by the fact that the thickness of the mesopore walls is only ∼0.85 nm as obtained by the DFT analysis of the nitrogen isotherm. Compared to the wall thickness of SBA-15 or 16 materials (Gobin et al., 2007b) the thickness is around four times smaller depending on the synthesis conditions. It is, therefore, possible, that the intrawall pores in the fibers are simply not visible in the nitrogen physisorption isotherm. This situation is similar to the one in ITQ-2, where the experimental micropore volume is lower than the theoretical one, due to the fact, that the micropores are accessible by larger pores and therefore only act as pockets (Corma et al., 2000). The minimum size of the micropores must be larger than the critical diameter of mesitylene, i.e., 8.4 nm (Satterfield and Cheng, 1972), as both hexane and mesitylene show a radial transport as discussed previously. As an additional confirmation of the presence of intrawall pores, recent studies showed that it is possible to obtain stable carbon replicas of the fibers (Chen et al., 2004).

By macroscopic techniques, such as the frequency response methods, the diffusivity is not directly measured. In principle, it is always the diffusional time constant L^2/D that is observed. In order to assign all the peaks in the experimental frequency response it is therefore necessary to transfer the calculated diffusivities into diffusional time constants L^2/D by knowledge of the corresponding characteristic length of the diffusion pathway. In the case of the radial effective diffusion the half-diameter, i.e., $L_{\text{radial}} = 12.5$ μm, is the characteristic length for both fiber samples. The half-length of the fiber or the

Sample	Compound	T °C	τ_{radial} s	τ_{axial}(c,h_1) s	τ_{axial}(e,h_1) s	τ_{axial}(c,h_2) s	τ_{axial}(e,h_2) s
parent	mesitylene	70	20.9	374.0	2994.7	135.9	2903.2
	mesitylene	100	71.2	2681.9	10244.9	1082.6	10116.4
	mesitylene	130	32.4	898.1	4658.7	343.4	4572.5
	n-hexane	30	24.1	305.1	3458.4	108.0	3304.6
crushed	mesitylene	70	19.9	10.3	79.4	3.8	77.1
	mesitylene	100	51.6	67.4	206.4	28.7	204.5
	mesitylene	130	28.9	24.3	115.2	9.4	113.3
	n-hexane	30	23.3	8.4	92.8	3.0	88.8

Table 6.6: Time constants L^2/D of the radial and axial diffusion processes. For the radial process τ_{radial} a characteristic length of $L_{\text{radial}} = 12.5$ μm, i.e. the average half diameter of the fibers, for both parent and crushed sample is assumed. For the axial processes τ_{axial} a characteristic length of $L_{\text{axial,parent}} = 150$ μm, and $L_{\text{axial,crushed}} = 25$ μm are used for the parent and crushed fiber sample respectively. The corresponding diffusivities D are reported in Table 6.4. Nomenclature is identical to the one given in Table 6.4.

characteristic length of the axial diffusion process is $L_{\text{axial,parent}} = 150$ μm for the parent, and $L_{\text{axial,crushed}} = 25$ μm for the crushed sample. The time constant briefly indicates the frequency in the experimental frequency response where the maximum of the out-of-phase characteristic function is expected. The results are given in Table 6.6 and clearly show that for the parent fiber sample in all cases the time constants of the axial diffusion processes are larger than the one of the radial processes, and thus, the axial diffusion is not the dominant transport mechanism. For the crushed fiber sample this situation is different. In this case, the time constants of the axial diffusion processes in the center of the fiber can be lower, that is, a faster transport, than the one of the radial processes. This, however, is only valid for the helical mesopores close to the center of the fiber. At the edge, the radial transport once again becomes faster than the axial.

After quantification of the diffusivities present in the fibers, it is possible to explain the different processes visible in the experimental frequency response data as given in Table 6.3. Experimentally, three diffusion processes are present: two diffusion processes at frequencies in between 0.1 to 0.01 Hz and a fast process at frequencies higher than 1 Hz. The dominant transport process has to be composed of two processes, as it shows a relatively broad frequency response that is temperature dependent. This can not be explained by a simple distribution of the fiber dimensions. Due to the temperature

dependence of the distribution it has to be related to a distribution of diffusivities. This result is consistent with the finding obtained by the preceding calculations. A second process, the effective axial diffusion, overlaps with the effective radial diffusion in the fibers and leads to a broadening which is dependent of the temperature. This distribution is more pronounced for the crushed fiber due to the shorter diffusion pathway, that shifts the time constant to a frequency region which is overlapping with the one of the radial diffusion process. The third process located at frequencies higher than 1 Hz is difficult to understand. In the uptake rate analysis done by Stempniewicz et al. (2007) also such kind of fast process was observed. Obviously this fast process is related to a structural feature of the fibers or to a feature that is due to the synthesis method. Stempniewicz et al. (2007) related the fast process to cracks in the fibers and not to a diffusion process in the mesopores.

In order to contribute to a fast diffusion process in these cracks, a certain fraction of molecules would have to be adsorbed in these cracks. From the frequency response measurements a contribution of ∼20% was observed, thus this amount of molecules would have to be adsorbed in these cracks in order to contribute to the fast transport process. This situation seems very unlikely, as this pore fraction, that must be larger than the framework mesopores, is not seen in the N_2-physisorption isotherm. However, assuming that cracks are indeed the reason for the very fast transport process, the following situation would be present: due to the cracks in the fibers, the characteristic length of the axial diffusion pathway would be significantly reduced and the contribution of the diffusion in the mesopores would be more important to the overall diffusion. This would lead to an activation energy of the observed transport process, that is close to the one of $D_{\mathrm{eff},\parallel}$ (45 kJ/mol). In the frequency response experiments, however, an activation energy of ∼20 kJ/mol was observed, confirming the fact that cracks in the fibers are not the reason for the fast transport process.

Two types of shapes grow during the synthesis at the phase boundary: fibers and small rotational symmetrical particles. Both have the same primary and secondary structure. They only differ in the ternary structure. These particles are rather small, with diameters similar to the diameter of the fibers. In these particles, the effective diffusion in the mesopores would have time constants below 1 s and, thus, be located in the frequency response at frequencies above 1 Hz. Therefore, it seems reasonable to assume, that this second population of particles may be the reason for the fast transport process. Also a weight fraction of 10% to 20% of the rotational symmetrical particles relative to the fiber fraction is reasonable as can be seen in SEM images. However, the temperature dependence of the relative contribution of the processes can not be explained by this model. As can be seen in Table 6.3, the relative contribution of the fast process

is nearly 30% at 130 °C of mesitylene, whereas it decreases to a contribution of ∼10% at 70 °C. As the adsorption properties of the small rotational symmetrical particles and of the fibers are identical, this leads to the conclusion, that the small particles can not be the only explanation for the fast transport process.

In Table 6.4 diffusivities of the effective tangential diffusion are given. This diffusivity is in principle identical to the effective diffusion in the mesopores. As this process is more than one order of magnitude faster than all other present in the fibers, it is a potential candidate for the very fast process experimentally observed. It was, however, stated that this diffusion pathway can not be observed by a macroscopic method, as in an ideal fiber, no open mesopore in tangential direction exists. Assuming that indeed cracks or more precisely open mesopore walls at the edge of the fiber are present in the fibers, this transport pathway would be possible and would lead to such a fast and also temperature dependent transport process. In conclusion the fast process is attributed to the effective tangential diffusion in the fibers in addition to a certain fraction of fast desorbing rotational particles present in the samples.

6.5 Conclusions

Circularly ordered mesoporous silica fibers are complex, hierarchical materials with very interesting transport properties. All three structural domains present in the fibers have to be considered in order to quantitatively understand the different diffusion pathways. The diffusion in radial direction is the dominant transport process. It is related to intrawall pores present in the framework walls. Diffusion in axial direction is also a potential transport pathway. Interestingly, this diffusion is essentially also governed by the intrawall diffusion and not by diffusion in the mesopores. This is due to the helical internal structure of the fibers that leads to high tortuosities of up to 104 at the edge of the fiber in the axial direction. In the fiber center, transport in axial direction is caused by diffusion in the mesopore channels. In addition to these two transport pathways, it was found, that also diffusion in tangential direction in the mesopores is present. The process is very fast and is due to non-idealities of the fiber structure, leading to mesopore openings at the edge of the fiber.

7 Conclusions

The transport of molecules in porous materials can be considered as a highly complex dynamic system. In this thesis, by application of the frequency response technique in addition to several other experimental techniques, a detailed understanding of the transport mechanisms present in several porous systems was obtained.

The intracystalline diffusion in MFI type materials, e.g., H-ZSM-5, is highly confined due to the MFI pores and, thus, strongly depends on the molecular dimensions of the molecule. Diffusion is isotropic in MFI for small molecules, however, in contrast, for bulkier molecules, the diffusion can be anisotropic. This is due to the complex pore structure of MFI, that is composed of two interconnected channel systems with different diffusivities. If the channel switching rate of the molecule is low, an anisotropic diffusion is observed (see chapter 3).

Intracrytalline diffusion properties of porous solids are highly important, however, for practical application, always the complete transport from the gas phase to the porous particle or crystal has to be considered. If the particles are small or the intracrystalline diffusion process fast, the transport is given by surface properties and not any more by the bulk properties of the particles (see chapter 4). Surface effects dominate and can lead to a selective enhancement or decrease of the transport. Thus, by tailoring the surface properties, for instance by deposition of reactive molecules, it is possible to selectively modify the overall transport properties of the porous solid (see chapter 5).

Often porous solids are not only compored of a uniform population of pores, but rather of complex hierarchical structures. In each structural domain, diffusion and transport properties may change. In such kind of complex material, the transport is a composite of all effects induced by each structural domain, and thus, for a complete description of the kinetic properties, characterization of the transport in each domain is essesary (see chapter 6).

Bibliography

P. Alexandridis and T. A. Hatton. Poly(ethylene oxide)-poly(propylene oxide)-poly (ethylene oxide) block copolymer surfactants in aqueous solutions and at interfaces: thermodynamics, structure, dynamics, and modeling. *Colloids and Surfaces A: Physicochem. Eng. Aspects*, 96:1–46, 1995.

H. M. Alsyouri and J. Y. S. Lin. Gas diffusion and microstructural properties of ordered mesoporous silica fibers. *Journal of Physical Chemistry B*, 109(28):13623–13629, 2005.

H. M. Alsyouri and Y. S. Lin. Effects of synthesis conditions on macroscopic and microscopic properties of ordered mesoporous silica fibers. *Chemistry Of Materials*, 15 (10):2033–2039, 2003.

C. Baerlocher and L.B. McCusker. Database of zeolite structures: http://www.iza-structure.org/databases/.

C. Baerlocher, W.M. Meier, and D.H. Olson. *Atlas of Zeolite Framework Types*. 5 edition, 2001.

J Banhart. Manufacture, characterisation and application of cellular metals and metal foams. *Progress in Materials Science*, 46(6):559–U3, 2001.

E.P. Barrett, L.G. Joyner, and P.P. Halenda. The Determination of Pore Volume and Area Distributions in Porous Substances. I. Computations from Nitrogen Isotherms. *Journal of the American Chemical Society*, 73:373–380, 1951.

D Barthomeuf. Basic zeolites: Characterization and uses in adsorption and catalysis. *Catalysis Reviews Science and Engineering*, 38(4):521–612, 1996.

J. S. Beck, J. C. Vartuli, W. J. Roth, M. E. Leonowicz, C. T. Kresge, K. D. Schmitt, C. T. W. Chu, D. H. Olson, E. W. Sheppard, S. B. McCullen, J. B. Higgins, and J. L. Schlenker. A New Family of Mesoporous Molecular-Sieves Prepared with Liquid-Crystal Templates. *Journal of the American Chemical Society*, 114(27):10834–10843, 1992.

References

G. C. Bond, M. A. Keane, H. Kral, and J. A. Lercher. Compensation phenomena in heterogeneous catalysis: General principles and a possible explanation. *Catalysis Reviews - Science and Engineering*, 42(3):323–383, 2000.

L. Boulicaut, S. Brandani, and D. M. Ruthven. Liquid phase sorption and diffusion of branched and cyclic hydrocarbons in silicalite. *Microporous and Mesoporous Materials*, 25(1-3):81–93, 1998.

S. Brandani and D. M. Ruthven. Analysis of ZLC Desorption Curves for Liquid-Systems. *Chemical Engineering Science*, 50(13):2055–2059, 1995.

S. Brandani and D. M. Ruthven. Moments analysis of the zero length column method. *Industrial and Engineering Chemistry Research*, 35(1):315–319, 1996.

S. Brandani, C. Cavalcante, A. Guimaraes, and D. Ruthven. Heat effects in ZLC experiments. *Adsorption*, 4(3-4):275–285, 1998.

S. Brandani, M. Jama, and D. Ruthven. Diffusion, self-diffusion and counter-diffusion of benzene and p-xylene in silicalite. *Microporous and Mesoporous Materials*, 35-6: 283–300, 2000a.

S. Brandani, M. A. Jama, and D. M. Ruthven. ZLC Measurements under non-linear conditions. *Chemical Engineering Science*, 55(7):1205–1212, 2000b.

J Caro, M Noack, P Kolsch, and R Schafer. Zeolite membranes - state of their development and perspective. *Microporous and Mesoporous Materials*, 38(1):3–24, JUL 2000.

C. L. Cavalcante and D. M. Ruthven. Adsorption of Branched and Cyclic Paraffins In Silicalite: 1. Equilibrium. *Industrial and Engineering Chemistry Research*, 34(1): 177–184, 1995.

C. L. Cavalcante, S. Brandani, and D. M. Ruthven. Evaluation of the main diffusion path in zeolites from ZLC desorption curves. *Zeolites*, 18(4):282–285, 1997.

F. X. Chen, X. J. Xu, S. C. Shen, S. Kawi, and K. Hidajat. Microporosity of SBA-3 mesoporous molecular sieves. *Microporous and Mesoporous Materials*, 75(3):231–235, 2004.

C. Chmelik, A. Varmla, L. Heinke, D. B. Shah, J. Karger, F. Kremer, U. Wilczok, and W. Schmidt. Effect of surface modification on uptake rates of isobutane in MFI crystals: An infrared Microscopy study. *Chemistry of Materials*, 19(24):6012–6019, 2007.

References

V. R. Choudhary, V. S. Nayak, and T. V. Choudhary. Single-component sorption/diffusion of cyclic compounds from their bulk liquid phase in H-ZSM-5 zeolite. *Industrial and Engineering Chemistry Research*, 36(5):1812–1818, 1997.

U. Ciesla and F. Schüth. Ordered mesoporous materials. *Microporous and Mesoporous Materials*, 27(2-3):131–149, 1999.

A. Corma. Inorganic Solid Acids And Their Use In Acid-Catalyzed Hydrocarbon Reactions. *Chemical Reviews*, 95(3):559–614, 1995.

A. Corma, V. Fornes, J. M. Guil, S. Pergher, T. L. M. Maesen, and J. G. Buglass. Preparation, characterisation and catalytic activity of ITQ-2, a delaminated zeolite. *Microporous and Mesoporous Materials*, 38(2-3):301–309, 2000.

J. Crank. *The Mathematics of Diffusion*. Oxford University Press, 1979.

M. E. Davis. Ordered porous materials for emerging applications. *Nature*, 417(6891): 813–821, 2002.

J. F. Denayer, G. V. Baron, J. A. Martens, and P. A. Jacobs. Chromatographic study of adsorption of n-alkanes on zeolites at high temperatures. *Journal of Physical Chemistry B*, 102(17):3077–3081, 1998.

E. G. Derouane and Z. Gabelica. A Novel Effect of Shape Selectivity - Molecular Traffic Control In Zeolite ZSM-5. *Journal of Catalysis*, 65(2):486–489, 1980.

W. L. Duncan and K. P. Möller. A 'zero length' criterion for ZLC chromatography. *Chemical Engineering Science*, 55:5415–5420, 2000.

W. L. Duncan and K. P. Möller. The effect of a crystall siye distribution on ZLC experiments. *Chemical Engineering Science*, 57:2641 – 2652, 2002.

F. Eder and J. A. Lercher. On the role of the pore size and tortuosity for sorption of alkanes in molecular sieves. *Journal of Physical Chemistry B*, 101(8):1273–1278, 1997.

F. Eder, M. Stockenhuber, and J. A. Lercher. Brønsted acid site and pore controlled siting of alkane sorption in acidic molecular sieves. *Journal of Physical Chemistry B*, 101(27):5414–5419, 1997.

J.-P. Gilson and M. Guisnet. *Zeolites for Cleaner Technologies*. Imperial College, 2002.

O. C. Gobin, Q. L. Huang, H. Vinh-Thang, F. Kleitz, M. Eic, and S. Kaliaguine. Mesostructured silica SBA-16 with tailored intrawall porosity part 2: Diffusion. *Journal of Physical Chemistry C*, 111(7):3059–3065, 2007a.

References

O. C. Gobin, Y. Wan, D. Y. Zhao, F. Kleitz, and S. Kaliaguine. Mesostructured silica SBA-16 with tailored intrawall porosity part 1: Synthesis and characterization. *Journal of Physical Chemistry C*, 111(7):3053–3058, 2007b.

O. C. Gobin, S. J. Reitmeier, A. Jentys, and J. A. Lercher. Comparison of the Transport of Aromatic Compounds in Small and Large MFI Particles. *Journal of Physical Chemistry C*, 113(47):20435–20444, 2009a.

O. C. Gobin, S. J. Reitmeier, A. Jentys, and J. A. Lercher. Diffusion pathways of benzene, toluene and p-xylene in MFI. *Microporous and Mesoporous Materials*, 125(1-2):3–10, 2009b.

S. J. Gregg and Sing K. S. W. *Adsorption Surface Area and Porosity.* Academic Press Inc.,U.S., 2nd edition, 1982.

Y. J. Han, J. T. Watson, G. D. Stucky, and A. Butler. Catalytic activity of mesoporous silicate-immobilized chloroperoxidase. *Journal of Molecular Catalysis B - Enzymatic*, 17(1):1–8, 2002.

N. Hansen. The CMA evolution strategy: a comparing review. In J.A. Lozano, P. Larranaga, I. Inza, and E. Bengoetxea, editors, *Towards a new evolutionary computation. Advances on estimation of distribution algorithms*, pages 75–102. Springer, 2006.

V. T. Hoang, Q. L. Huang, M. Eic, T. O. Do, and S. Kaliaguine. Structure and diffusion characterization of SBA-15 materials. *Langmuir*, 21(5):2051–2057, 2005.

M. Jaroniec, M. Kruk, and A. Sayari. Adsorption methods for characterization of surface and structural properties of mesoporous molecular sieves. In *Mesoporous Molecular Sieves 1998*, volume 117 of *Studies in Surface Science and Catalysis*, pages 325–332. Elsevier Science Publ B V, Amsterdam, 1998.

M. Jaroniec, M. Kruk, and J. P. Olivier. Standard nitrogen adsorption data for characterization of nanoporous silicas. *Langmuir*, 15(16):5410–5413, 1999.

M. Jaroniec, J. Choma, and M. Kruk. On the applicability of the Horwath-Kawazoe method for pore size analysis of MCM-41 and related mesoporous materials. In *Characterization of Porous Solids V*, volume 128 of *Studies in Surface Science and Catalysis*, pages 225–234. Elsevier Science Bv, Amsterdam, 2000.

A. Jentys, H. Tanaka, and J. A. Lercher. Surface processes during sorption of aromatic molecules on medium pore zeolites. *Journal of Physical Chemistry B*, 109(6):2254–2261, 2005.

References

A. Jentys, R. R. Mukti, and J. A. Lercher. On the sticking probability of aromatic molecules on zeolites. Comment on "Sticking Probability on Zeolites". *Journal of Physical Chemistry B*, 110(35):17691–17693, 2006.

A. Jentys, R. R. Mukti, J. A. Lercher, Zi G. J. C. Ruren X., and Wenfu Y. The Energetic and Entropic Contributions Controlling the Orientation of Alkyl Substituted Aromatic Molecules in the Pores of MFI Zeolites. In *Studies in Surface Science and Catalysis*, volume Volume 170, Part 1, page 926. Elsevier, 2007.

M. Jiang and M. Eic. Transport Properties of Ethane, Butane and Their Binary Mixtures in MFI-Type Zeolite and Zeolite-Membrane Systems. *Adsorption*, 9:225–234, 2003.

H. Jobic, M. Bee, and S. Pouget. Diffusion of benzene in ZSM-5 measured by the neutron spin-echo technique. *Journal of Physical Chemistry B*, 104(30):7130–7133, 2000.

R. G. Jordi and D. D. Do. Analysis of The Frequency-Response Method For Sorption Kinetics In Bidispersed Structured Sorbents. *Chemical Engineering Science*, 48(6): 1103–1130, 1993.

J. Kärger. Measurement of diffusion in zeolites - A never ending challenge? *Adsorption*, 9(1):29–35, 2003.

J. Kärger and D. M. Ruthven. Diffusion and adsorption in porous solids. *Handbook of Porous Solids*, 4:2089, 2002.

J. Kärger and D.M. Ruthven. On the comparision between macroscopic and NMR measurements of intracrystalline diffusion in zeolites. *Zeolites*, 9(4):267–281, 1989.

J. Kärger, H. Pfeifer, T. Wutscherk, S. Ernst, J. Weitkamp, and J. Fraissard. Direct observation of intracrystalline transport diffusion in zeolites by Xe-129 NMR. *Journal of Physical Chemistry*, 96(12):5059–5063, 1992.

J. M. Kim, J. H. Kwak, S. Jun, and R. Ryoo. Ion-Exchange and Thermal-Stability of MCM-41. *Journal of Physical Chemistry*, 99(45):16742–16747, 1995.

C. E. A. Kirschhock, E. J. P. Feijen, P. A. Jacobs, and J. A. Martens. Hydrothermal zeolite synthesis. In G. Ertl, H. Knözinger, F. Schüth, and J. Weitkamp, editors, *Handbook of Heterogeneous Catalysis*, chapter 2.3.5, pages 160–178. Wiley-VCH, 2008.

F. Kleitz, F. Marlow, G. D. Stucky, and F. Schüth. Mesoporous silica fibers: Synthesis, internal structure, and growth kinetics. *Chemistry of Materials*, 13(10):3587–3595, 2001.

E. Klemm and G. Emig. A method for the determination of diffusion coefficients in product-shape-selective catalysis on zeolites under reaction conditions. *Chemical Engineering Science*, 52(23):4329–4344, 1997.

G. Kokotailo, S. Lawton, D. Olson, and W. Meier. Structure of Synthetic Zeolite ZSM-5. *Nature*, 272:437 – 438, 1978.

P. Kortunov, S. Vasenkov, C. Chmelik, J. Karger, D. M. Ruthven, and J. Wloch. Influence of defects on the external crystal surface on molecular uptake into MFI-type zeolites. *Chemistry of Materials*, 16(18):3552–3558, 2004.

C. T. Kresge, M. E. Leonowicz, W. J. Roth, J. C. Vartuli, and J. S. Beck. Ordered Mesoporous Molecular-Sieves Synthesized by a Liquid-Crystal Template Mechanism. *Nature*, 359(6397):710–712, 1992.

R. Krishna. Describing the Diffusion of Guest Molecules Inside Porous Structures. *Journal of Physical Chemistry C*, 113(46):19756–19781, 2009.

R. Krishna and J. M. van Baten. Unified Maxwell-Stefan description of binary mixture diffusion in micro- and meso-porous materials. *Chemical Engineering Science*, 64(13): 3159–3178, 2009.

R Krishna and JA Wesselingh. Review article number 50 - The Maxwell-Stefan approach to mass transfer. *Chemical Engineering Science*, 52(6):861–911, 1997.

M. Kruk and M. Jaroniec. Gas adsorption characterization of ordered organic-inorganic nanocomposite materials. *Chemistry of Materials*, 13(10):3169–3183, 2001.

M. Kruk, M. Jaroniec, and A. Sayari. Application of large pore MCM-41 molecular sieves to improve pore size analysis using nitrogen adsorption measurements. *Langmuir*, 13 (23):6267–6273, 1997.

M. Kruk, M. Jaroniec, and J. Choma. Comparative analysis of simple and advanced sorption methods for assessment of microporosity in activated carbons. *Carbon*, 36 (10):1447–1458, 1998.

M. Kruk, V. Antochshuk, M. Jaroniec, and A. Sayari. New approach to evaluate pore size distributions and surface areas for hydrophobic mesoporous solids. *Journal of Physical Chemistry B*, 103(48):10670–10678, 1999.

M. Kruk, M. Jaroniec, Y. Sakamoto, O. Terasaki, R. Ryoo, and C. H. Ko. Determination of pore size and pore wall structure of MCM-41 by using nitrogen adsorption, transmission electron microscopy, and X-ray diffraction. *Journal of Physical Chemistry B*, 104(2): 292–301, 2000.

References

R Lakes. Materials with structural hierarchy. *Nature*, 361(6412):511–515, 1993.

M. H. Lim and A. Stein. Comparative studies of grafting and direct syntheses of inorganic-organic hybrid mesoporous materials. *Chemistry of Materials*, 11(11):3285–3295, 1999.

Y. S. Lin and H. Alsyouri. Reply to "Comment on 'Gas diffusion and microstructural properties of ordered mesoporous silica fibers'". *Journal of Physical Chemistry B*, 110 (23):11606–11606, 2006.

M Linden, S Schacht, F Schüth, A Steel, and KK Unger. Recent advances in nano- and macroscale control of hexagonal, mesoporous materials. *Journal of Porous Materials*, 5(3-4):177–193, 1998.

Z. Q. Liu, M. F. Ottaviani, L. Abrams, X. G. Lei, and N. J. Turro. Characterization of the external surface of silicalites employing electron paramagnetic resonance. *Journal of Physical Chemistry A*, 108(39):8040–8047, 2004.

W. W. Lukens, P. Schmidt-Winkel, D. Y. Zhao, J. L. Feng, and G. D. Stucky. Evaluating pore sizes in mesoporous materials: A simplified standard adsorption method and a simplified Broekhoff-de Boer method. *Langmuir*, 15(16):5403–5409, 1999.

F. Marlow and M. Stempniewicz. Comment on "Gas diffusion and microstructural properties of ordered mesoporous silica fibers". *Journal of Physical Chemistry B*, 110 (23):11604–11605, 2006.

F. Marlow, B. Spliethoff, B. Tesche, and D. Y. Zhao. The internal architecture of mesoporous silica fibers. *Advanced Materials*, 12(13):961–+, 2000.

F. Marlow, F. Kleitz, U. Wilczok, W. Schmidt, and I. Leike. Texture effects of circularly ordered fibers. *ChemPhysChem*, 6(7):1269–1275, 2005.

F. Marlow, A. S. G. Khalil, and M. Stempniewicz. Circular mesostructures: solids with novel symmetry properties. *Journal of Materials Chemistry*, 17(21):2168–2182, 2007.

T. Maschmeyer, F. Rey, G. Sankar, and J. M. Thomas. Heterogeneous Catalysts Obtained by Grafting Metallocene Complexes onto Mesoporous Silica. *Nature*, 378(6553):159–162, 1995.

G. Mirth, J. Cejka, and J. A. Lercher. Transport And Isomerization of Xylenes Over H-ZSM-5 Zeolites. *Journal of Catalysis*, 139(1):24–33, 1993.

K. Moller and T. Bein. Inclusion chemistry in periodic mesoporous hosts. *Chemistry of Materials*, 10(10):2950–2963, 1998.

References

R. R. Mukti, A. Jentys, and J. A. Lercher. Orientation of alkyl-substituted aromatic molecules during sorption in the pores of ZSM-5 zeolites. *Journal of Physical Chemistry C*, 111(10):3973–3980, 2007.

G. Muller, T. Narbeshuber, G. Mirth, and J. A. Lercher. Infrared Microscopic Study of Sorption and Diffusion of Toluene In ZSM-5. *Journal of Physical Chemistry*, 98(31): 7436–7439, 1994.

L. M. Naphtali and L. M. Polinski. A Novel Technique for Characterization of Adsorption Rates on Heterogeneous Surfaces. *Journal of Physical Chemistry*, 67(2):369–&, 1963.

A. V. Neimark and P. I. Ravikovitch. Density functional theory of adsorption hysteresis and nanopore characterization. In *Characterization of Porous Solids V*, volume 128 of *Studies in Surface Science and Catalysis*, pages 51–60. Elsevier Science Bv, Amsterdam, 2000.

A. V. Neimark, P. I. Ravikovitch, M. Grun, F. Schuth, and K. K. Unger. Pore size analysis of MCM-41 type adsorbents by means of nitrogen and argon adsorption. *Journal of Colloid and Interface Science*, 207(1):159–169, 1998a.

A.V. Neimark, K. S. W. Sing, and Thommes M. Characterization of Solid Catalysts. In G Ertl, H. Knözinger, F. Schüth, and Weitkamp J., editors, *Handbook of Heterogeneous Catalysis*, chapter 3.1.1, pages 721–737. Wiley VCH GmbH, 1998b.

D. H. Olson, G. T. Kokotailo, S. L. Lawton, and W. M. Meier. Crystal-Structure and Structure Related Properties Of ZSM-5. *Journal of Physical Chemistry*, 85(15): 2238–2243, 1981.

D. Paschek and R. Krishna. Inter-relation between self- and jump-diffusivities in zeolites. *Chemical Physics Letters*, 333(3-4):278–284, 2001.

P. I. Ravikovitch and A. V. Neimark. Experimental confirmation of different mechanisms of evaporation from ink-bottle type pores: Equilibrium, pore blocking, and cavitation. *Langmuir*, 18(25):9830–9837, 2002.

P. I. Ravikovitch, D. Wei, W. T. Chueh, G. L. Haller, and A. V. Neimark. Evaluation of pore structure parameters of MCM-41 catalyst supports and catalysts by means of nitrogen and argon adsorption. *Journal of Physical Chemistry B*, 101(19):3671–3679, 1997.

P. I. Ravikovitch, G. L. Haller, and A. V. Neimark. Density functional theory model for calculating pore size distributions: pore structure of nanoporous catalysts. *Advances in Colloid and Interface Science*, 77:203–226, 1998.

References

S. J. Reitmeier, R. R. Mukti, A. Jentys, and J. A. Lercher. Surface transport processes and sticking probability of aromatic molecules in HZSM-5. *Journal of Physical Chemistry C*, 112(7):2538–2544, 2008.

S. J. Reitmeier, O. C. Gobin, A. Jentys, and J. A. Lercher. Enhancement of sorption processes in zeolite H-ZSM5 by postsynthetic surface modification. *Angewandte Chemie-International Edition*, 48(3):533–538, 2009a.

S. J. Reitmeier, O. C. Gobin, A. Jentys, and J. A. Lercher. Influence of surface modification on shape selective transport of aromatics in H-ZSM5. *Journal of Physical Chemistry C*, 113:15355–15363, 2009b.

S. J. Reitmeier, R. R. Mukti, A. Jentys, and J. A. Lercher. Surface transport processes and sticking probability of aromatic molecules in HZSM-5. *Journal of Physical Chemistry C*, 113(4):1640–1640, 2009c.

F. Rouquerol, J. Rouquerol, and K. Sing. *Adsorption by powders and porous solids.* Acad. Press, 1999, 1999.

D. Ruthven and F. Brandani. ZLC response for systems with surface resistance control. *Adsorption*, 11(1):31–34, 2005.

D. M. Ruthven. Diffusion of aromatic hydrocarbons in silicalite/HZSM-5. *Adsorption*, 13(3-4):225–230, 2007a.

D. M. Ruthven and P. Stapleton. Measurement of Liquid-Phase Counter-Diffusion in Zeolite Crystals by the ZLC Method. *Chemical Engineering Science*, 48(1):89–98, 1993.

D. M. Ruthven, W. J. DeSisto, and S. Higgins. Diffusion in a mesoporous silica membrane: Validity of the Knudsen diffusion model. *Chemical Engineering Science*, 64(13):3201–3203, 2009.

D.M. Ruthven. *Diffusion in zeolite molecular sieves*, chapter 21, pages 737–781. Elsevier, 2007b.

D.M. Ruthven, L.K. Lee, and H. Yucel. Kinetics of non-isothermal sorption in molecular-sieve crystals. *AICHE Journal*, 26(1):16–23, 1980.

R. Ryoo and S. Jun. Improvement of hydrothermal stability of MCM-41 using salt effects during the crystallization process. *Journal of Physical Chemistry B*, 101(3):317–320, 1997.

References

C. E. Salmas and G. P. Androutsopoulos. A novel pore structure tortuosity concept based on nitrogen sorption hysteresis data. *Industrial and Engineering Chemistry Research*, 40(2):721–730, 2001.

C. Sangwichien, G. L. Aranovich, and M. D. Donohue. Density functional theory predictions of adsorption isotherms with hysteresis loops. *Colloids and Surfaces A - Physicochemical and Engineering Aspects*, 206(1-3):313–320, 2002.

C. N. Satterfield and C. S. Cheng. Liquid Counterdiffusion of Selected Aromatic and Naphthenic Hydrocarbons In Type-Y Zeolites. *AICHE Journal*, 18(4):724–&, 1972.

A. Sayari. Catalysis by crystalline mesoporous molecular sieves. *Chemistry of Materials*, 8(8):1840–1852, 1996.

A. Sayari, P. Liu, M. Kruk, and M. Jaroniec. Characterization of large-pore MCM-41 molecular sieves obtained via hydrothermal restructuring. *Chemistry of Materials*, 9 (11):2499–2506, 1997.

Danny Schuring. *Diffusion in Zeolites: Towards a Microscopic Understanding*. PhD thesis, University Eindhoven, 2002.

S. K. Seshadri, H. Alsyouri, and Y. S. Lin. Counter diffusion self assembly synthesis of ordered mesoporous silica membranes in straight pore supports. *Microporous and Mesoporous Materials*, 129(1-2):228–237, 2010.

D. M. Shen and L. V. C. Rees. Diffusivities of Benzene In H-ZSM-5, Silicalite-1, and NaX Determined by Frequency-Response Techniques. *Zeolites*, 11(7):666–671, 1991.

D. M. Shen and L. V. C. Rees. Frequency-Response Technique Measurements of p-Xylene Diffusion in Silicalite-1 and Silicalite-2. *Journal of the Chemical Society, Faraday Transactions*, 89(7):1063–1065, 1993.

D. M. Shen and L. V. C. Rees. Analysis of Bimodal Frequency Response Behavior of p-Xylene Diffusion in Silicalite-1. *Journal of the Chemical Society, Faraday Transactions*, 91(13):2027–2033, 1995.

K. S. W. Sing, D. H. Everett, R. A. W. Haul, L. Moscou, R. A. Pierotti, J. Rouquerol, and T. Siemieniewska. Reporting Physisorption Data for Gas Solid Systems with Special Reference to the Determination of Surface-Area and Porosity (Recommendations 1984). *Pure and Applied Chemistry*, 57(4):603–619, 1985.

A. I. Skoulidas and D. S. Scholl. Kinetics of hard sphere and chain adsorption into circular and elliptical pores. *Journal of Chemical Physics*, 113(10):4379–4387, 2000.

References

R. Q. Snurr, A. T. Bell, and D. N. Theodorou. Prediction of Adsorption of Aromatic-Hydrocarbons in Silicalite from Grand-Canonical Monte-Carlo Simulations with Biased Insertions. *Journal of Physical Chemistry*, 97(51):13742–13752, 1993.

R. Q. Snurr, A. T. Bell, and D. N. Theodorou. Investigation of the Dynamics of Benzene in Silicalite using Transition-State Theory. *Journal of Physical Chemistry*, 98(46): 11948–11961, 1994.

S. Sommer, T. Melin, J. L. Falconer, and R. D. Noble. Transport of C-6 isomers through ZSM-5 zeolite membranes. *Journal of Membrane Science*, 224(1-2):51–67, 2003.

L. Song, Z.-L. Sun, and L. V. C. Rees. Experimental and molecular simulation studies of adsorption and diffusion of cyclic hydrocarbons in silicalite-1. *Microporous and Mesoporous Materials*, 55(1):31–49, 2002.

L. J. Song and L. V. C. Rees. Adsorption and diffusion of cyclic hydrocarbon in MFI-type zeolites studied by gravimetric and frequency-response techniques. *Microporous Mesoporous Materials*, 35-6:301–314, 2000.

M. Stempniewicz, A. S. G. Khalil, M. Rohwerder, and F. Marlow. Diffusion in coiled pores - Learning from microrelease and microsurgery. *Journal of the American Chemical Society*, 129(34):10561–10566, 2007.

L. M. Sun and V. Bourdin. Measurement of Intracrystalline Diffusion by the Frequency-Response Method - Analysis and Interpretation of Bimodal Response Curves. *Chemical Engineering Science*, 48(22):3783–3793, 1993.

L. M. Sun, F. Meunier, and J. Kärger. On the Heat Effect in Measurements of Sorption Kinetics by the Frequency-Response Method. *Chemical Engineering Science*, 48(4): 715–722, 1993.

L. M. Sun, F. Meunier, P. Grenier, and D. M. Ruthven. Frequency-Response for Nonisothermal Adsorption in Biporous Pellets. *Chemical Engineering Science*, 49(3): 373–381, 1994.

D. Tzoulaki, L. Heinke, W. Schmidt, U. Wilczok, and J. Kärger. Exploring crystal morphology of nanoporous hosts from time-dependent guest profiles. *Angewandte Chemie-International Edition*, 47(21):3954–3957, 2008a.

D. Tzoulaki, W. Schmidt, U. Wilezok, and J. Kärger. Formation of surface barriers on silicalite-1 crystal fragments by residual water vapour as probed with isobutane by interference microscopy. *Microporous and Mesoporous Materials*, 110(1):72–76, 2008b.

References

D. Tzoulaki, L. Heinke, H. Lim, J. Li, D. Olson, J. Caro, R. Krishna, C. Chmelik, and J. Kärger. Assessing Surface Permeabilities from Transient Guest Profiles in Nanoporous Host Materials. *Angewandte Chemie-International Edition*, 48(19):3525–3528, 2009.

H. van Koningsveld and J. C. Jansen. Single crystal structure analysis of zeolite H-ZSM-5 loaded with naphthalene. *Microporous Materials*, 6(3):159–167, 1996.

R. A. van Santen and G. J. Kramer. Reactivity theory of zeolitic bronsted acidic sites. *Chemical Reviews*, 95(3):637–660, 1995.

R. A. van Santen and J. W. Niemantsverdriet. *Chemical Kinetics and Catalysis*. Langmuir. Plenum Press, New York, 1995.

P. Vansteenkiste, V. Van Speybroeck, E. Pauwels, and M. Waroquier. How should we calculate multi-dimensional potential energy surfaces for an accurate reproduction of partition functions? *Chemical Physics*, 314(1-3):109–117, 2005.

C. E. Webster, R. S. Drago, and M. C. Zerner. A method for characterizing effective pore sizes of catalysts. *Journal of Physical Chemistry B*, 103(8):1242–1249, 1999.

J. Wloch. Effect of surface etching of ZSM-5 zeolite crystals on the rate of n-hexane sorption. *Microporous and Mesoporous Materials*, 62(1-2):81–86, 2003.

P. Wu, T. Tatsumi, T. Komatsu, and T. Yashima. Postsynthesis, characterization, and catalytic properties in alkene epoxidation of hydrothermally stable mesoporous Ti-SBA-15. *Chemistry of Materials*, 14(4):1657–1664, 2002.

OM Yaghi, M O'Keeffe, NW Ockwig, HK Chae, M Eddaoudi, and J Kim. Reticular synthesis and the design of new materials. *Nature*, 423(6941):705–714, 2003.

Y. Yasuda. Detection of surface-resistance in a gas porous - adsorbent system by frequency-response method. *Bulletin of the Chemical Society of Japan*, 64(3):954–961, 1991.

Y. Yasuda. Frequency-Response Method for Investigation of Gas-Surface Dynamic Phenomena. *Heterogeneous Chemistry Review*, 1(2):103–124, 1994a.

Y. Yasuda. Frequency-Response Method for Investigation of Various Dynamic Phenomena Occurring Simultaneously in a Gas Zeolite System. In *Zeolites and Related Microporous Materials: State of the Art 1994*, volume 84 of *Studies in Surface Science and Catalysis*, pages 1331–1338. 1994b.

Y. Yasuda and G. Sugasawa. A Frequency-Response Technique to Study Zeolitic Diffusion of Gases. *Journal of Catalysis*, 88(2):530–534, 1984.

References

Z. B. Ye, H. Alsyouri, S. P. Zhu, and Y. S. Lin. Catalyst impregnation and ethylene polymerization with mesoporous particle supported nickel-diimine catalyst. *Polymer*, 44(4):969–980, 2003.

L. Zhang, C. Chmelik, A. N. C. van Laak, J. Karger, P. E. de Jongh, and K. P. de Jong. Direct assessment of molecular transport in mordenite: dominance of surface resistances. *Chemical Communications*, (42):6424–6426, 2009.

D. Y. Zhao, J. L. Feng, Q. S. Huo, N. Melosh, G. H. Fredrickson, B. F. Chmelka, and G. D. Stucky. Triblock copolymer syntheses of mesoporous silica with periodic 50 to 300 angstrom pores. *Science*, 279(5350):548–552, 1998a.

D. Y. Zhao, Q. S. Huo, J. L. Feng, B. F. Chmelka, and G. D. Stucky. Nonionic triblock and star diblock copolymer and oligomeric surfactant syntheses of highly ordered, hydrothermally stable, mesoporous silica structures. *Journal of the American Chemical Society*, 120(24):6024–6036, 1998b.

X. S. Zhao, G. Q. M. Lu, and G. J. Millar. Advances in mesoporous molecular sieve MCM-41. *Industrial and Engineering Chemistry Research*, 35(7):2075–2090, 1996.

S. Zheng. Surface modification of hzsm-5 zeolites. *PhD. Thesis*, 2002.

S. Zheng, H. R. Heydenrych, H. P. Röger, A. Jentys, and J. A. Lercher. On the enhanced selectivity of H-ZSM-5 modified by chemical liquid deposition (CLD). *Topics in Catalysis*, 22(1-2):101–106, 2003.

S. Zheng, A. Jentys, and J. A. Lercher. Xylene isomerization with surface-modified HZSM-5 zeolite catalysts: An in situ IR study. *Journal of Catalysis*, 241(2):304–311, 2006.

S. R. Zheng, H. Tanaka, A. Jentys, and J. A. Lercher. Novel model explaining toluene diffusion in HZSM-5 after surface modification. *Journal of Physical Chemistry B*, 108 (4):1337–1343, 2004.

List of Figures

List of Tables

List of Publications

Publications in scientific journals

1. **Diffusion in circularly ordered mesoporous silica fibers**
   Hatem Alsyouri, **Oliver C. Gobin**, Andreas Jentys, and Johannes A. Lercher,
   J. Phys. Chem. C; **2011**; 115(17), pp 8602–8612

2. **Nanoporous glass as a model system for a consistency check of the different techniques of diffusion measurement**
   Chmelik C, Enke D, Galvosas P, **Gobin O**, Jentys A, Jobic H, Kärger J, Krause CB, Kullmann J, Lercher J, Naumov S, Ruthven DM, Titze T,
   PhysChemPhys; **2011**; 12(6), pp 1130-1134

3. **Adsorption of C2-C8 n-Alkanes in Zeolites**
   Bart A. De Moor, Marie-Franoise Reyniers, **Oliver C. Gobin**, Johannes A. Lercher, and Guy B. Marin,
   J. Phys. Chem. C; **2011**; 115(4), pp 1204–1219

4. **Role of the surface modification on the transport of hexane isomers in ZSM5**
   Oliver C. Gobin, Stephan J. Reitmeier, Andreas Jentys, and Johannes A. Lercher,
   J. Phys. Chem. C; **2011**; 115(4), pp 1171–1179

5. **Comparison of the Transport of Aromatic Compounds in Small and Large MFI Particles**
   Oliver C. Gobin, Stephan J. Reitmeier, Andreas Jentys, and Johannes A. Lercher,
   J. Phys. Chem. C; **2009**; 113(47), pp 20435-20444

6. **Comparison of Single- and Multiobjective Design of Experiment in Combinatorial Chemistry for the Selective Dehydrogenation of Propane**
   Javier Llamas-Galilea, **Oliver C. Gobin**, and Ferdi Schüth,
   J. Comb. Chem.; **2009**; 11(5), pp 907-913

7. **Diffusion pathways of benzene, toluene and p-xylene in MFI**
   Oliver C. Gobin, Stephan J. Reitmeier, Andreas Jentys, and Johannes A. Lercher,
   Microporous and Mesoporous Mat.; **2009**; 125(1-2), pp 3-10

8. **Influence of Postsynthetic Surface Modification on Shape Selective Transport of Aromatic Molecules in HZSM-5**
   Stephan J. Reitmeier, **Oliver C. Gobin**, Andreas Jentys, and Johannes A. Lercher,
   J. Phys. Chem. C; **2009**; 113(34), pp 15355-15363

9. **Enhancement of Sorption Processes in the Zeolite H-ZSM5 by Postsynthetic Surface Modification**
   Stephan J. Reitmeier, **Oliver C. Gobin**, Andreas Jentys, and Johannes A. Lercher,
   Angew. Chem. Int. Ed.; **2009**; 48(3), pp 533-538

10. **On the Suitability of Different Representations of Solid Catalysts for Combinatorial Library Design by Genetic Algorithms**
    Oliver C. Gobin, and Ferdi Schüth,
    J. Comb. Chem.; **2008**; 10(6), pp 835-846

11. **Multi-objective optimization in combinatorial chemistry applied to the selective catalytic reduction of NO with C3H6**
    Oliver C. Gobin, Alberto Martinez-Joaristi, and Ferdi Schüth,
    J. Catal.; **2007**; 252(2), pp 205-214

12. **Mesostructured Silica SBA-16 with Tailored Intrawall Porosity Part 2: Diffusion**
    Oliver C. Gobin, Qinglin Huang, Hoang Vinh-Thang, Freddy Kleitz, Mladen Eic, and Serge Kaliaguine,
    J. Phys. Chem. C; **2007**; 111(7), pp 3059-3065

13. **Mesostructured Silica SBA-16 with Tailored Intrawall Porosity Part 1: Synthesis and Characterization**
    Oliver C. Gobin, Ying Wan, Dongyuan Zhao, Freddy Kleitz, and Serge Kaliaguine,
    J. Phys. Chem. C; **2007**; 111(7), pp 3053-3058

Selected publications in scientific conferences

1. **Diffusion in circularly ordered mesoporous silica fibers**
   H. Alsyouri, **Oliver C. Gobin**, Andreas Jentys, and Johannes A. Lercher, Talk, 16th International Zeolite Conference, **2010**, Sorrento, Italy

2. **Evolutionary approach to the solution of multimodal reaction networks**
   Oliver C. Gobin, Michael Salzinger, and Johannes A. Lercher, Poster, 43. Deutsche Katalysetagung, **2010**, Weimar, Deutschland

3. **Sorption and transport processes of hexane isomers in H-ZSM-5 with surface modification**
   Oliver C. Gobin, Stephan J. Reitmeier, Andreas Jentys, and Johannes A. Lercher, Poster, 42. Deutsche Katalysetagung, **2009**, Weimar, Deutschland

4. **Diffusion of aromatics in MFI-type zeolites**
   Oliver C. Gobin, Stephan J. Reitmeier, Andreas Jentys, and Johannes A. Lercher, Talk, 21. Deutsche Zeolithtagung, **2009**, Kiel, Germany

5. **Measuring diffusion in zeolites by pressure frequency response**
   Oliver C. Gobin, Stephan J. Reitmeier, Andreas Jentys, and Johannes A. Lercher, Poster, 20. Deutsche Zeolithtagung, **2008**, Halle a.d. Saale, Deutschland

6. **Multi-objective Optimization in Combinatorial Chemistry Applied to the Selective Catalytic Reduction of NOx**
   Oliver C. Gobin, Alberto Martínez-Joaristi, and Ferdi Schüth, Poster, Europacat VIII, **2007**, Turku, Finland

7. **Stage I and Stage II High Throughput Techniques for the development of mixed oxides DeNOx catalysts**
   Alberto Martínez-Joaristi, **Oliver C. Gobin**, and Ferdi Schüth, Poster, EuroCombiCat, **2007**, Bari, Italy